

FEASIBILITY STUDY OF ALPHA PARTICLE
DENSITOMETERS FOR MEASURING
PLANETARY ATMOSPHERIC
DENSITY

Distribution of this report is provided in the interest of
information exchange. Responsibility for the contents
resides in the author or organization that prepared it.

FINAL REPORT

Prepared by

Frederick A. Hanser and Bach Sellers

for

NASA Langley Research Center
Langley Station, Hampton, Virginia

Contract No.
NAS 1-8487

June 1969

PANAMETRICS, INC.
221 Crescent Street
Waltham, Massachusetts 02154

CASE FILE
COPY

FEASIBILITY STUDY OF ALPHA PARTICLE
DENSITOMETERS FOR MEASURING
PLANETARY ATMOSPHERIC
DENSITY

Distribution of this report is provided in the interest of
information exchange. Responsibility for the contents
resides in the author or organization that prepared it.

FINAL REPORT

Prepared by

Frederick A. Hanser and Bach Sellers

for

NASA Langley Research Center
Langley Station, Hampton, Virginia

Contract No.
NAS 1-8487

June 1969

PANAMETRICS, INC.
221 Crescent Street
Waltham, Massachusetts 02154

FOREWORD

The research reported herein was carried out for the NASA Langley Research Center in Hampton, Virginia. Special appreciation is given to Mr. Gary W. Grew, the Technical Representative for the NASA Langley Research Center, who provided much valuable assistance.

This is a final report and summarizes work performed over the period July 1968 to May 1969. The assistance of Mr. Lawrence E. Starratt in making some of the system response measurements is gratefully acknowledged.

ABSTRACT

The use of radioactive alpha particle sources to measure gas density has been investigated. Such systems consist of a source separated from a detector by a fixed distance, with a gas then reducing the alpha energy. The "thin source" system uses a monoenergetic alpha source and measures the average energy loss, while the "thick source" system uses a source having a broad spectrum and measures the count rate above a fixed threshold. For either system used in combination with CO₂, N₂ and Ar atmospheres the measured density is given by $\rho_m = \rho_{CO_2} + \rho_{N_2} + 0.67 \rho_{Ar}$ to $\pm 2\%$. The thin source system gives greater accuracy at high densities, while the thick source system can have the accuracy adjusted to be better at low densities. Use with an x-ray attenuation system allows the quantities $\rho_{CO_2} + \rho_{N_2}$ and ρ_{Ar} to be determined separately. When no composition information is available the alpha particle system alone will measure the density of the Martian atmosphere to $\pm 8\%$, based on the extreme VM models.

TABLE OF CONTENTS

	<u>Page</u>
FOREWORD	ii
ABSTRACT	iii
LIST OF ILLUSTRATIONS	viii
LIST OF TABLES	xii
1. INTRODUCTION	1
2. OPERATIONAL ENVIRONMENT	3
2.1 Description of the Martian Atmosphere	3
2.2 Estimated Entry Characteristics for a Martian Lander	3
2.3 Decontamination Requirements for a Martian Lander	7
3. DENSITY MEASUREMENT - BASIC FORMULATION AND DESIGN CONSIDERATIONS	7
3.1 General Discussion	7
3.1.1 Thin Source Method	10
3.1.2 Thick Source Method	15
3.2 Applications in CO ₂ , N ₂ and Ar Atmospheres	21
3.2.1 Theoretical and Measured Stopping Powers	21
3.2.2 Composition Dependence Limitations	24
3.3 Detector Considerations	26
3.3.1 Discussion of Proton Radiation Damage Studies	29
3.3.2 Experimental Results of Alpha Particle Irradiation of Surface-Barrier Detectors	32
3.3.3 Limitations Imposed by the Detectors	33
3.4 Theoretical Formulation of the Errors	38
3.4.1 Thin Source System	38
3.4.2 Thick Source System	42
4. DENSITY MEASUREMENT-EXPERIMENTAL RESULTS AND PROPOSED SYSTEM DESIGNS	43
4.1 Thin Source Method	45
4.1.1 Experimental Calibration Curves	45
4.1.2 Expected Errors for the Thin Source Method	54
4.1.3 Alpha Source Manufacture, Reproducibility and Stability	54

TABLE OF CONTENTS (cont' d)

	<u>Page</u>
4.2 Thick Source Method	59
4.2.1 Experimental Calibration Curves	59
4.2.2 Expected Errors for the Thick Source Method	73
4.2.3 Alpha Source Manufacture, Reproducibility, and Stability	79
4.3 Proposed System Designs	81
4.3.1 General Discussion	81
4.3.2 Thin Source Method	81
4.3.3 Thick Source Method	89
4.3.4 Comparison of Methods	89
5. ARGON COMPOSITION MEASUREMENT	92
5.1 General Discussion	92
5.2 Neptunium M X-Ray Attenuation	93
5.2.1 Theoretical Formulation	93
5.2.2 Experimental Results	95
5.2.3 Expected Errors for the X-Ray Attenuation System	98
5.2.4 Proposed System Designs	102
5.3 Argon Fluorescent X-Ray Measurement	105
5.3.1 Theoretical Formulation	105
5.3.2 Experimental Results	107
5.3.3 Expected Errors for the Fluorescent X-Ray System	109
5.3.4 Proposed System Designs	115
5.4 Comparison of Methods	115
6. SUMMARY	117
6.1 Density Measurements	117
6.1.1 Thin Source Method	117
6.1.2 Thick Source Method	117
6.2 Argon Composition Measurement	121
6.2.1 X-Ray Attenuation Method	121
6.2.2 Fluorescent X-Ray Method	121
6.3 Estimated Density Measurement Accuracy	121
6.3.1 Alpha Particle System Used with Argon Composition Measurement	121
6.3.2 Alpha Particle System Used with Separate Gas Composition Measurement	125

TABLE OF CONTENTS (cont' d)

	<u>Page</u>
6.3.3 Alpha Particle System Used with No Composition Information	125
7. CONCLUSIONS AND RECOMMENDATIONS	126
APPENDIX A - CALCULATION OF GAS DENSITIES FROM PRESSURE AND TEMPERATURE MEASUREMENTS	130
APPENDIX B - APPROXIMATE CALCULATION OF THE EFFECTS OF A TEMPERATURE DIFFERENCE BETWEEN THE DENSITY MEASURING SYSTEM AND THE ATMOSPHERIC GASES	132
APPENDIX C - DISCUSSION OF THE EFFECTS OF CO AND H ₂ O IN THE MEASURED ATMOSPHERE	137
APPENDIX D - EFFECT OF A FROST LAYER ON THE SYSTEMS	140
REFERENCES	141

LIST OF ILLUSTRATIONS

<u>Figure</u>		<u>Page</u>
2. 1	Variation of Density with Altitude in the Martian Atmosphere Models VM-1 to VM-10.	4
2. 2	Estimated Altitude vs. Time Profiles for a Martian Lander.	5
3. 1	Outline of the Basic Operation of a Gas Density Measuring System Using Alpha Particles.	9
3. 2	Thin Source Method - Illustration of the Variation of the Detected Alpha Particle Spectrum with Gas Density.	11
3. 3	Thin Source Method - Calibration Curve for CO ₂ , using Am ²⁴¹ at 30 cm.	12
3. 4	Thick Source Method - Illustration of the Variation of the Detected Alpha Particle Spectrum with Gas Density.	16
3. 5	Thick Source Method - Calibration Curve for CO ₂ , using Am ²⁴¹ Foil #11.68 at 30 cm and a Threshold of 1 MeV.	17
3. 6	Calculated Stopping Powers of CO ₂ , N ₂ and Ar for Alpha Particles of 2 to 7 MeV.	22
3. 7	Calculated Stopping Powers of CO ₂ , N ₂ and Ar for Alpha Particles of 0.4 to 6 MeV - Converted from Proton Values.	23
3. 8	Experimental Values of the Stopping Power of CO ₂ , N ₂ and Ar for Alpha Particles.	25
3. 9	Thin Source Calibration Curves for CO ₂ , N ₂ and Ar with an Attenuation Foil over the Source.	27
3. 10	Thin Source Calibration Curves for CO ₂ , N ₂ and Ar with an Attenuation Foil over the Detector.	28
3. 11	Summary of Results on Radiation Damage to Silicon Surface-Barrier Detectors by 50 keV to 1 MeV Protons (Based on Ref. 3.4).	30
3. 12	Summary of Results on Radiation Damage to Silicon Surface-Barrier Detectors by 0.8 to 5 MeV Protons (Based on Ref. 3.5).	31

LIST OF ILLUSTRATIONS (cont' d)

<u>Figure</u>		<u>Page</u>
3. 13	Results of 4. 5 MeV Alpha Irradiation Tests on a Silicon Surface-Barrier Detector - Leakage Current and Resolution.	34
3. 14	Leakage Current vs. Bias Voltage of a Silicon Surface-Barrier Detector after Irradiations by 4. 5 MeV Alpha Particles.	35
3. 15	Leakage Current and Resolution for Am ²⁴¹ vs. Alpha Fluence for a Silicon Surface-Barrier Detector (from Ref. 3. 9).	36
4. 1	Geometry for Thick and Thin Source Configuration Tests.	44
4. 2	Spectra of an Am ²⁴¹ Vacuum Sublimed Source and of the Po ²¹⁰ Foil Source.	47
4. 3	Calibration Points for CO ₂ , N ₂ and Ar with 5. 48 MeV Am ²⁴¹ Source, Showing Region of Straight Line Fit at Low Densities.	48
4. 4	Plots of Average Stopping Power vs. Argon Mass Fraction of Gas.	49
4. 5	Calibration Curve for Am ²⁴¹ (5. 48 MeV) at 30 cm.	52
4. 6	Calibration Curve for Am ²⁴¹ (3. 22 MeV) at 30 cm.	53
4. 7	Spectra of the Three Am ²⁴¹ Foil Sources.	60
4. 8a	Spectra of an Am ²⁴¹ Foil Source with and without Al Foil Coverings.	61
4. 8b	Spectrum of an Am ²⁴¹ Foil Source with a Partial Al Foil Covering.	62
4. 9	Spectra of the Po ²¹⁰ Microsphere Source with and without Al Foil Coverings.	63
4. 10	Calibration Points for CO ₂ , N ₂ and Ar Using an Am ²⁴¹ Foil Source and a 0. 25 MeV Threshold - No Detector Covering Foil.	64
4. 11	Calibration Points for CO ₂ , N ₂ and Ar Using an Am ²⁴¹ Foil Source and a 0. 25 MeV Threshold - Detector Covered with 0. 45 mil Al Foil.	65

LIST OF ILLUSTRATIONS (cont' d)

<u>Figure</u>	<u>Page</u>
4. 12 Spectrum of Am ²⁴¹ Foil Source Covered One-half with 0. 45 mil Al Foil and One-half with 0. 60 mil Al Foil.	66
4. 13 Calibration Points for CO ₂ and N ₂ Using an Am ²⁴¹ Foil Source Covered with Al Foils to Generate the Spectrum of Figure 4. 14.	68
4. 14 Spectrum of Am ²⁴¹ Foil Source Covered with Several 0. 15 mil Al Foils.	69
4. 15 Calibration Data with the Po ²¹⁰ Microsphere Source at 30 cm.	70
4. 16 Calibration Data with the Am ²⁴¹ Foil Source #11.68 at 30 cm.	71
4. 17 Calibration Data with the Am ²⁴¹ Foil Source #112572/1 at 30 cm.	72
4. 18 Plots of Several Thick Source System Calibration Curves.	75
4. 19 Statistical Error in Density for Several Thick Source Systems - Maximum Performance Designs.	76
4. 20 Total Density Errors for Several Thick Source Systems, Including a One Percent Telemetry Error - Minimum Power Designs.	80
4. 21 Physical Layout of an Alpha Particle Density Measuring System, as Mounted on Portions of the Lander Structure.	82
4. 22 Design of the Electronics and Detector Housing for the Minimum Power Configuration.	83
4. 23 Design of the Electronics and Detector Housing for the Maximum Performance Configuration.	84
4. 24 Electronics Design for Minimum Weight and Power Consumption - Thin Source System.	85
4. 25 Electronics Design for Intermediate Power Consumption - Thin Source System.	87

LIST OF ILLUSTRATIONS (cont' d)

<u>Figure</u>		<u>Page</u>
4. 26	Electronics Design for Maximum Performance - Thin Source System.	88
4. 27	Electronics Design for Minimum Weight and Power Consumption - Thick Source System.	90
4. 28	Electronics Design for Maximum Performance - Thick Source System.	91
5. 1	Proportional Counter Detection Efficiency for X-Rays.	96
5. 2	Np M X-Ray Spectrum.	97
5. 3	Np M X-Ray Attenuation Results - Source Covered with 3 mils Be.	99
5. 4	Np M X-Ray Attenuation Results - Source Uncovered.	100
5. 5	Np M X-Ray Attenuation Results - Source Partially Collimated.	101
5. 6	Electronics Design for the Np M X-Ray Attenuation System.	104
5. 7	Outline of the Argon Fluorescent X-Ray Detection System to be Used on a Martian Lander.	106
5. 8	Results of the Ar K X-Ray Production Measurements.	108
5. 9	Power Law Fits to the Ar K X-Ray Data.	110
5. 10	Plots of the Ar K X-Ray Data on an Ar Mass Fraction Scale.	111
6. 1	Plots of N ₂ to CO ₂ and of Ar to CO ₂ Stopping Power Ratios.	118
C. 1	Plots of CO to CO ₂ and of H ₂ O to CO ₂ Stopping Power Ratios.	139

LIST OF TABLES

<u>Table</u>		<u>Page</u>
2. 1	Surface Density in Mars Atmosphere Models	6
2. 2	Lander Descent Velocities and Density Rates of Change for VM-8 and VM-9 Atmospheres	6
2. 3	Martian Lander Decontamination Procedure (Tentative)	8
3. 1	Values of \bar{E} , σ , $\delta \bar{E}_{st}$, and $\delta \bar{E}_{drift}$ for an Am ²⁴¹ Alpha Source	41
4. 1	Properties of Some Alpha Emitters Suitable for Thin Source Manufacture	46
4. 2	Comparison of Some Average Stopping Powers	50
4. 3	Some Thin Source System Parameters	55
4. 4	Expected Errors for the Thin Source System	56
4. 5	Data on the Stability of Am ²⁴¹ Vacuum Sublimed Sources	58
4. 6	Data on the Stability of a Po ²¹⁰ Foil Source	58
4. 7	Data on the Thick Source Systems Described in Figures 4. 18, 4. 19 and 4. 20	74
4. 8	Electronic Drift Errors for the Thick Source System	78
4. 9	Comparison of Various Density Measuring Systems	78
5. 1	Statistical Errors for the Np M X-Ray Attenuation System	103
5. 2	Results of the Ar K X-Ray Measurements	112
5. 3	Expected Errors for the Fluorescent X-Ray System	114
5. 4	Comparison of Ar Measurement Systems	116
6. 1	Estimated Errors of the Thin Source System	119
6. 2	Estimated Errors of the Thick Source System	120
6. 3	Estimated Errors of the X-Ray Attenuation System	122

LIST OF TABLES (cont' d)

<u>Table</u>	<u>Page</u>
6. 4 Errors for the Thin Source System Used with the Np M X-Ray System	123
6. 5 Errors for the Thick Source System Used with the Np M X-Ray System	124
6. 6 Composition Dependent Density Errors for the Alpha Particle System Used Alone	127
A. 1 Density Differences Between the Perfect Gas Law and the Van der Waals Equation	131

1. INTRODUCTION

It is expected that in the next decade several lander vehicles will explore the atmosphere and surface of the planet Mars. These landers will send back much scientifically important data, including the vertical atmospheric density profile, and the diurnal and seasonal surface air density variations. The vertical density profile will be measured during the entry descent, while the surface density variations will be measured during the remainder of the lander's lifetime.

Atmospheric gas density can be measured by two principal methods. The first involves measuring the gas temperature, pressure and average molecular weight, from which the gas density can be obtained through use of the perfect gas law, as shown in Appendix A. If the acceleration of gravity at the Martian surface is known as well as its variation with altitude, and if the average molecular weight of the atmosphere is known, then the vertical density profile can be obtained from pressure vs. temperature data, or from temperature or pressure vs. altitude data, provided at least one complete density measurement is made. Diurnal and seasonal variations require both pressure and temperature measurements, as well as knowledge of the average molecular weight. Since a complete density measurement requires at least one set of pressure, temperature and average molecular weight data, the failure of any one of these systems will preclude obtaining any absolute density measurements.

The second type of density measurement is a direct measurement, a system which responds primarily to gas density. Since the interaction of nuclear and atomic radiation is generally dependent only on the amount of matter rather than its pressure and temperature, such radiation-based systems offer great promise for measuring gas density. Use of a direct density measurement along with pressure, temperature and average molecular weight measurements forms a redundant system which allows internal checks on system performance. Also, if one component fails a complete set of data is still obtained.

Of the radiation methods for density measurement the one that is the subject of this report is the α particle system. Here an α source is located at a fixed separation from a detector, and the introduction of a gas into this space causes a reduction in the energy of the detected α particles. Two methods are distinguished, the "thin source" method where the average energy lost is measured, and the "thick source" method where the particles with energy above a fixed threshold are counted. Both systems can be calibrated for response vs. gas density, and then used to measure absolute gas density.

The major difficulty with α particle systems is that the response is somewhat composition dependent. For the expected composition of the Martian atmosphere this may not be too critical. It is found that the system can be designed such that CO_2 and N_2 produce nearly the same response, while Ar can

be measured by other methods and its effect can thus be compensated. The precise methods developed are discussed in the following sections.

The majority of this report describes the experimental and theoretical investigation of α particle density measuring systems. The investigation was oriented primarily toward the Martian atmosphere. Methods of obtaining partial composition information are also discussed. If gas composition is known, then the α particle systems become absolute density measuring systems. The report concludes with α particle density measuring system designs, including recommendations as to which of these designs is best suited for use on a Martian lander.

2. OPERATIONAL ENVIRONMENT

2.1 Description of the Martian Atmosphere

The design of a density measuring system for use in the Martian atmosphere should take account of any currently available information about that atmosphere. Existing estimates of the surface atmosphere density are useful for obtaining an approximate maximum density which the system must measure. Since alpha particle density measuring systems are also sensitive to gas composition, any information on composition of the Martian atmosphere will be of use in relating the response of these systems to the actual gas density.

The work and designs described in this report were carried out primarily on the basis of the Martian atmosphere models VM-1 to VM-10 described in the Statement-of-Work (Ref. 2.1). These models assume only CO_2 , N_2 , and Ar as significant atmospheric constituents; the ground level atmospheric densities for these models are listed in Table 2.1. These should be considered as approximate, especially as they encompass a variation of about a factor of 6. The variation of density with altitude for the various atmospheres is shown in Figure 2.1.

The ground level density estimates of Table 2.1 list a maximum of about $40 \times 10^{-6} \text{ g/cm}^3$. The density measuring systems will thus be designed for a maximum density of about $80 \times 10^{-6} \text{ g/cm}^3$, the factor 2 increase allowing for possible landings in a depression, or an actual density somewhat greater than any listed in Table 2.1.

The atmospheric compositions listed in Table 2.1 show that CO_2 is established as a likely component of the Martian atmosphere. Since only CO_2 is listed as the sole component of an atmosphere, the study of alpha particle density measuring systems should concentrate on the response to CO_2 . Nitrogen is the next most likely gas and should be considered second in the study. Finally, Ar is present in only three of the ten atmospheres, and only to 36% by weight, so it will be considered as least likely to be present of the three gases, CO_2 , N_2 and Ar.

2.2 Estimated Entry Characteristics for a Martian Lander

Entry characteristics for two projected paths and for two of the extreme Martian atmospheres (VM-8 and VM-9) are shown in Figure 2.2 (taken from Ref. 2.1). From Figures 2.2 and 2.1 we find the descent velocities and rates of density change listed in Table 2.2. The rate of density change does not vary significantly with altitude (for the descent curves in Figure 2.2) nor with the atmosphere model. It is expected that the lander would have a useful descent lifetime of one hundred to a few hundred seconds, descent velocity on the order of 50 m/sec, and observe density rate of change of $0.05 \times 10^{-6} \text{ g/cm}^3\text{-sec}$.

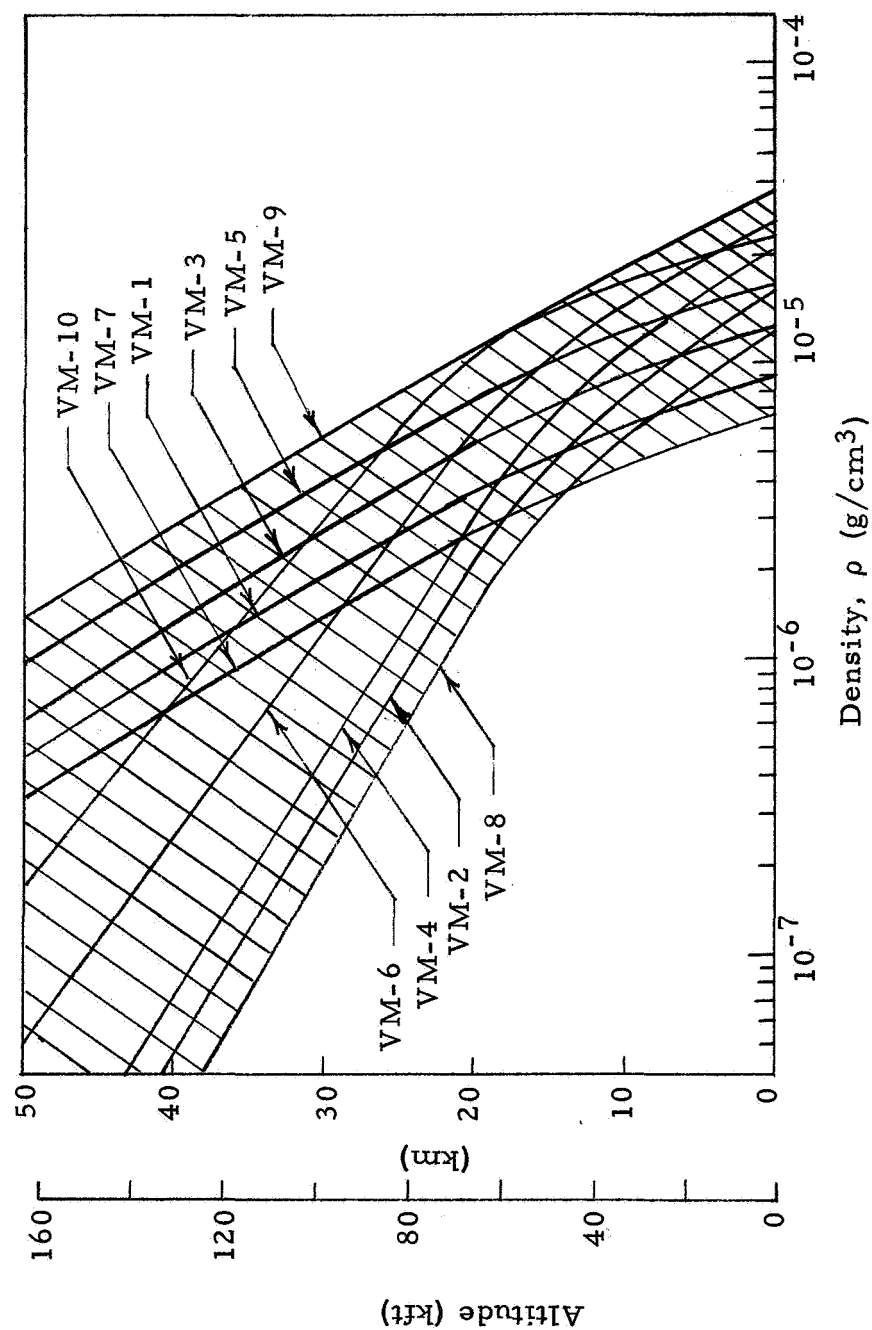


Figure 2.1 Variation with Altitude in the Martian Atmosphere Models VM-1 to VM-10.

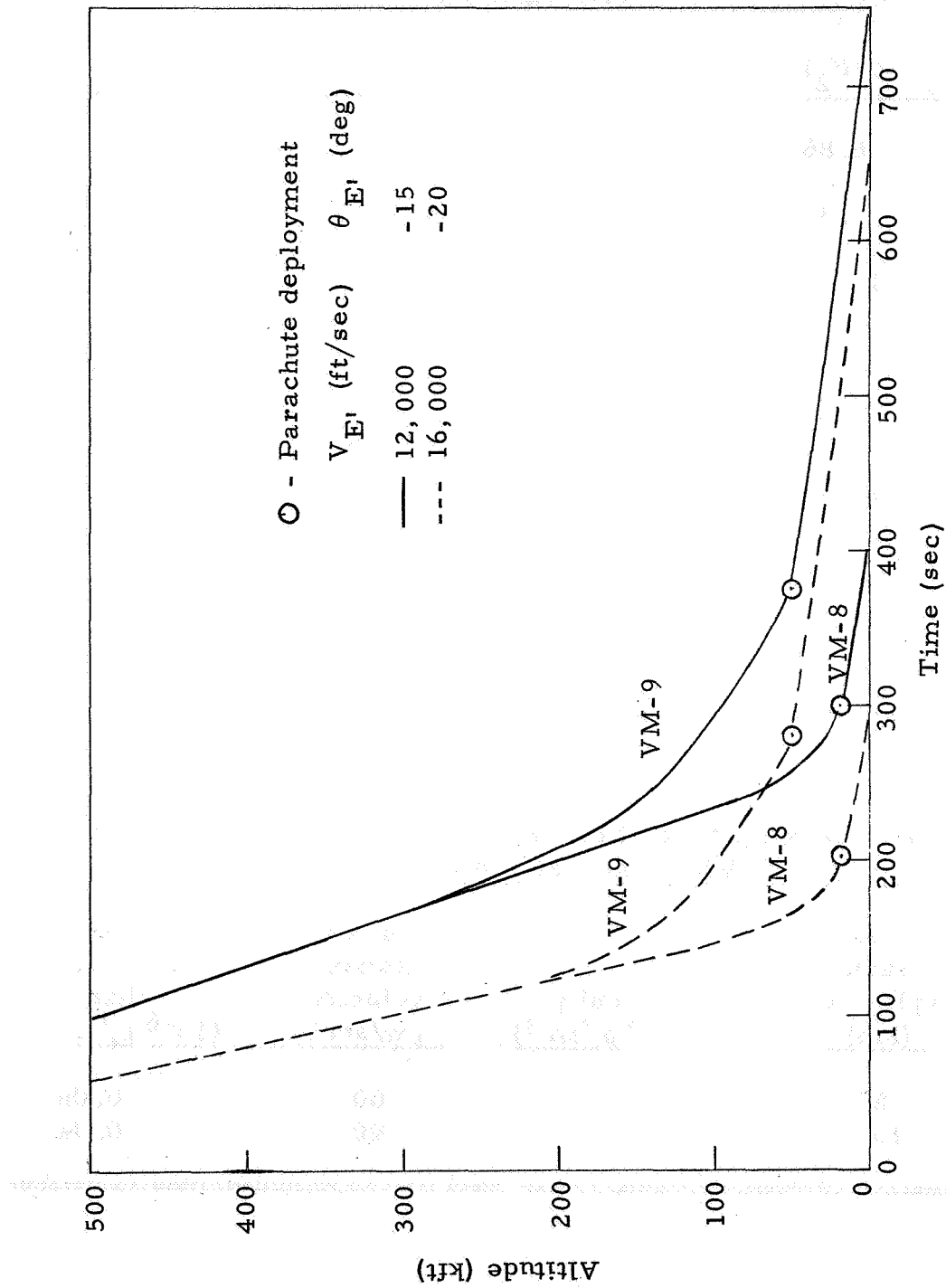


Figure 2.2 Estimated Altitude vs. Time Profiles for a Martian Lander

Table 2. 1

Surface Density in Mars Atmosphere Models
(10^{-6} g/cm³)

Atm #	ρ (N ₂)	ρ (CO ₂)	ρ (Ar)	ρ total
VM-1	6.86	2.69	-	9.55
VM-2	-	18.5	-	18.5
VM-3	9.80	3.85	-	13.65
VM-4	-	18.0	7.71	25.7
VM-5	13.7	5.39	-	19.1
VM-6	8.81	11.0	11.0	30.8
VM-7	4.88	1.92	-	6.8
VM-8	-	13.2	-	13.2
VM-9	19.6	7.70	-	27.3
VM-10	23.7	4.98	9.58	38.3

Table 2. 2

Lander Descent Velocities and Density Rates of Change for
VM-8 and VM-9 Atmospheres

Atm #	Altitude of parachute deployment (km)	Density (10^{-6} g/cm ³)	Lander descent velocity (m/sec)	Rate of density change (10^{-6} g/cm ³ -sec)
VM-8	6	8	60	0.06
VM-9	15	15	40	0.04

2.3 Decontamination Requirements for a Martian Lander

The search for life-forms on Mars is expected to be difficult, particularly since it must be shown that detected forms are native to Mars and not spacecraft contaminants. For this reason the Martian lander is expected to undergo a decontamination procedure before launch to destroy as completely as possible all life-type molecules that may be in or on the lander. Design of the density measuring system must take this decontamination procedure into account, since some components may be adversely affected by the treatment.

A tentative outline of the decontamination procedure is listed in Table 2.3. This outline was obtained from the Technical Representative, and should be considered very preliminary, as no final procedure has yet been set. The procedure can be summarized briefly as several hundred hours at 135°C in a 100% N₂ atmosphere, and a couple of hundred hours at 50°C in an atmosphere of 12% ethylene oxide and 88% Freon-12 at 35% humidity.

3. DENSITY MEASUREMENT - BASIC FORMULATION AND DESIGN CONSIDERATIONS

3.1 General Discussion

The basic operation of a gas density measuring system using alpha particles is outlined in Figure 3.1. An alpha source and detector are separated by a distance D and are surrounded by a gas with density ρ . The particles observed by the detector are sent to a signal analyzer which puts out a voltage (analog or digital) called the system response R . The response R can then be measured for several gas densities ρ and calibration curves obtained. Thereafter the density of a gas of the same composition can be measured by using the proper calibration curve and the system response when placed in that gas.

The components of Figure 3.1 which can be adjusted to modify the system calibration curve are three: the operation of the signal analyzer; the spectrum of the alpha source; and the source-detector separation D . Since the output of the signal analyzer is one voltage while the input is the alpha spectrum incident on the detector, it is obvious that some information has been lost in obtaining such a response. The design of the signal analyzer should be such that a minimum amount of useful information is lost. The two most practical designs for the signal analyzer are those in which the output is either: (1) the average energy of the alpha particles; or (2) the average count rate above a given threshold in alpha energy. In both cases the response curve is also influenced by the source spectrum.

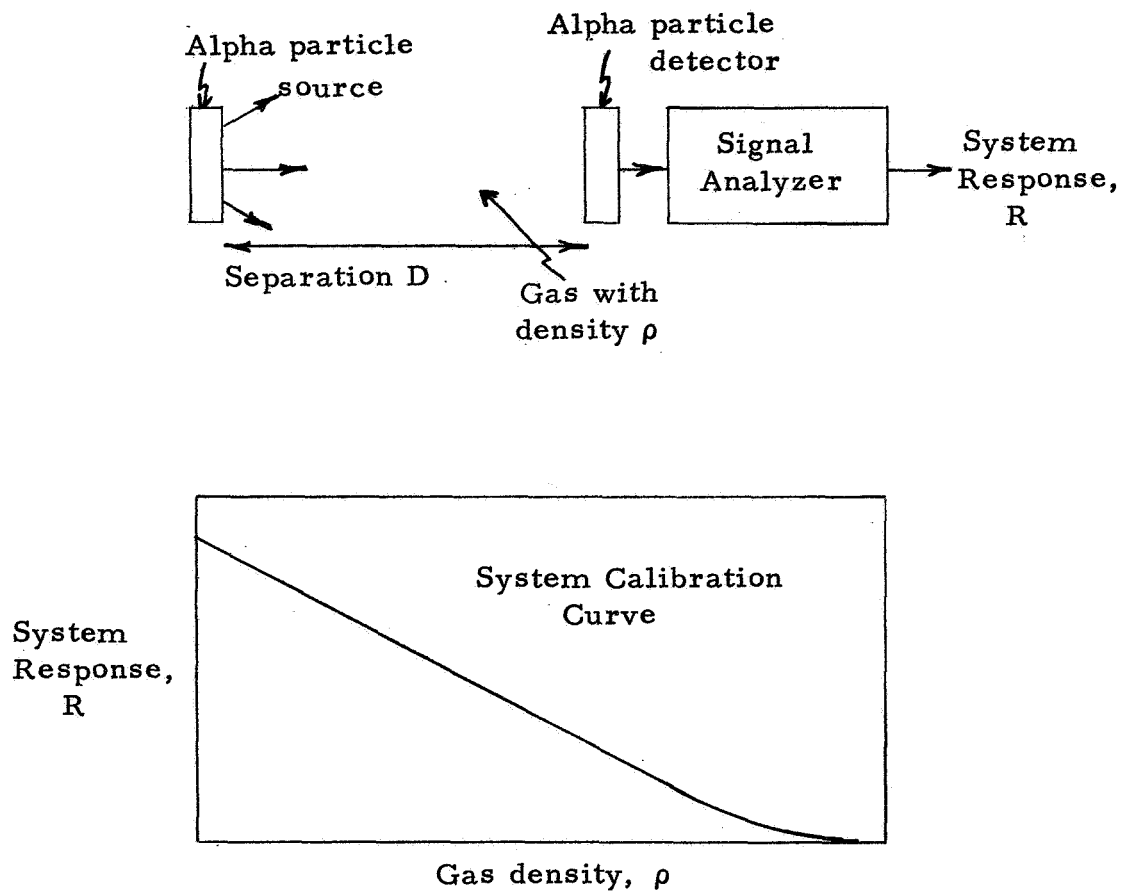
The spectrum of the alpha source can have very wide variations, but a general distinction can be made between sources with a very narrow alpha energy distribution (peaked energy spectra) and sources with a very broad

Table 2.3

Martian Lander Decontamination Procedure (Tentative)

Definitions: heat \equiv 100% N₂ atmosphere
 decontamination \equiv 12% ethylene oxide and
 88% Freon-12 at 35%
 humidity

Stage	Number of cycles	Hours per cycle	Atmosphere	Temperature (°C)
Acceptance	1	24	heat	40
Assembly	1	60	heat	125
Spacecraft	1	60	heat	125
Qualification	6	92	heat	135
(parts)	1	28	decontamination	50
(assemblies)	1	26	decontamination	50
	6	26	decontamination	50



Measured density error:

$$\delta \rho = \frac{d\rho}{dR} \delta R$$

Figure 3.1 Outline of the Basic Operation of a Gas Density Measuring System Using Alpha Particles.

alpha energy distribution. Since the detector must have a finite count rate and the signal analyzer must use a finite time interval over which to analyze the detector output, statistical error considerations show that a narrow alpha source spectrum is best used with the first type of signal analyzer, while the broad spectrum is best used with the second type. These two combinations of source and signal analyzer are described in more detail in the following sections as the thin source method and the thick source method.

The source-detector separation D enters only as a scale factor for the density ρ . The system response R depends only on the product $x = \rho D$. Thus, changing D changes the range over which ρ can be measured. If the calibration curve is plotted as R vs. x it is then independent of D . For a given separation D we then have

$$\rho = x(R)/D \quad (3.1)$$

with an error

$$\Delta\rho = \frac{dx}{dR} \frac{\Delta R}{D} \quad (3.2)$$

where $x(R)$ depends only on the source spectrum and the signal analyzer. This property is very useful as it allows measurements at any separation D to be converted to any other separation with only a change in source strength to keep the alpha flux at the detector constant.

3.1.1 Thin Source Method

The thin source method uses a nearly monoenergetic alpha source and a signal analyzer which gives the average alpha energy as the output (see Figure 3.1). The method is based on the property that alpha particles lose energy nearly continuously rather than being completely absorbed like x-rays. Alpha particles thus have a unique range-energy relationship for a given gas, and a measurement of the energy lost over a given pathlength D can yield the density of the gas.

Figure 3.2 shows a number of alpha spectra measured by the detector in a thin source configuration. An uncovered Am-241 vacuum sublimed alpha source is used with a source-detector separation of $D = 30$ cm. The various spectra show how the average alpha energy at the detector is reduced as the gas density (CO_2) is increased. The spread in the alpha peak at low energies illustrates the statistical variations present in the energy loss process. The low energy background arises from scattering in the source and must be taken into account when calculating the statistical errors of the system response. The calibration curve for this system with CO_2 gas is shown in Figure 3.3.

The calibration curve for the thin source method can be analyzed in

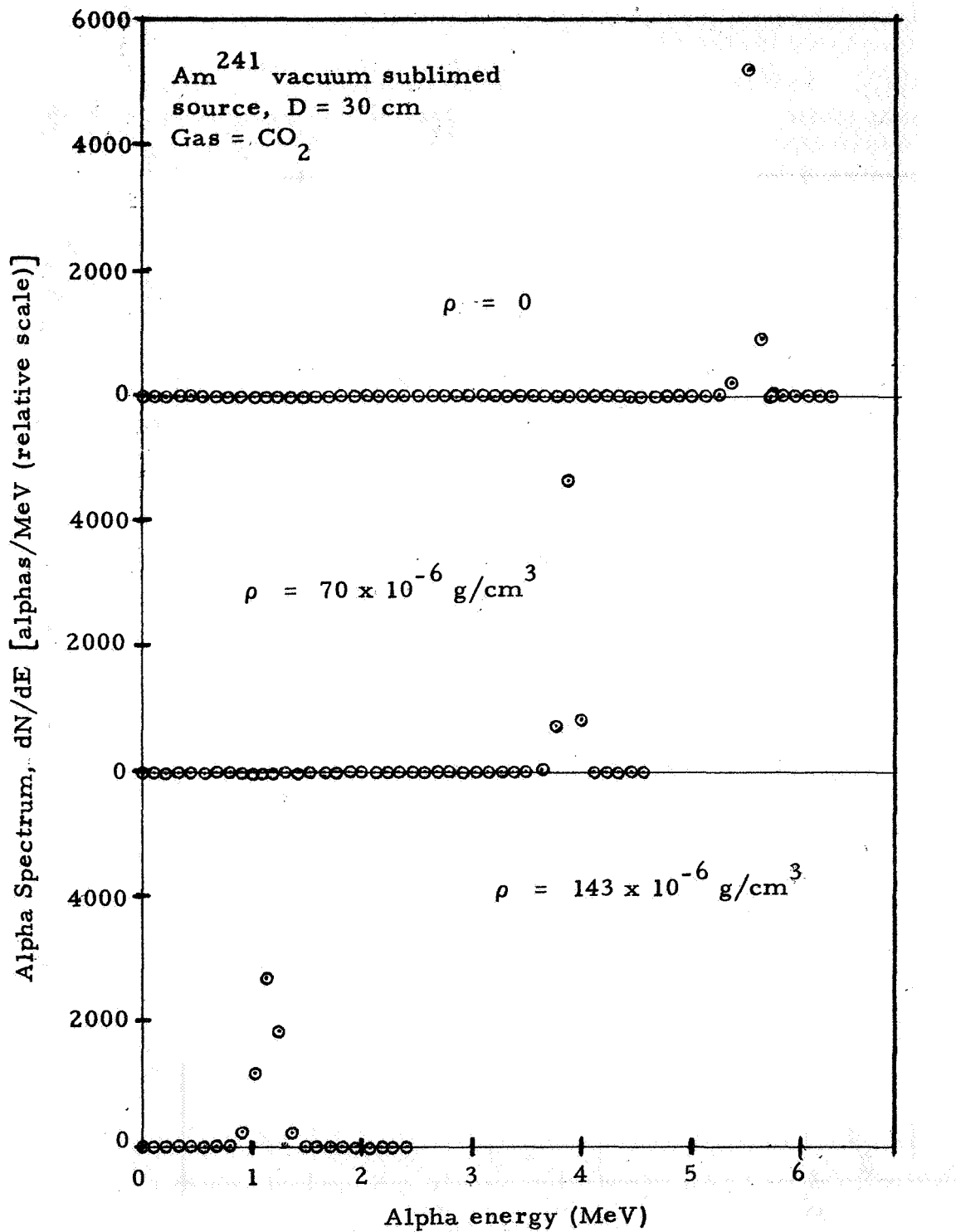


Figure 3.2 Thin Source Method - Illustration of the Variation of the Detected Alpha Particle Spectrum with Gas Density.

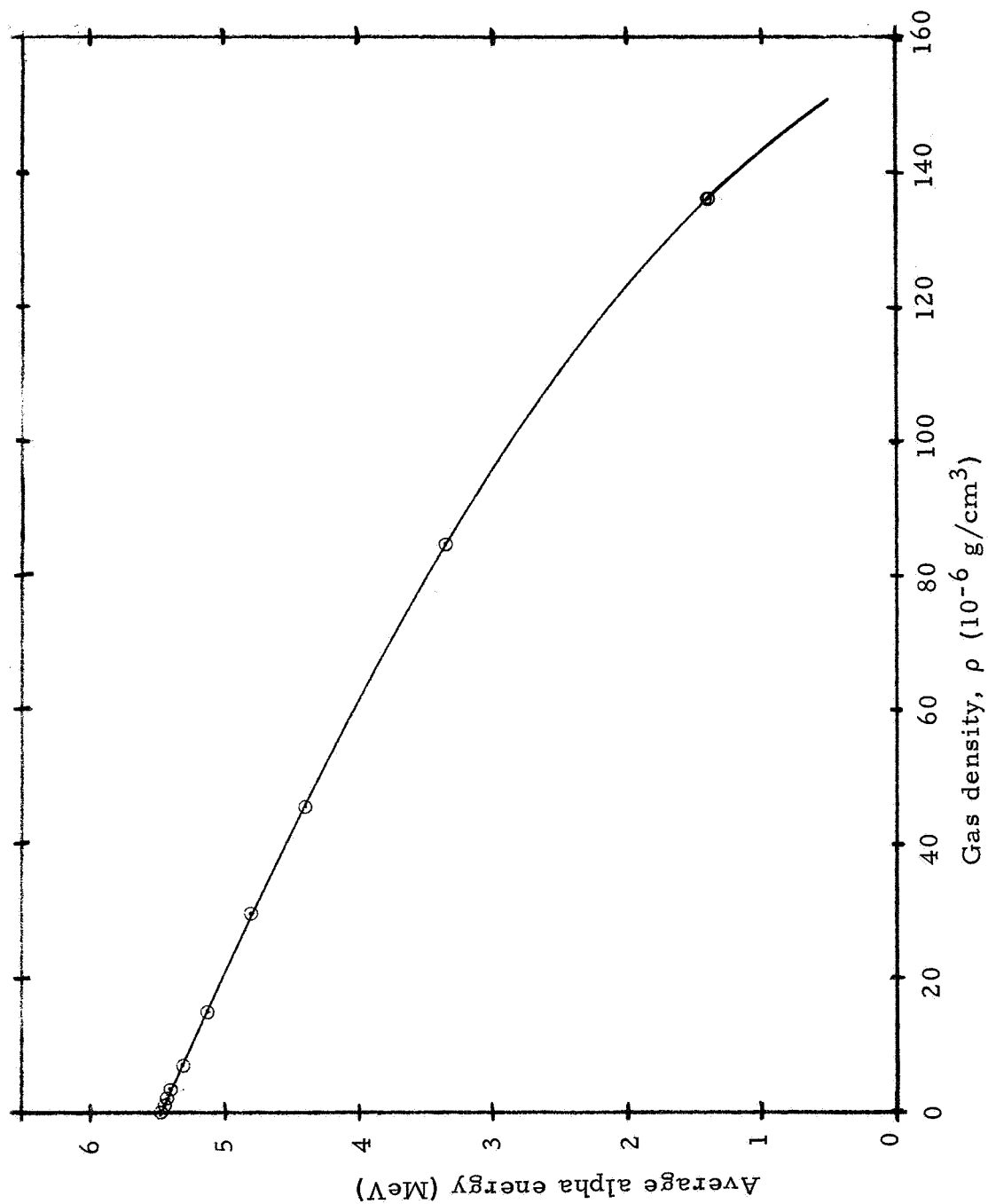


Figure 3.3 Thin Source Method - Calibration Curve for CO₂, using Am²⁴¹ at 30 cm.

terms of the stopping power of the gas for alpha particles, $S(E) = -dE/dx$ in MeV-cm²/g. (Note that the units on x are g/cm².) For a gas density of ρ g/cm³ and an average alpha energy of E MeV incident on the detector a slight increase in density $\Delta\rho$ thus results in a change in E of

$$\Delta E = -DS(E) \Delta\rho \quad (3.3)$$

or

$$\frac{dE}{d\rho} = -DS(E) \quad (3.4)$$

Equation (3.4) can be integrated to give

$$\int_E^{E_0} \frac{dE}{S(E)} = \rho D \quad (3.5)$$

where E is the average energy measured by the detector at a gas density ρ and E_0 is the average alpha source energy. If $S(E)$ for a given gas is known then (3.5) allows the thin source method calibration curve to be calculated from $S(E)$, E_0 and D . Equation (3.5) also shows explicitly that the calibration curve is a function of ρD , and that if $S(E)$ differs for two gases then they will have different calibration curves. The latter point is investigated in more detail in Section 3.2. The thin source system calibration curve is, to first order, not dependent on the width of the alpha peak.

For the case where the detector is covered with a foil of thickness t_f g/cm² we obtain

$$\int_{E_1}^{E_0} \frac{dE}{S(E)} = \rho(E) D \quad (3.5a)$$

where

$$\int_E^{E_1} \frac{dE}{S_f(E)} = t_f \quad (3.5b)$$

Here E is the measured energy and $S_f(E)$ the stopping power of the foil. From (3.5a) and (3.5b) the form for (3.4) becomes

$$\frac{dE}{d\rho} = - \frac{DS_f(E)}{S_f(E_1)} S(E_1) \quad (3.4a)$$

Equation (3.5) can be easily used with a gas of known composition since $S(E)$ is the stopping power of the mixture. For a gas composed of several components of weight fraction w_i ($\sum_i w_i = 1$) and stopping power $S_i(E)$, (3.5) becomes

$$\int_E^{E_0} \frac{dE}{\sum_i w_i S_i(E)} = \rho(E) D \quad (3.6)$$

If the system is calibrated with one component gas, say (1) with $S_1(E)$, then the calibration curve is

$$\rho_1(E) D = \int_E^{E_0} \frac{dE}{S_1(E)} \quad (3.7)$$

By defining

$$f(E) = \frac{\int_E^{E_0} \frac{dE}{\sum_i w_i S_i(E)}}{\int_E^{E_0} \frac{dE}{S_1(E)}} \quad (3.8)$$

we obtain

$$\rho(E) = \rho_1(E) f(E) \quad (3.9)$$

where $\rho(E)$ is the actual density and $\rho_1(E)$ is the "measured" density obtained from the calibration curve for gas (1). Note that in order to use (3.9) all w_i and $S_i(E)$ must be known so that $f(E)$ may be calculated.

By way of example, in a three component gas, a system calibrated with gas (1), and with

$$\begin{aligned} S_2(E) &= f_{21} S_1(E) \\ S_3(E) &= f_{31} S_1(E) \end{aligned} \quad (3.10)$$

where f_{21} and f_{31} are constants at least over the range E to E_0 , then (3.9)

becomes

$$\rho(E) = \frac{\rho_1(E)}{(w_1 + w_2 f_{21} + w_3 f_{31})} \quad (3.11)$$

3.1.2 Thick Source Method

The thick source method uses a broad alpha particle source spectrum and a signal analyzer which gives the count rate above a fixed energy threshold averaged over some period of time as the output (see Figure 3.1). In this case the presence of a gas reduces the energy of a portion of the alpha particles below the threshold and so changes the system count rate. A number of alpha spectra measured by the detector in a thick source configuration are shown in Figure 3.4, with the resulting calibration curve given in Figure 3.5.

The calibration curve for the thick source method can be calculated from the source spectrum shape $\frac{dN}{dE}(E)$ (alphas/MeV), the stopping power of the gas for alpha particles $S(E)$ (MeV-cm²/g), the detector threshold E_{th} (MeV), and the source-detector separation D (cm). For a gas density ρ (g/cm³) the effective threshold in terms of the source energy spectrum E_{eff} is given by

$$\int_{E_{th}}^{E_{eff}} \frac{dE}{S(E)} = \rho D \quad (3.12)$$

or

$$R(E_{eff}) - R(E_{th}) = \rho D \quad (3.13)$$

where

$$R(E) = \int_0^E \frac{dE}{S(E)} \quad (3.14)$$

is the range in g/cm² of an alpha particle of energy E . The signal analyzer output is then given by

$$C = \frac{sA}{D^2} \int_{E_{eff}}^{\infty} \frac{dN}{dE}(E) dE \quad (3.15)$$

where C is the system count rate in cps, A the detector area in cm², s the source strength in alpha emissions/(sec-sr), and the source spectrum shape

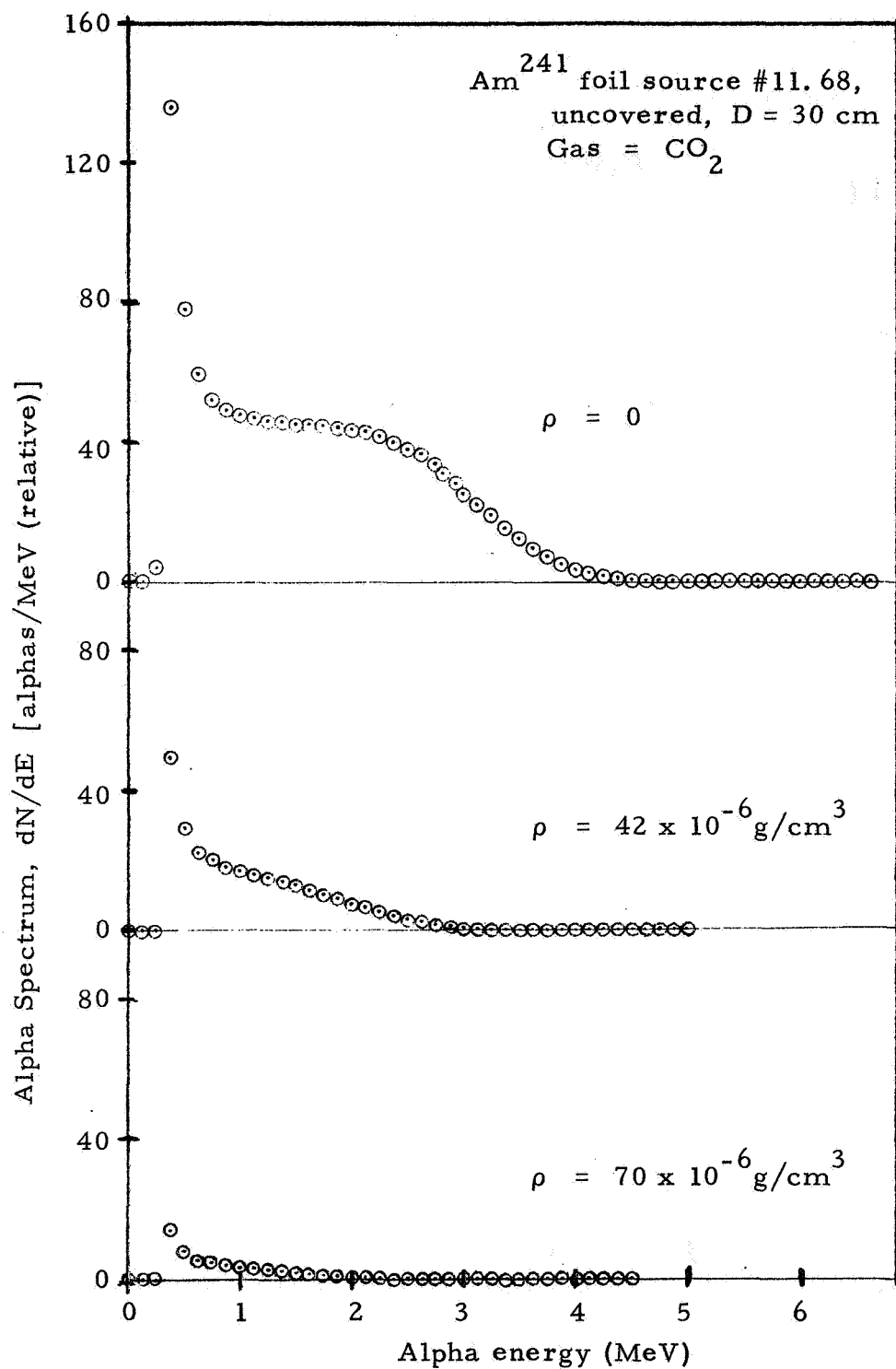


Figure 3.4 Thick Source Method - Illustration of the Variation of the Detected Alpha Particle Spectrum with Gas Density.

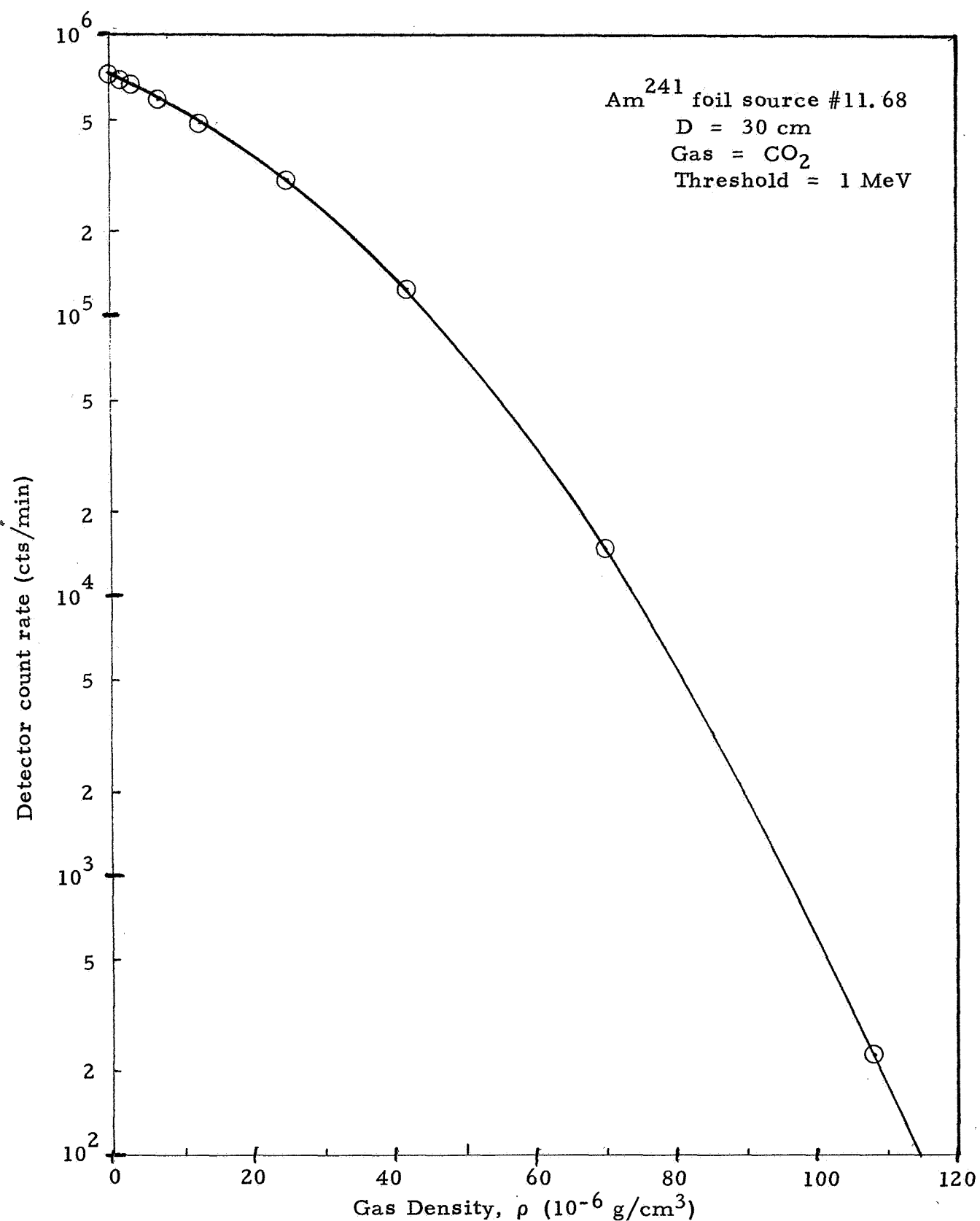


Figure 3.5 Thick Source Method - Calibration Curve for CO₂, using Am²⁴¹ Foil #11.68 at 30 cm and a Threshold of 1 MeV.

has been normalized so

$$\int_0^{\infty} \frac{dN}{dE} (E) dE = 1 \quad (3.16)$$

For the case where the detector is covered with a thin foil the preceding analysis still holds provided E_{th} is replaced by E'_{th} where

$$\int_{E_{th}}^{E'_{th}} \frac{dE}{S_f(E)} = t_f \quad (3.12a)$$

in which t_f is the foil thickness (g/cm^2), $S_f(E)$ the stopping power of the foil, E_{th} the detector threshold, and E'_{th} the threshold energy referred to the entrance side of the foil. Note that E_{th} and E'_{th} are fixed energies.

Since the thick source method has a calibration curve which is strongly dependent on the alpha spectrum shape, dN/dE , it has more inherent flexibility than the thin source method, although this also means that the thick source method is more sensitive to any degradation of the source spectrum. It is thus possible to shape the calibration curve by adjusting the source spectrum. If from other considerations we desire to have the calibration curve be $C(\rho)$, then from Equations (3.15) and (3.12) we obtain

$$\frac{dN}{dE} (E) = \frac{D}{sA S(E)} \frac{dC}{d\rho} \quad (3.17)$$

where $dC/d\rho$ is calculated for the value of ρ satisfying (3.12) with $E_{eff} = E$.

Before using Eq. (3.17) to calculate a desired spectrum we must find a reason for selecting a form for $C(\rho)$. This can be done on the basis of the statistical errors in $C(\rho)$, which, for a counting time of T seconds, is (see Section 3.4)

$$\Delta C = \sqrt{C/T} \quad (3.18)$$

From (3.18) we obtain

$$\begin{aligned}\Delta\rho &\equiv \frac{d\rho}{dC} \Delta C \\ &= \frac{d\rho}{dC} \sqrt{C/T}\end{aligned}\tag{3.19}$$

We can now consider several possibilities for $\Delta\rho$ and in each case integrate Eq. (3.19) to obtain $\rho(C)$ (and $C(\rho)$).

First, we may wish to have a constant density error $\Delta\rho$, for all densities of interest. This leads to

$$\rho = 2\Delta\rho \sqrt{C_0 T} \left[1 - \sqrt{C/C_0} \right]\tag{3.20}$$

with

$$\Delta\rho = \frac{\rho_{\max}}{2 \sqrt{C_0 T}}\tag{3.21}$$

where C_0 is the count rate above the threshold for zero density, and ρ_{\max} is the maximum density to be measured (the density at which the count rate C becomes zero).

A second system is one in which the fractional density error, $\Delta\rho/\rho = K$, is held constant. For this case

$$\rho = \rho_{\max} e^{-2K \sqrt{CT}}\tag{3.22}$$

which we note requires an infinite count rate C for zero density. This result shows that any actual system, which is limited to finite count rates, must have a non-zero density error at zero density.

A third system, chosen only for illustration, is a straight line form for $\rho(C)$ which gives

$$\rho = \rho_{\max} (1 - C/C_0)\tag{3.23}$$

and

$$\begin{aligned}\Delta \rho &= \frac{\rho_{\max}}{C_0} \sqrt{C/T} \\ &= \frac{\rho_{\max}}{\sqrt{C_0 T}} \sqrt{1 - \rho/\rho_{\max}}\end{aligned}\tag{3.24}$$

The latter form of Eq. (3.24) shows that for this case $\Delta \rho$ approaches zero at $\rho = \rho_{\max}$.

Further discussion of the desirable, and achievable forms for $C(\rho)$ and the resulting spectra (from Eq. (3.17)) is delayed to Section 3.4 where system errors are discussed more fully. Limitations on the alpha particle density measuring system must first be discussed to set desirable values for C_0 and find possible limitations for E_{th} . For the present it need only be noted that changing the alpha source spectrum allows the density which can be measured with a maximum accuracy to be located almost anywhere in the density range 0 to ρ_{\max} , except near zero.

For a mixture of gases we modify (3.12) in a manner similar to (3.5) and obtain (we use E for E_{eff})

$$\int_{E_{th}}^E \frac{dE}{\sum_i w_i S_i(E)} = \rho(E) D \tag{3.25}$$

By defining

$$f(E) = \frac{\int_{E_{th}}^E \sum_i w_i S_i(E) dE}{\int_{E_{th}}^E \frac{dE}{S_1(E)}} \tag{3.26}$$

and the equivalent density of the calibration gas (1)

$$\rho_1(E) D = \int_{E_{th}}^E \frac{dE}{S_1(E)} \tag{3.27}$$

then

$$\rho(E) = \rho_1(E) f(E) \tag{3.28}$$

Note that $f(E)$ is slightly different than (3.8) for the thin source method, as it is an integral from E_{th} up to E rather than from E_0 down to E . Since the thick source method uses a count rate rather than an energy measurement, Eq.(3.15) must be used to convert $E(E_{eff})$ to C to form

$$\rho(C) = \rho_1(C) f(C) \quad (3.29)$$

This last conversion can be quite tedious if $f(E)$ is not a simple function. For a three gas mixture with the constant stopping power ratios of (3.10) the conversions are simple and yield

$$\rho(C) = \frac{\rho_1(C)}{(w_1 + w_2 f_{21} + w_3 f_{31})} \quad (3.30)$$

3.2 Applications in CO_2 , N_2 and Ar Atmospheres

3.2.1 Theoretical and Measured Stopping Powers

The analysis in Section 3.1 shows that any composition dependence of the alpha particle density measuring system enters through variations in the stopping power of the various gases. Composition dependence is thus most directly investigated by measuring the stopping power of the gases of interest.

A preliminary estimate of composition effects can be obtained from calculated values of the stopping power. Figure 3.6 shows the stopping power calculations of Hill et al. (Ref. 3.1) for CO_2 , N_2 and Ar, along with the ratio of Ar to CO_2 stopping powers. The calculations only go down to 2 MeV, but show N_2 as about 2% greater than CO_2 , and Ar as only 64% to 69% of the CO_2 stopping power over the range 2 to 5.5 MeV.

Stopping power estimates for alphas below 2 MeV can be obtained from proton calculations using average values of the α to proton stopping power ratio. As described by Whaling (Ref. 3.2), the proton energies are for an equivalent α energy a factor of 3.97 higher. Above 2 MeV α energy the ratio is 4, but for lower energies values in a table by Whaling (Ref. 3.2, p 214) must be used. In this manner the proton stopping power calculations of Janni (Ref. 3.3) have been converted to α stopping powers and plotted in Figure 3.7. Here the values below 1 MeV show large (> 10%) deviations between the CO_2 and N_2 stopping powers, as well as strong variations in the Ar- CO_2 stopping power ratio.

Experimental values for the stopping power of CO_2 , N_2 and Ar are

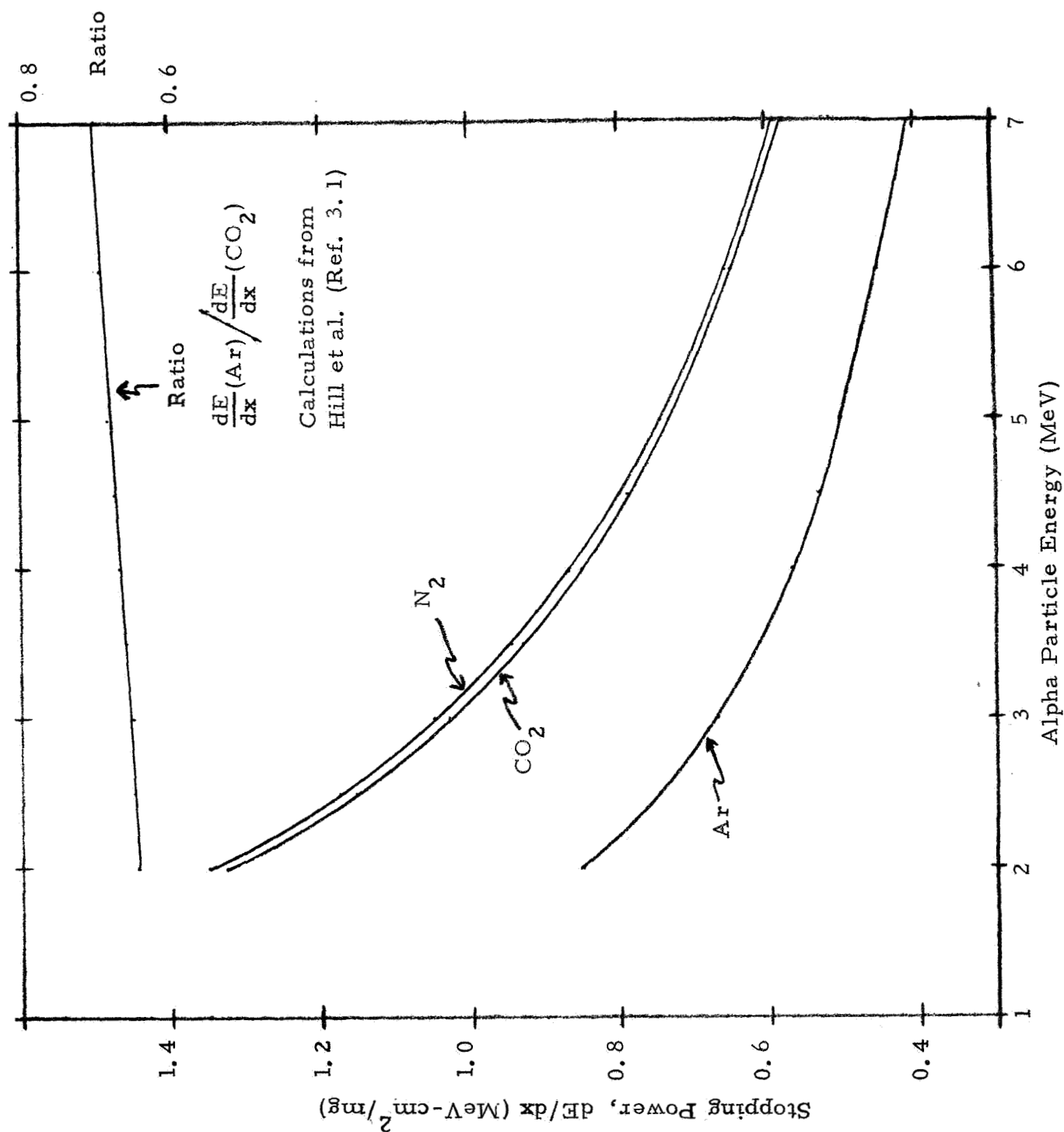


Figure 3.6 Calculated Stopping Powers of CO_2 , N_2 and Ar for Alpha Particles of 2 to 7 MeV.

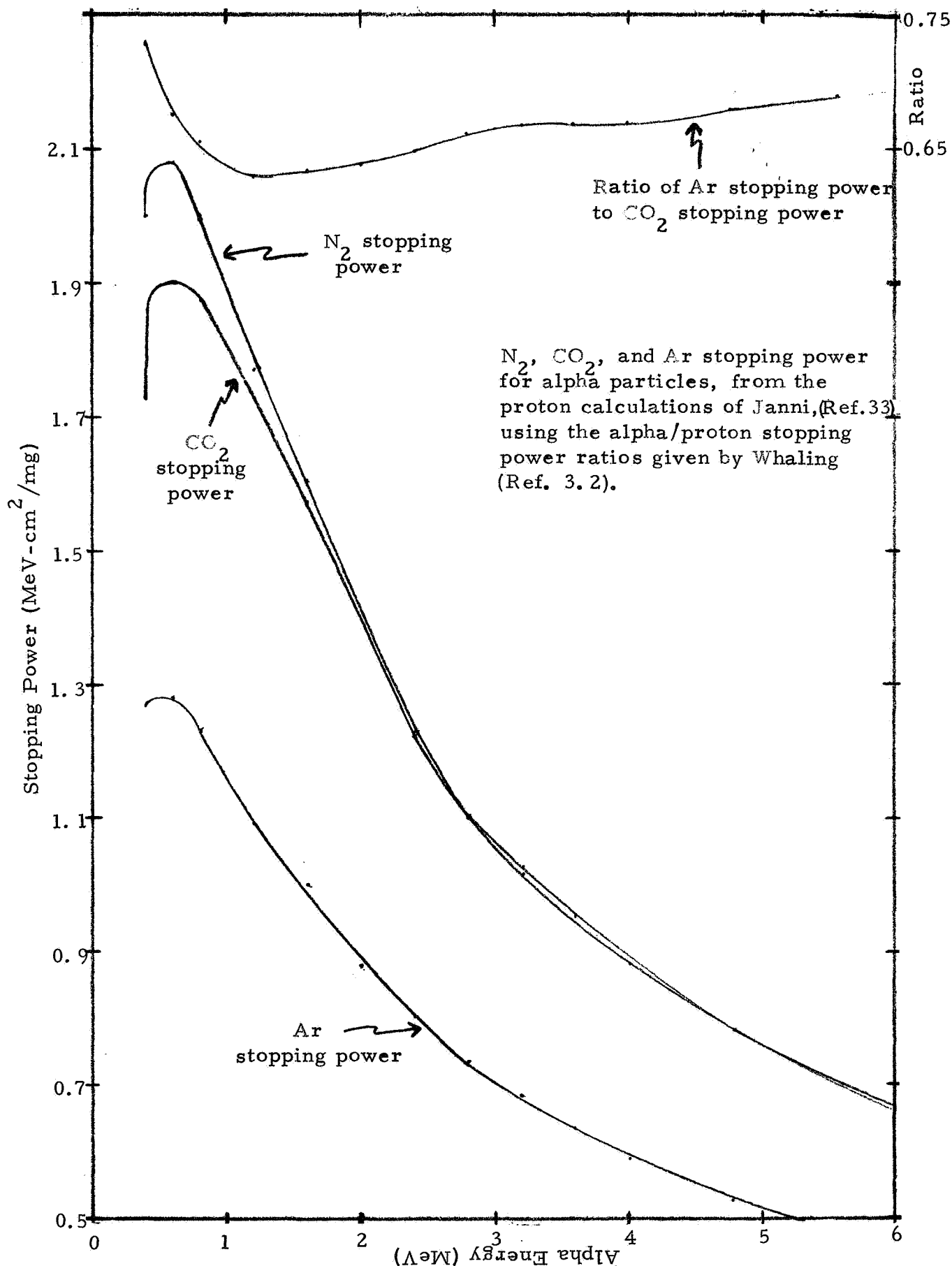


Figure 3.7 Calculated Stopping Powers of CO_2 , N_2 and Ar for Alpha Particles of 0.4 to 6 MeV - Converted from Proton Values.

plotted in Figure 3.8. These measurements were taken from the data used for the thin source calibration curves described in Section 4.1. The curves in Figure 3.8 are approximate best fits to the points above 1 MeV. The experimental values are about 5% higher than the theoretical values of Figures 3.6 and 3.7. The N₂-CO₂ stopping power ratio varies from about 1.15 at 0.6 MeV to 1.05 at 1 MeV and 1.02 at 5.5 MeV. For the Ar-CO₂ stopping power ratio the corresponding values are 0.80, 0.66, and 0.69, with a minimum of 0.65 at about 1.5 MeV.

3.2.2 Composition Dependence Limitations

The results of the preceding section show that for alpha energies above 1 MeV we have approximately

$$S_{N_2}(E) = S_{CO_2}(E) \left[1.035 \pm 0.015 \right] \quad (3.31)$$

and

$$S_{Ar}(E) = S_{CO_2}(E) \left[0.67 \pm 0.02 \right] \quad (3.32)$$

From either of Equations (3.11) and (3.30) we can then write

$$\rho = \frac{\rho_m}{(w_{CO_2} + 1.035 w_{N_2} + 0.67 w_{Ar})} \quad (3.33)$$

where ρ_m is the "measured" density using the system response and the calibration curve for CO₂. Since $\rho w_{CO_2} = \rho_{CO_2}$, etc., this can also be written

$$\rho_m = \rho_{CO_2} + 1.035 \rho_{N_2} + 0.67 \rho_{Ar} \quad (3.34)$$

We define the error in a density measurement as

$$\xi = \left| \frac{\rho_m - \rho}{\rho_m} \right| \quad (3.35)$$

where we have used the "measured" density as a base. From Equations (3.34) and (3.35) we see that a system calibrated with CO₂ will have an average error of 3.4% when used in N₂, and of 49% when used in Ar. This assumes that no composition information is available. For the Martian atmosphere models the

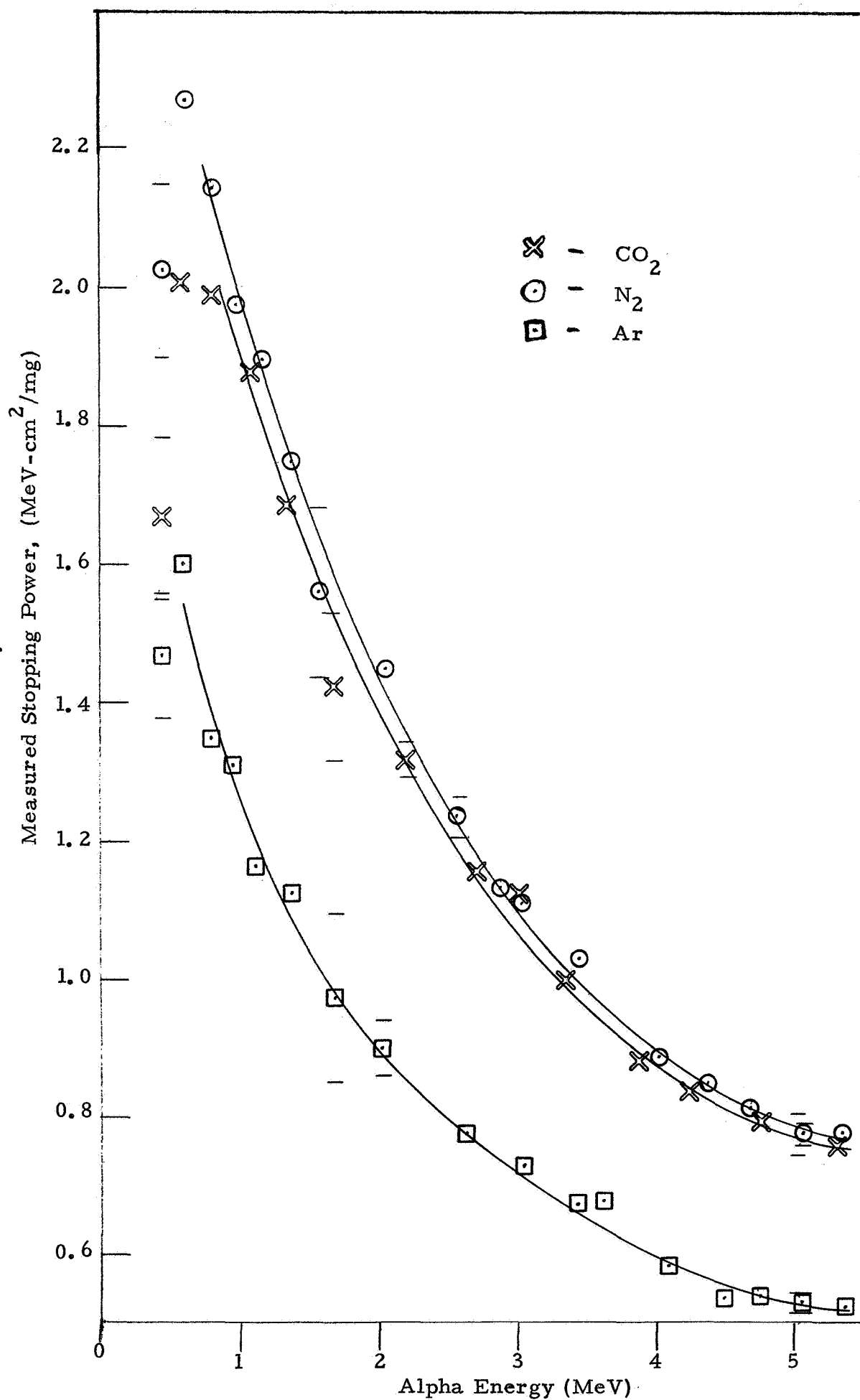


Figure 3.8. Experimental Values of the Stopping Power of CO_2 , N_2 and Ar for Alpha Particles.

largest error is 12% with VM-6. If composition information is available, then from (3.31) and (3.32) the largest error for an N₂ atmosphere is 1.4%, and for an Ar atmosphere 3%. When the gas composition is known errors can be reduced even more by using the $f(E)$ factors defined in Equations (3.8) and (3.26). For the present we note that because of the large variations in the N₂-CO₂ and Ar-CO₂ stopping power ratios below 1 MeV, this should be the approximate lowest value for alpha energy loss in the gas.

Figures 3.9 and 3.10 illustrate the composition dependence of the thin source method. An Am²⁴¹ vacuum sublimed source was located 30 cm from a 1 cm² solid state detector and a 0.75 mil thick Al foil was placed over the source for the data of Figure 3.9, and over the detector for the data of Figure 3.10. Note that for a residual α energy of 0.5 MeV the N₂ densities are 5.5% and 2.5% less than the CO₂ densities for Figures 3.9 and 3.10, respectively, while for Ar the results are 46% and 44% greater. The thick source method yields similar results. This shows that the system should be designed such that its response is due to energy loss in the gas for alpha energies above 1 MeV, in order to maintain the N₂-CO₂ difference at less than a few percent.

3.3 Detector Considerations

A Martian lander will be in flight from earth to Mars for a period of about six months. If no provision is made for a shield, the solid state detector will be irradiated by the alpha source for at least that period, and this must not cause sufficient radiation damage to the detector to impair the density measurements. By allowing for at least a few months of operation on the Martian surface, it appears that the system should have a design lifetime in excess of 1 year $\approx 3 \times 10^7$ seconds.

Radiation damage to silicon solid state detectors generally sets in slowly, with there being no sharp cut-off beyond which the detector cannot be used. The first sign of radiation damage is an increase in leakage current followed, after much greater irradiation, by a worsening of detector energy resolution. Eventually microplasma breakdown occurs and the detector must be operated at lower bias voltages, and under even more irradiation, the resolution becomes so poor and the maximum bias voltage so low that the detector is useless. Some recovery may occur when the detector is heated to a few hundred degrees C for several hours, but this is not a feasible process for the density measuring systems under consideration.

The following sections discuss radiation damage in silicon detectors caused by protons and by alpha particles. The results are then used to set approximate upper limits to the alpha flux incident on the solid state detector of the density measuring system. It should be emphasized that there is no sharp cut-off, but only a gradual degradation of performance, primarily an increase in detector leakage current. Thus, the alpha flux chosen for the

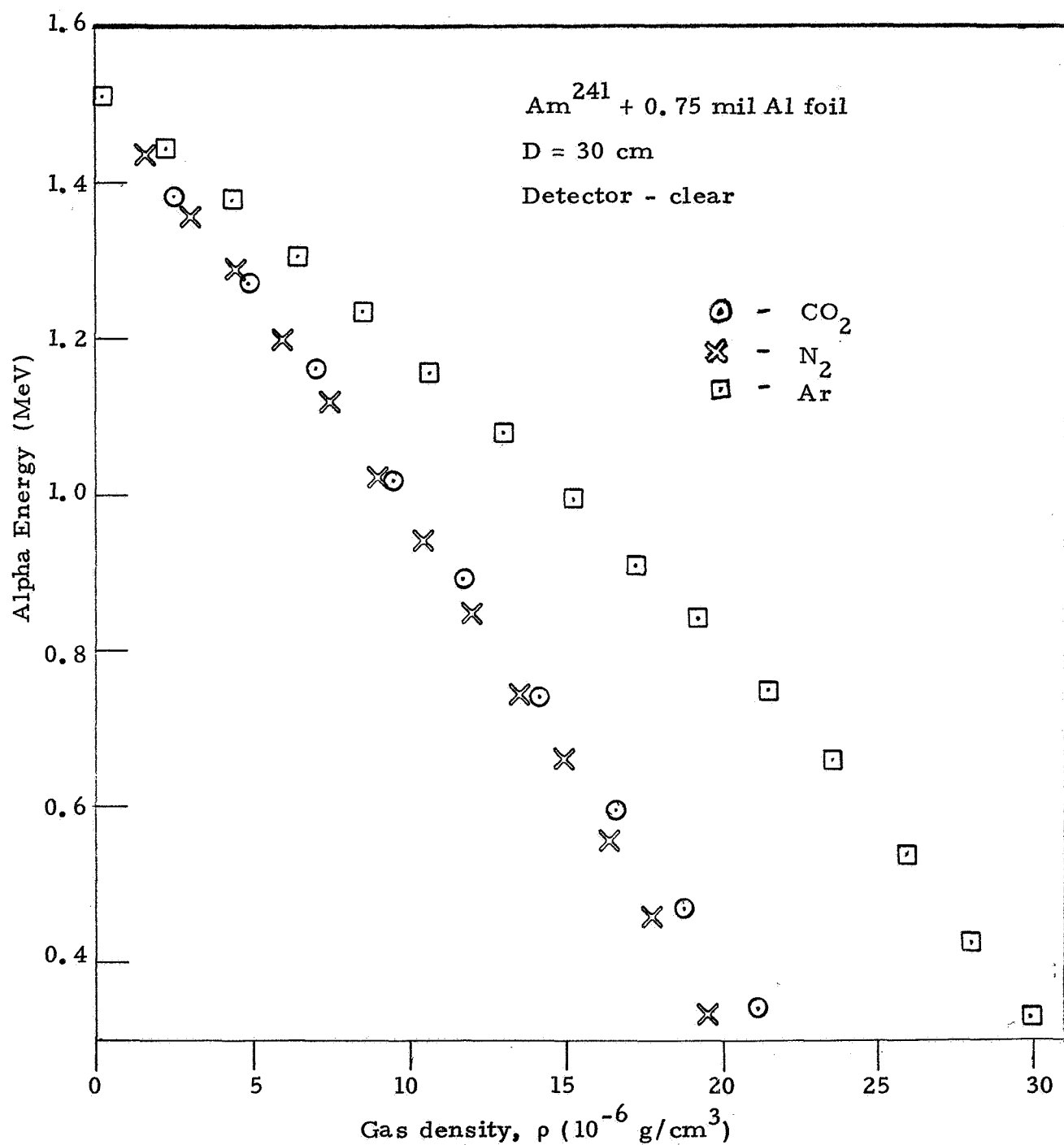


Figure 3.9. Thin Source Calibration Curves for CO₂, N₂ and Ar with an Attenuation Foil over the Source.

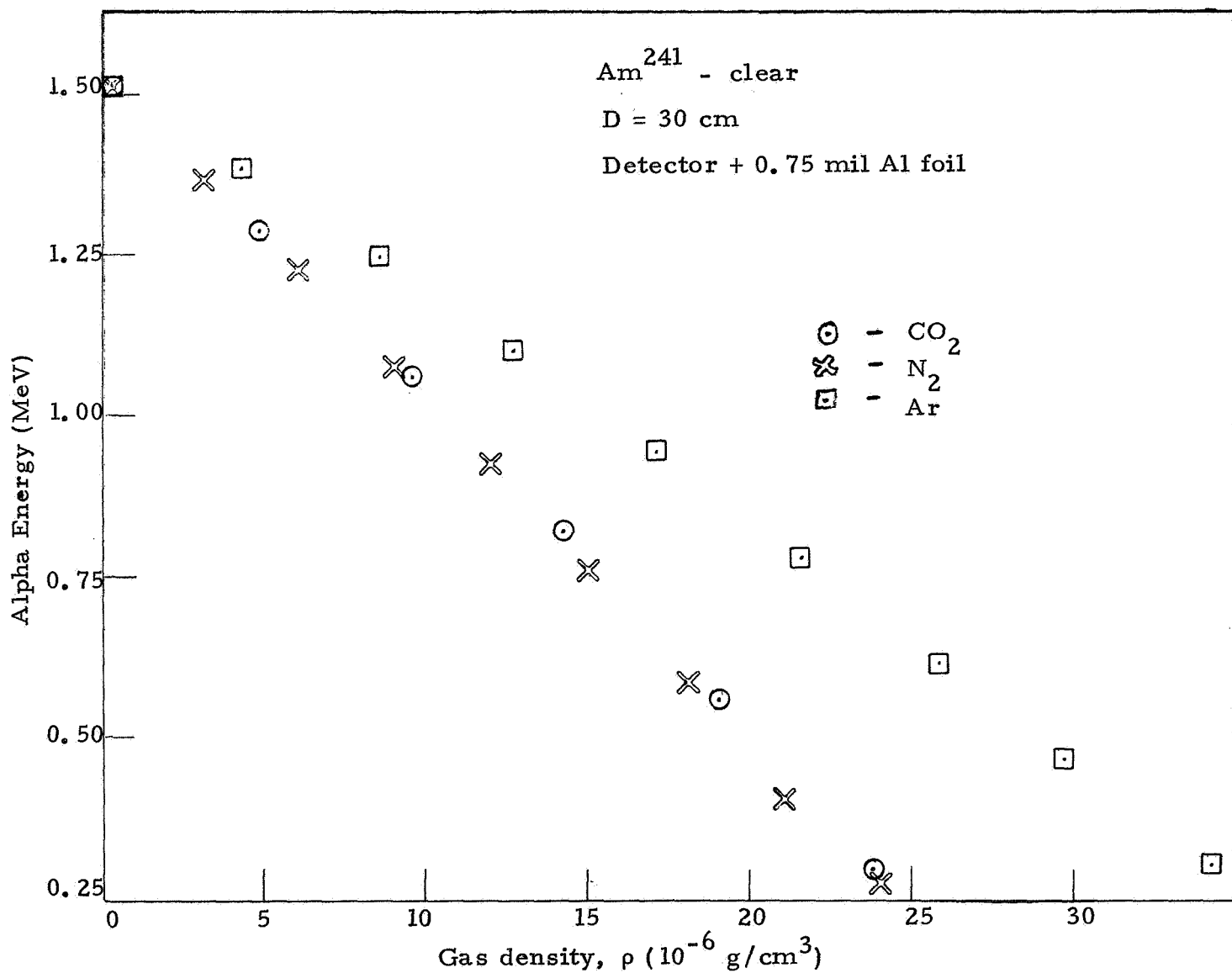


Figure 3. 10. Thin Source Calibration Curves for CO₂, N₂ and Ar with an Attenuation Foil over the Detector.

design is partially qualitative and must weigh the desirabilities of low radiation damage and high count rate.

3.3.1 Discussion of Proton Radiation Damage Studies

The major work on proton radiation damage to silicon solid state detectors which will be described here was reported in References 3.4 and 3.5. These references report on radiation damage to silicon surface-barrier detectors by 50 keV to 5 MeV protons. The measurements were made with totally depleted 100 μ thick n-type silicon of 1700 to 2200 Ω -cm resistivity, and tests were made with front irradiation and rear irradiation.

The basic results of Ref. 3.4 are summarized in Figure 3.11. It is seen that serious changes in detector noise and collection efficiency start at 10^{12} to 10^{13} protons/cm² irradiation, while leakage current increases become important above about 10^{11} protons/cm². For non-penetrating protons (i. e., range less than detector thickness) front entry (through the gold-covered surface barrier) has a greater effect than rear entry (the aluminum covered surface).

Some results from Ref. 3.5 are summarized in Figure 3.12. Here it is seen that noise increases significantly above 10^{12} protons/cm², while leakage current increases above 10^{11} protons/cm² (normal leakage currents are a few tenths microamp). For penetrating protons, front and rear entry produce basically the same results, while for non-penetrating protons rear entry produces less apparent damage.

Additional information on radiation damage to surface-barrier detectors is given by Dearnaley and Northrop (Ref. 3.6), who cite evidence that surface barrier detectors undergo an increase in resistivity as a result of radiation damage, and that totally depleted detectors withstand radiation better than partially depleted detectors. The first effect results in a greater depletion depth for a given bias voltage (for partially depleted detectors), and is in the opposite direction from the effects of an increase in leakage current which (because of the increased voltage drop across the bias resistor) decreases the depletion depth. The results of Scott (References 3.7 and 3.8) for n-on-p silicon diffused-junction detectors under proton and electron irradiation indicate that for proton irradiation the resistivity increases while for electrons it decreases. The results of References 3.4 and 3.5 show that for n-type surface barrier detectors and low energy ($\lesssim 1$ MeV) protons the resistivity decreases, while for higher energy protons the resistivity increases for low bias voltages but decreases for high bias voltages. The higher energy protons do not, however, produce capacity changes as large as those observed at low bias voltages with low energy protons incident on the front of the detector. Capacity changes were significant only for low bias voltages and irradiations above 10^{12} protons/cm². In Ref. 3.4 it was also found that irradiation of the rear of the detectors with low energy protons produced a thin dead layer which was very difficult to

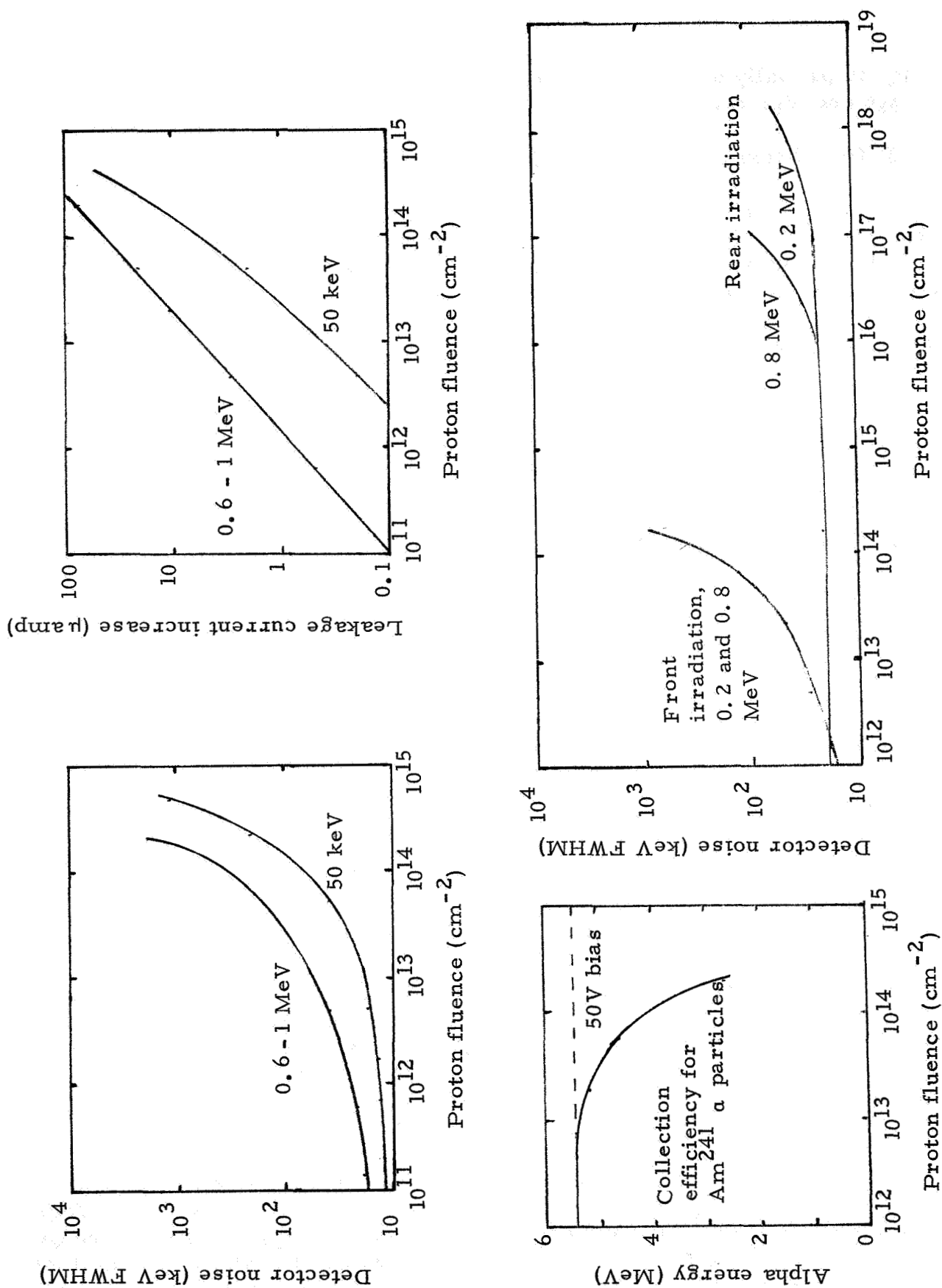


Figure 3.11. Summary of Results on Radiation Damage to Silicon Surface-Barrier Detectors by 50 keV to 1 MeV Protons (Based on Ref. 3.4)

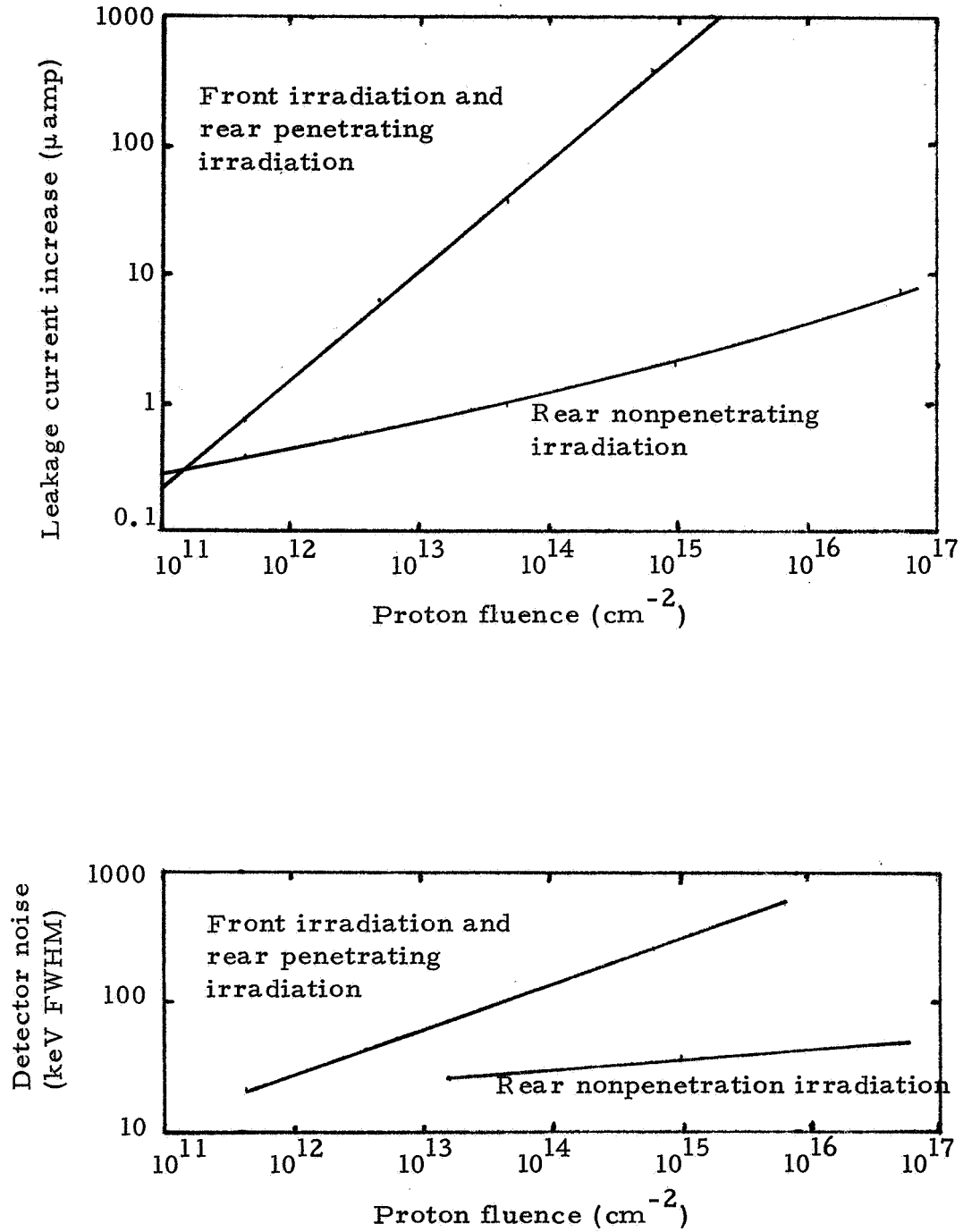


Figure 3.12. Summary of Results on Radiation Damage to Silicon Surface-Barrier Detectors by 0.8-to-5 MeV Protons (Based on Ref. 3.5).

deplete, even though other signs of radiation damage were minimal.

The preceding discussion provides the basis for a few conclusions about the use of silicon surface-barrier detectors for proton detection. First, the maximum usable irradiation is about 10^{12} protons/cm², as detector degradation (noise and leakage current) becomes more severe above this value. Second, a low value bias resistor should be used to avoid large changes in the detector bias voltage because of the increased leakage current above 10^{11} protons/cm². Third, a totally depleted detector should be used to avoid changes in depletion depth (and hence gain) as the leakage current (hence bias voltage) and silicon resistivity change. The leakage current is the first detector characteristic to change appreciably, although changes in resistivity may affect the depletion depth earlier (Ref. 3.6, p 392). Use of an overbiased totally depleted detector reduces, or even eliminates, the effects of these last two changes.

3.3.2 Experimental Results of Alpha Particle Irradiation of Surface-Barrier Detectors

The radiation damage to silicon detectors caused by alpha particles is expected to be more severe than the damage by protons. The stopping power of a given material for alpha particles is approximately (Ref. 3.2)

$$S_a(E_a) = 4 S_p(E_p) \quad (3.36)$$

where $S_p(E_p)$ is the stopping power for protons and

$$\begin{aligned} E_a &= \frac{M_a}{M_p} E_p \\ &= 3.97 E_p \end{aligned} \quad (3.37)$$

Since $S_a(E_a)$ peaks near $E_a = 0.6$ MeV while our interest is for energies above 1 MeV, the result of (3.36) and (3.37) is that $S_a(E_a)$ is generally several times $S_p(E_p)$ for a given energy $E = E_a = E_p$. Thus, the alpha particles lose much more energy in the detector for penetrating particles, and concentrate their energy in a smaller pathlength for non-penetrating particles. Because of the greater energy loss concentration, alpha particles are thus expected to produce a greater amount of radiation damage.

The proton radiation damage studies indicate that alpha particle damage should appear near 10^{10} alphas/cm², since proton effects become visible near 10^{11} protons/cm². To check this experimentally one of the Nuclear Diodes

surface barrier detectors was irradiated with one of the vacuum sublimed Am^{241} alpha sources. The detector was a partially depleted n-type silicon surface barrier detector with a $1000\ \Omega\text{-cm}$ resistivity and a 70V maximum bias rating. The detector had a 1 cm^2 area and was biased at 30-40V during irradiation. The source was positioned 1 cm from the front (gold) surface and with irradiation in air this resulted in a flux of $5.5 \times 10^4\ \alpha'\text{ s}/(\text{sec}\text{-cm}^2)$ of average energy 4.5 MeV. During a period of about 1 month the detector leakage current as a function of bias voltage was periodically measured, and the detector resolution for a full-energy Am^{241} source in vacuum and for a precision pulser were measured. Results are given in Figures 3.13 and 3.14. As shown in Figure 3.13, leakage current increases noticeably by $10^9\ \alpha'\text{ s}/\text{cm}^2$, and increases nearly linearly with alpha fluence. Detector noise as measured by resolution for Am^{241} alphas and a pulser also increase with alpha fluence. At $10^{11}\ \alpha'\text{ s}/\text{cm}^2$ the leakage current has become about $6\ \mu\text{amps}/\text{cm}^2$, and the Am^{241} peak resolution has increased by 60%.

Alpha irradiation of a silicon surface-barrier detector was also made by Dearnaley (References 3.9 and 3.6) with the results shown in Figure 3.15. The irradiations were made using the full 5.5 MeV energy of Am^{241} alphas. The leakage current results are about a factor of 4 greater than those shown in Figure 3.13, while the Am^{241} resolution becomes very bad above $10^{10}\ \alpha'\text{ s}/\text{cm}^2$ in contrast to that shown in Figure 3.13. The latter result as well as the multiple peaking (not observed in our tests) seem to be caused by the low bias voltage used by Dearnaley, which was only 2 volts and resulted in the end-of-range of the $\text{Am}^{241}\ \alpha'$ s lying in the low electric field region near the edge of the depletion layer. When Dearnaley increased the bias to 20V the resolution became much better and the multiple peaking disappeared. Thus, his results are in rough agreement with ours.

The major conclusions to be drawn from the alpha irradiation studies are thus: leakage current increases become important above $10^9\ \alpha'\text{ s}/\text{cm}^2$; the bias voltage must be high enough to provide a large collecting field in the region where the particles lose their energy or else multiple peaking will occur at $10^9\text{-}10^{10}\ \alpha'\text{ s}/\text{cm}^2$, and; the upper limit for detector use appears to be $10^{10}\text{-}10^{11}\ \alpha'\text{ s}/\text{cm}^2$ as leakage current becomes severe above this range and detector resolution becomes appreciably worse.

3.3.3 Limitations Imposed by the Detectors

The results of the preceding sections can now be used to define the characteristics and limitations on the best detector for the alpha particle density measuring system. Because of their compactness, low power requirements, and good energy resolution only semiconductor detectors have been considered. Germanium type detectors have not been considered since they are generally suitable for use only at cryogenic temperatures. Since lithium drifted silicon detectors are about two orders of magnitude more susceptible to radiation damage (References 3.10 and 3.6) they too are excluded from

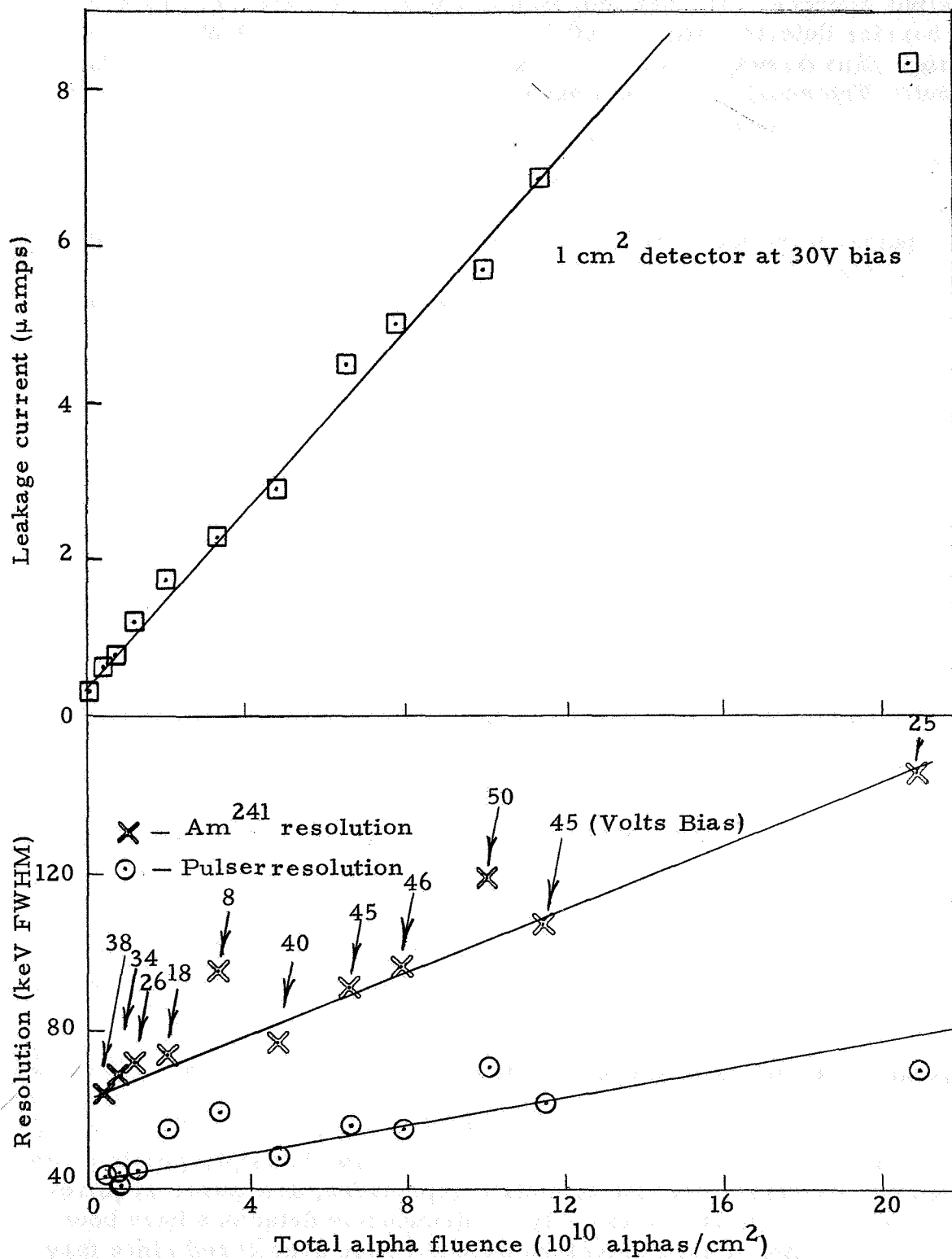


Figure 3.13. Results of 4.5 MeV Alpha Irradiation Tests on a Silicon Surface-Barrier Detector-Leakage Current and Resolution.

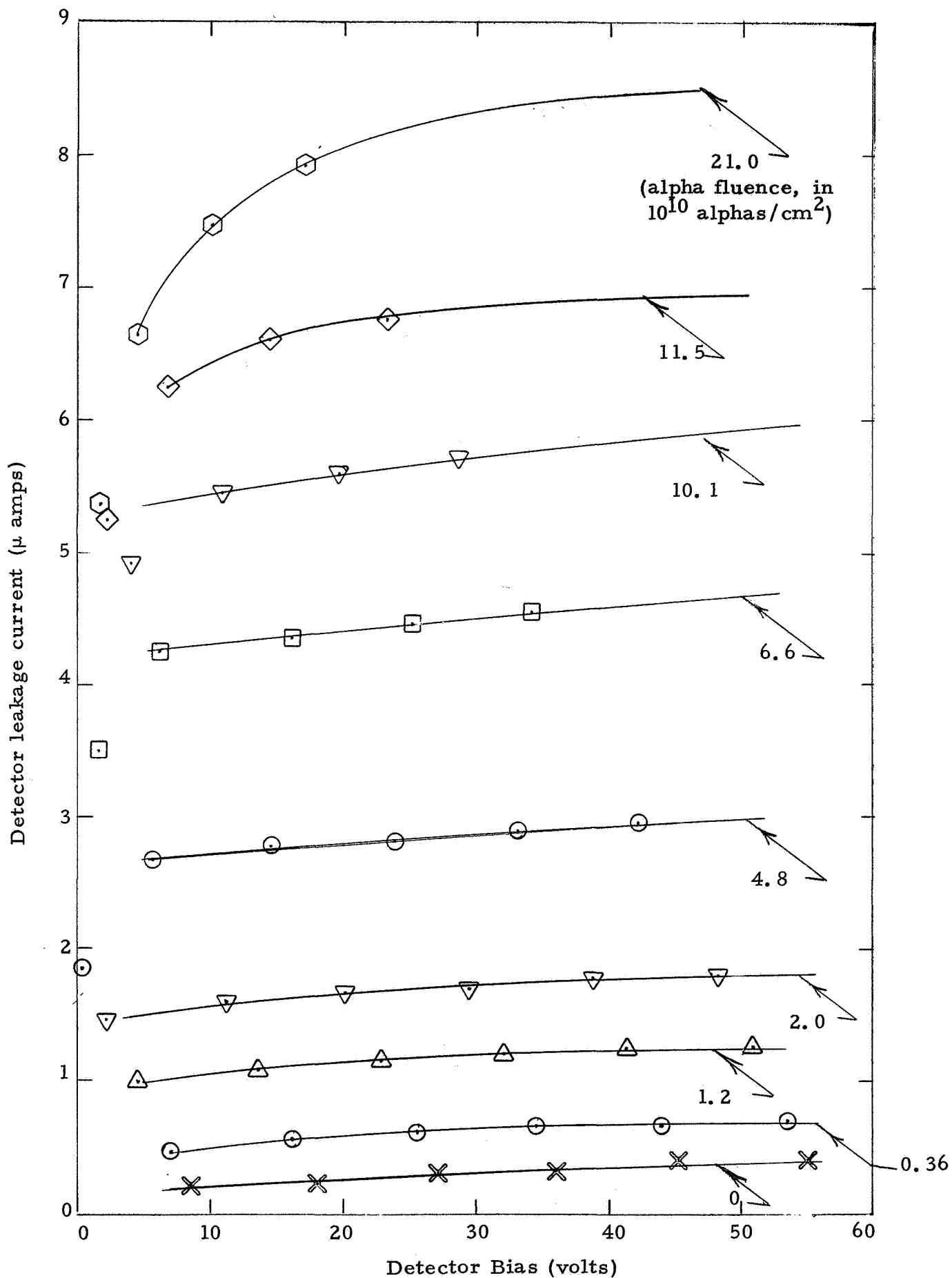


Figure 3.14. Leakage Current vs. Bias Voltage of a Silicon Surface-Barrier Detector after Irradiations by 4.5 MeV Alpha Particles.

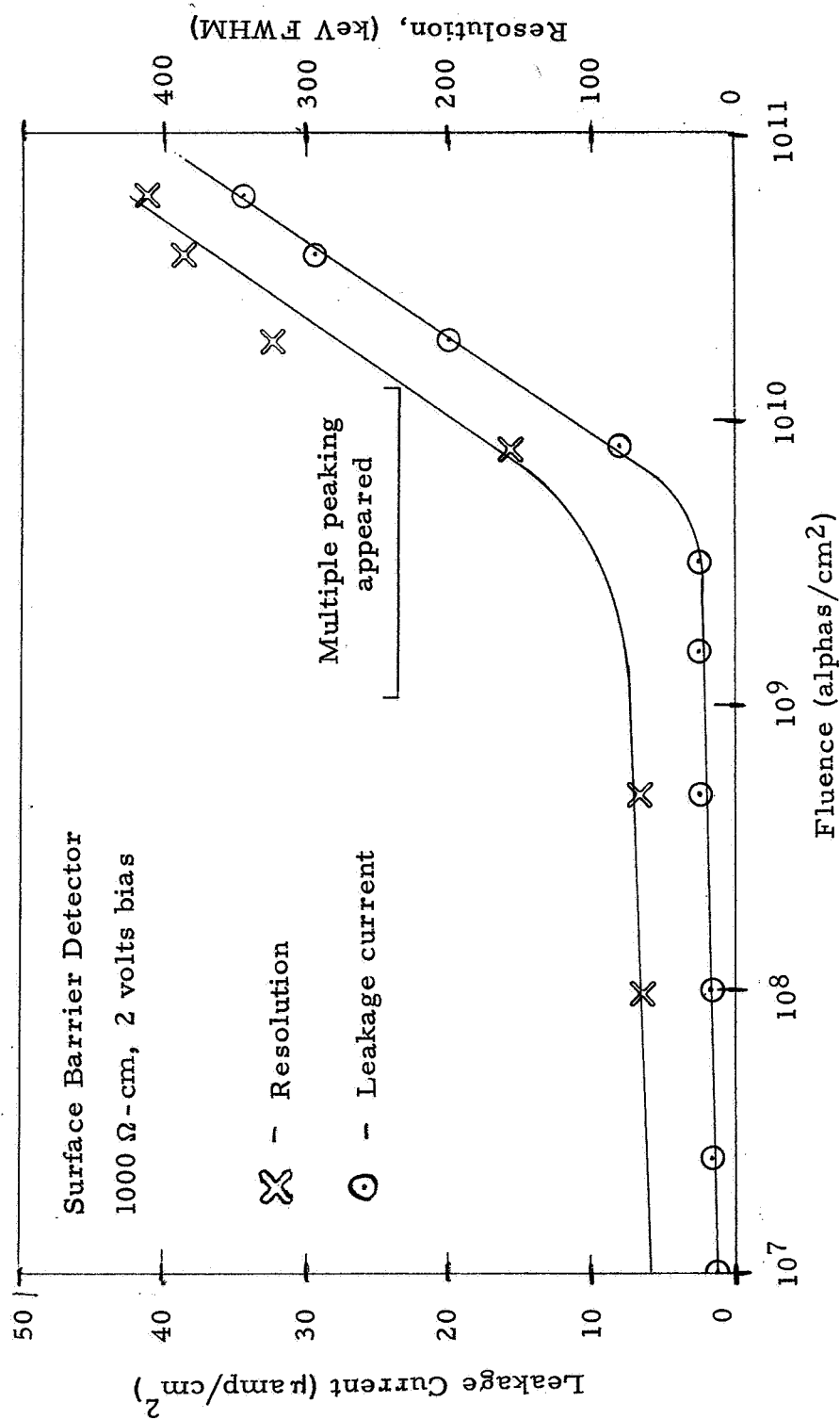


Figure 3.15 Leakage Current and Resolution for Am^{241} vs. Alpha Fluence for a Silicon Surface-Barrier Detector (from Ref. 3.9).

further consideration. Remaining are silicon surface-barrier and diffused junction detectors. Of the two, the surface-barrier detector generally has lower noise levels and consequently better resolution (Ref. 3.6, chap 5), so since their radiation damage properties are substantially the same, the silicon surface-barrier detector is recommended for use in the alpha particle density measuring system.

The data presented in Section 3.3.2 show that the maximum usable alpha fluence for a silicon surface-barrier detector is in the range 10^{10} - 10^{11} α 's/cm². This corresponds to a leakage current of 1-6 μ amps/cm², and possibly higher as shown by the results of Ref. 3.9. Over this range the noise FWHM becomes 45-60 keV from an initial value of 42 keV. The increase in leakage current causes a change in detector bias because of an increased voltage drop across the bias resistor. This results in a decreased depletion depth for a partially depleted detector. Changes in the detector resistivity can also produce changes in the depletion depth. Since a charge sensitive preamp will show some gain changes with variations in the detector depletion depth (hence input capacitance of the preamp), it is recommended that an overbiased totally depleted detector be used. With an overbias of 20V and a 1 M Ω bias resistor a leakage current of up to 20 μ amps can be tolerated.

Since statistical errors in system response can be minimized only by maximizing the detector count rate, it is recommended that a large area detector be used. A suitable detector would be a 4 cm², 300 micron thick totally depleted silicon surface-barrier detector. Such detectors are readily available and have sufficient mechanical strength to withstand shock and vibration. It is recommended that the irradiation fluence be less than 3×10^{10} α 's/cm², or that the maximum flux be 10^3 α 's/(cm²-sec) for one year. This would give a design count rate of 4000/sec for the 4 cm² detector. After this fluence this detector would have a leakage current of 24 μ amps, so with a 1 M Ω bias resistor at least 24V overbias is required.

A number of additional considerations should be mentioned briefly. Since the spacecraft will be in interplanetary space and subject to the full intensity of solar flare radiation, this contribution should be estimated for the time of the flight. This component can only be crudely estimated, however, since solar flares are presently difficult to predict and their most intense particle emissions tend to be localized in space, thus possibly missing the spacecraft. Another consideration is the possible variation in detector response to radiation damage. It may be better to allow for higher leakage currents than expected in order to avoid uncorrectable difficulties during flight.

The statistical error calculations made in later sections are based on a detector count rate of 4000/sec. Source strength calculations are based on 1000 α 's/(sec-cm²) at the detector (4 cm²). The electronic designs allow for a leakage current increase of about 24 μ amps. These numbers represent

approximate upper limits, and may even require decreases to improve system reliability.

3.4 Theoretical Formulation of the Errors

3.4.1 Thin Source System

The errors in the thin source system can be conveniently divided into three categories. First, there is the statistical error which arises from the finite count rate and count time of the detector, and the non-zero width of the measured alpha peak. Second, there are drift errors in the electronic amplifiers and other circuitry. Third, there are errors which may arise as a result of the telemetry system.

The statistical errors arise because of the distribution in measured alpha energies, as illustrated by the spectra in Figure 3.2. The measured alpha spectra can be specified by a true average energy E and standard deviation σ , where

$$E = \sum_i E_i / n \quad (3.38)$$

and

$$\sigma = \left\{ \sum_i (E_i - E)^2 / (n - 1) \right\}^{1/2} \quad (3.39)$$

with n the total number of particles (assumed very large) and the sum over i including all the observed alpha particles. If the energy distribution is approximately gaussian, then it can be readily shown that for a small number N of particles the average \bar{E} defined as

$$\bar{E} = \sum_i E_i / N \quad (3.40)$$

has a standard deviation given by (Ref. 3.11, p 762)

$$\sigma_{\bar{E}} = \sigma / \sqrt{N} \quad (3.41)$$

This value of $\sigma_{\bar{E}}$ is the statistical error in the value of \bar{E} obtained from a finite number N of particles.

For a detector count rate of C α 's/sec, there are two principal ways

of obtaining an average. The circuit can accept particles for a fixed time interval T and average these. In this case $N = CT$ and

$$\sigma_{\bar{E}} = \sigma / \sqrt{CT} \quad (3.42)$$

If C is varying with time, then the measured \bar{E} corresponds most closely to the true value at a time $T/2$ seconds before the circuit stopped accepting pulses (i. e. , at the center of the averaging time). The second type of circuit uses an exponentially decaying memory. In this case a decay time constant of T_e seconds results in an effective memory time of $2 T_e$ seconds (Ref. 3. 11, p 804) so that

$$\sigma_{\bar{E}} = \sigma / \sqrt{2 CT_e} \quad (3.43)$$

and the average applies to a time T_e seconds earlier. Note that this is the same result as (3.42) if we set $T = 2 T_e$. In general, any signal analyzer (see Figure 3. 1) will have an output that is an average over the input for some effective time T seconds. A given electronic circuit may require considerable analysis to determine this time T , but once it is known Eq. (3.42) can be used to give the statistical error, and the measurement applies to a time $T/2$ earlier. The statistical error in \bar{E} is thus

$$\begin{aligned} \delta E_{st} &= \sigma_{\bar{E}} \\ &= \sigma / \sqrt{CT} \end{aligned} \quad (3.44)$$

The electronic drift error arises primarily from changes in amplifier gains. These changes are not statistical and thus provide a constant bias to the system response. Two components of electronic drift can be distinguished. The long term aging (about six months during flight) of the electronics may introduce a shift on the order of a percent, but this can be eliminated by calibration in vacuum before the lander entry into the Martian atmosphere. A second component of drift occurs when the detector and electronics undergo temperature changes and possible interaction with the Martian atmosphere. The latter may be known only within certain limits, and it is this component that we now consider. If the amplifier gain changes by a fraction f , then the change in average alpha energy \bar{E} is

$$\delta \bar{E}_{\text{drift}} = f \bar{E} \quad (3.45)$$

Note that if the system cannot be calibrated before entry, then the long term drifts can be accounted for by an increase in the value of f in (3.45). It is expected that the value of f will typically be 0.005 or less.

Finally, the telemetry errors depend on the form used for the system output and the properties of the telemetry system. If a digital system output is used there should be no telemetry errors other than catastrophic failures. If the system provides an analog output then telemetry may introduce errors of perhaps 1%. For the present we simply express this as $\delta \bar{E}_{TM}$ and discuss it in more detail later.

Some values for \bar{E} , σ , $\delta \bar{E}_{st}$, and $\delta \bar{E}_{drift}$ are given in Table 3.1. These are based on measurements made with an Am^{241} vacuum sublimed source and a 0.5 MeV threshold. $\delta \bar{E}_{st}$ is calculated for $CT = 4000$ a's, while $\delta \bar{E}_{drift}$ is for $f = 0.005$. It should be noted that σ depends almost completely on \bar{E} , and is largely independent of the method used to reduce the energy of the Am^{241} 5.48 MeV α particles, whether it be thin foils or various gases.

The errors in the density are obtained from the errors in the average energy by the relation

$$\delta \rho_m = \left| \frac{d\rho}{d\bar{E}} \right| \delta \bar{E} \quad (3.46)$$

which from (3.4) becomes

$$\delta \rho_m = \frac{1}{DS(\bar{E})} \delta \bar{E} \quad (3.47)$$

Equation (3.47) will give three components to the density error, corresponding to the three components of $\delta \bar{E}$, i. e., statistical, drift, and telemetry errors. Increasing the detector count rate or averaging time T will generally decrease only the statistical error. Thus, in averaging several measurements only the statistical error should be reduced. The drift errors will generally be systematic, depending primarily on the temperature of the electronics, the power supply voltages, and the aging drift in component values. By measuring the temperature of the electronics during the density measurements a portion of the temperature drift errors may be eliminated. Drift in component values during flight may be corrected by calibration in vacuum before entry, but any component value changes arising from the shock and heating of entry are likely to be uncorrectable. The precise behavior of the drift must be determined by measurements on a prototype. For the present, we assume that the drift (and telemetry) errors can be approximated by a gaussian distribution (e. g., a $\pm 10^\circ C$

Table 3. 1

Values of \bar{E} , σ , $\delta \bar{E}_{st}$ and $\delta \bar{E}_{drift}$ for an Am²⁴¹ Alpha Source

Average Alpha Energy, \bar{E} (MeV)	Standard Deviation σ (MeV)	Statistical Error for 4000 Counts, $\delta \bar{E}_{st}$ (keV)	Electronic Drift Error for 0.5% Drift, $\delta \bar{E}_{drift}$ (keV)
5.5	0.38	6.0	28
4.0	0.24	3.8	20
3.0	0.17	2.7	15
2.0	0.13	2.1	10.0
1.5	0.12	1.9	7.5
1.0	0.12	1.9	5.0

temperature variation is more likely than a $\pm 25^{\circ}\text{C}$ variation) and thus combine the three error components on an rms basis. Note, however, that the drift and telemetry errors should not be reduced when two density measurements are combined. Using this method we can obtain reasonable estimates of the system accuracy. Thus the form for $\delta \bar{E}$ is chosen as

$$\delta \bar{E} = \left\{ \left(\delta \bar{E}_{\text{st}} \right)^2 + \left(\delta \bar{E}_{\text{drift}} \right)^2 + \left(\delta \bar{E}_{\text{TM}} \right)^2 \right\}^{1/2} \quad (3.48)$$

Finally, if no composition information is available there will be an additional uncertainty in ρ given by

$$\delta \rho_c = \xi \rho \quad (3.49)$$

where ξ is defined in Eq. (3.35). The precise value used for ξ depends on the atmospheric compositions which are considered likely, and also on the density and effective threshold of the system. For calibration in CO_2 and use in Ar (composition not known, however), the approximate maximum value for ξ of 0.49 is obtained (see also the discussion in Section 3.2.2). The overall error in ρ can then be taken as

$$\delta \rho = \delta \rho_m + \delta \rho_c \quad (3.50)$$

where the errors are now added linearly to show explicitly that $\delta \rho_c$ is a systematic error that cannot be reduced without composition information.

3.4.2 Thick Source System

The errors in the thick source system can be divided much the same as for the thin source system. Again, if the signal analyzer has an effective counting time of T ($= 2 T_e$ for an exponential weighting function) then the measurements apply to a time $T/2$ earlier.

The statistical errors arise from the finite count rate $C(\rho)$, which results in CT counts with a standard deviation of \sqrt{CT} counts. This gives an error in the measured value of C of

$$\delta C_{\text{st}} = \sqrt{C/T} \quad (3.51)$$

We next discuss the telemetry errors which contribute δC_{TM} for an analog output and effectively nothing for a digital output. These two then give a density error of

$$\delta \rho_a = \left| \frac{d\rho}{dC} \right| \left\{ \left(\delta C_{st} \right)^2 + \left(\delta C_{TM} \right)^2 \right\}^{1/2} \quad (3.52)$$

The density error arising from drifts in the electronic threshold E_{th} can be calculated directly by differentiation of Equations (3.12) and (3.12a) to give

$$\delta \rho_{drift} = \frac{1}{DS(E'_{th})} \frac{S_f(E'_{th})}{S_f(E_{th})} \delta E_{th} \quad (3.53)$$

For a 0.04 mil gold foil with $E'_{th} = 1.0$ MeV, $E_{th} = 0.225$ MeV, this becomes (for CO_2)

$$\delta \rho_{drift} = \frac{1.08 \times 10^{-3}}{D} \delta E_{th} \quad (3.54)$$

with $\delta E_{th} \approx 0.005 E_{th}$. The error in the measured value of ρ is then

$$\delta \rho_m = \left\{ \left(\delta \rho_{drift} \right)^2 + \left(\delta \rho_a \right)^2 \right\}^{1/2} \quad (3.55)$$

The errors because of composition information are the same as given in Section 3.4.1 in Eq. (3.49), with the overall error in ρ given by (3.50).

4. DENSITY MEASUREMENT-EXPERIMENTAL RESULTS AND PROPOSED SYSTEM DESIGNS

The experimental calibration curves for the alpha particle density measuring systems were taken with the set-up shown in Figure 4.1. This set-up was also used to obtain the stopping powers presented in Section 3.2.1. The alpha sources and the detector were located inside a vacuum chamber which allowed measurements to be made at various densities of CO_2 , N_2 and Ar, as well as mixtures of these gases. As discussed in Section 3.2.1, energy losses in the gases are best confined to alpha particles greater than 1 MeV to minimize differences in the CO_2 and N_2 stopping powers. Statistical errors of the systems are calculated for a maximum count rate of 4000/sec, which is the approximate limit obtained from Section 3.3.

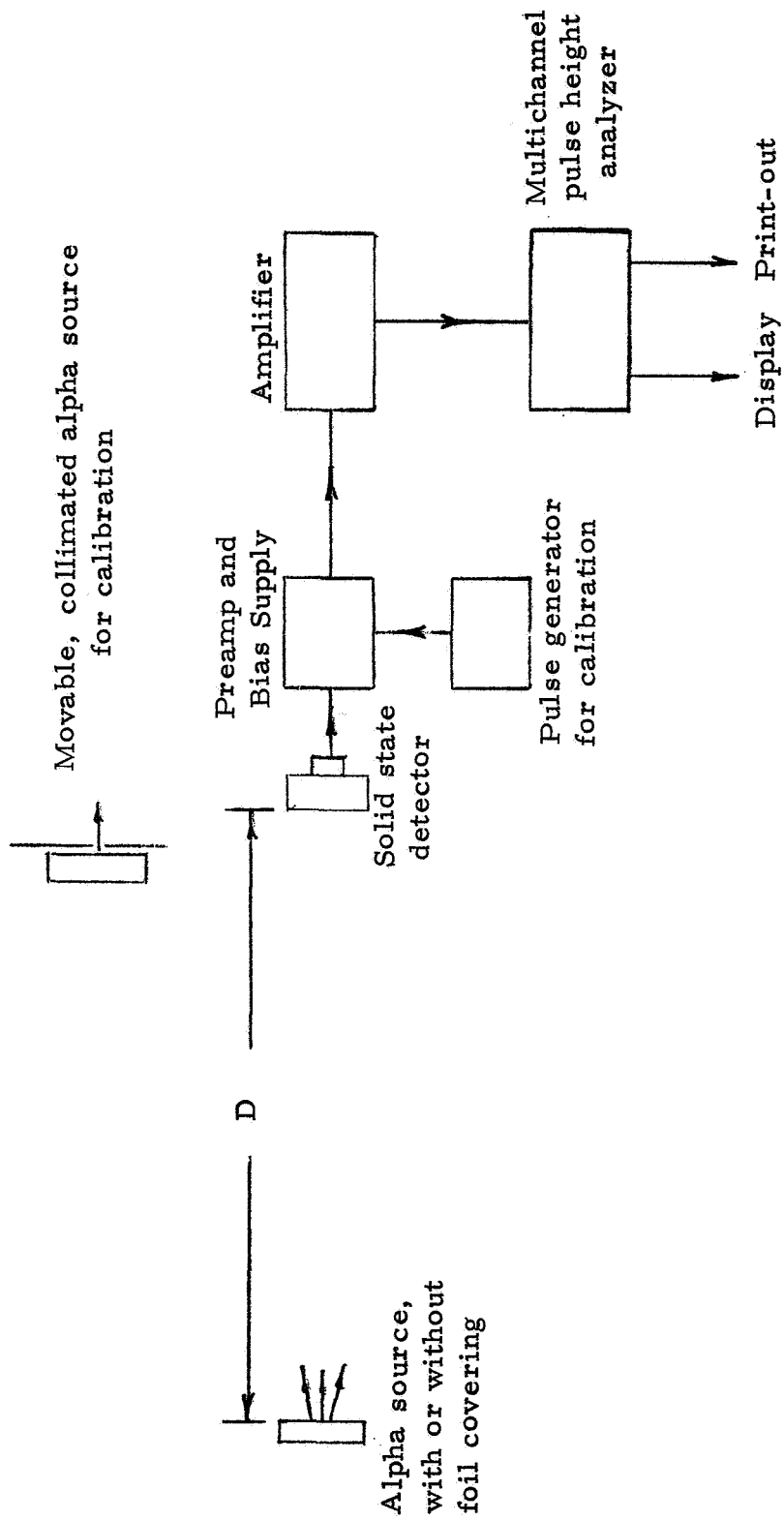


Figure 4.1. Geometry for Thick and Thin Source Configuration Tests

4.1 Thin Source Method

The thin source method has been investigated using vacuum sublimed Am^{241} sources and a Po^{210} foil source. The basic properties of Am^{241} and Po^{210} are listed in Table 4.1, along with the properties of Cm^{242} which has recently become available in greater quantities. The data are taken from References 4.1, 4.2, and 4.3. Spectra of an Am^{241} source, uncovered and with a 0.2 mil Ni foil covering, and of the Po^{210} foil source are shown in Figure 4.2. Note that the Po^{210} foil source spectrum has a significantly greater width than the Am^{241} source with the Ni foil covering, even though the average alpha energies are not very different.

4.1.1 Experimental Calibration Curves

Calibration curves for the thin source method were taken primarily to verify the theoretical conclusions made in Section 3. Tests were made mostly with an uncovered vacuum sublimed Am^{241} source, and with this source covered with a 0.2 mil Ni foil.

The analysis in Section 3 shows that at low gas densities the thin source calibration curve can be rewritten as (see Eq. (3.3))

$$E = E_0 - \rho DS \quad (4.1)$$

where E_0 is the initial alpha energy and S is an average stopping power approximately equal to the value for alphas of energy E_0 . For a mixture of CO_2 , N_2 and Ar

$$\begin{aligned} S &= w_{\text{CO}_2} S_{\text{CO}_2} + w_{\text{N}_2} S_{\text{N}_2} + w_{\text{Ar}} S_{\text{Ar}} \\ &\approx (1 - w_{\text{Ar}}) S_{\text{CO}_2} + w_{\text{Ar}} S_{\text{Ar}} \end{aligned} \quad (4.2)$$

where it is assumed that $S_{\text{CO}_2} \approx S_{\text{N}_2}$. The use of Eq. (4.1) is illustrated in Figure 4.3 which shows some calibration points for CO_2 , N_2 and Ar with a full energy (5.48 MeV) Am^{241} source.

Results of using (4.1) on various gas mixtures are plotted in Figure 4.4. The plots show that Eq. (4.2) holds within the errors of the measurements (indicated by bars on the right side of the graph). The ratios of Ar to CO_2 stopping powers are also given in Figure 4.4 and compared with the theoretical ratio obtained from the calculations of Ref. 3.1. Table 4.2 lists some average stopping power values for several gas mixtures at different source-detector separations.

Table 4. 1

Properties of Some Alpha Emitters Suitable for
Thin Source Manufacture

- a) Am²⁴¹ - half-life = 458 years
- melting point > 850°C

Radiation	Energy (MeV)	%/disintegration
α	5.545	0.25
	5.513	0.12
	5.486	86.0
	5.443	12.7
	5.389	1.33
γ	0.060	36
Np L x-rays	0.012-0.022	38

- b) Po²¹⁰ - half-life = 138 days
- melting point = 254°C

Radiation	Energy (MeV)	%/disintegration
α	5.305	100

- c) Cm²⁴² - half-life = 163 days
- melting point = (high?)

Radiation	Energy (MeV)	%/disintegration
α	6.115	74
	6.071	26

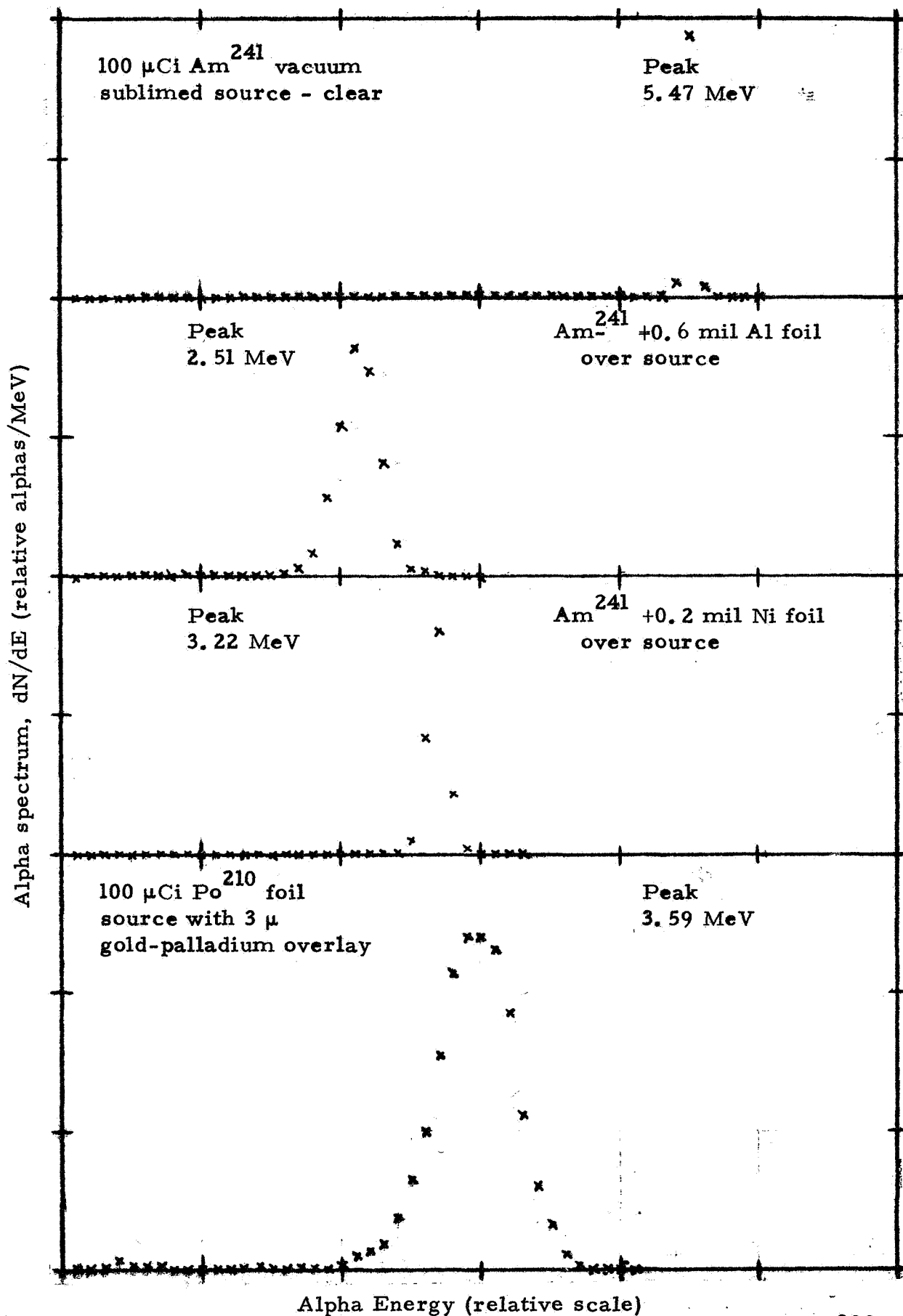


Figure 4.2 Spectra of an Am^{241} Vacuum Sublimed Source and of the Po^{210} Foil Source.

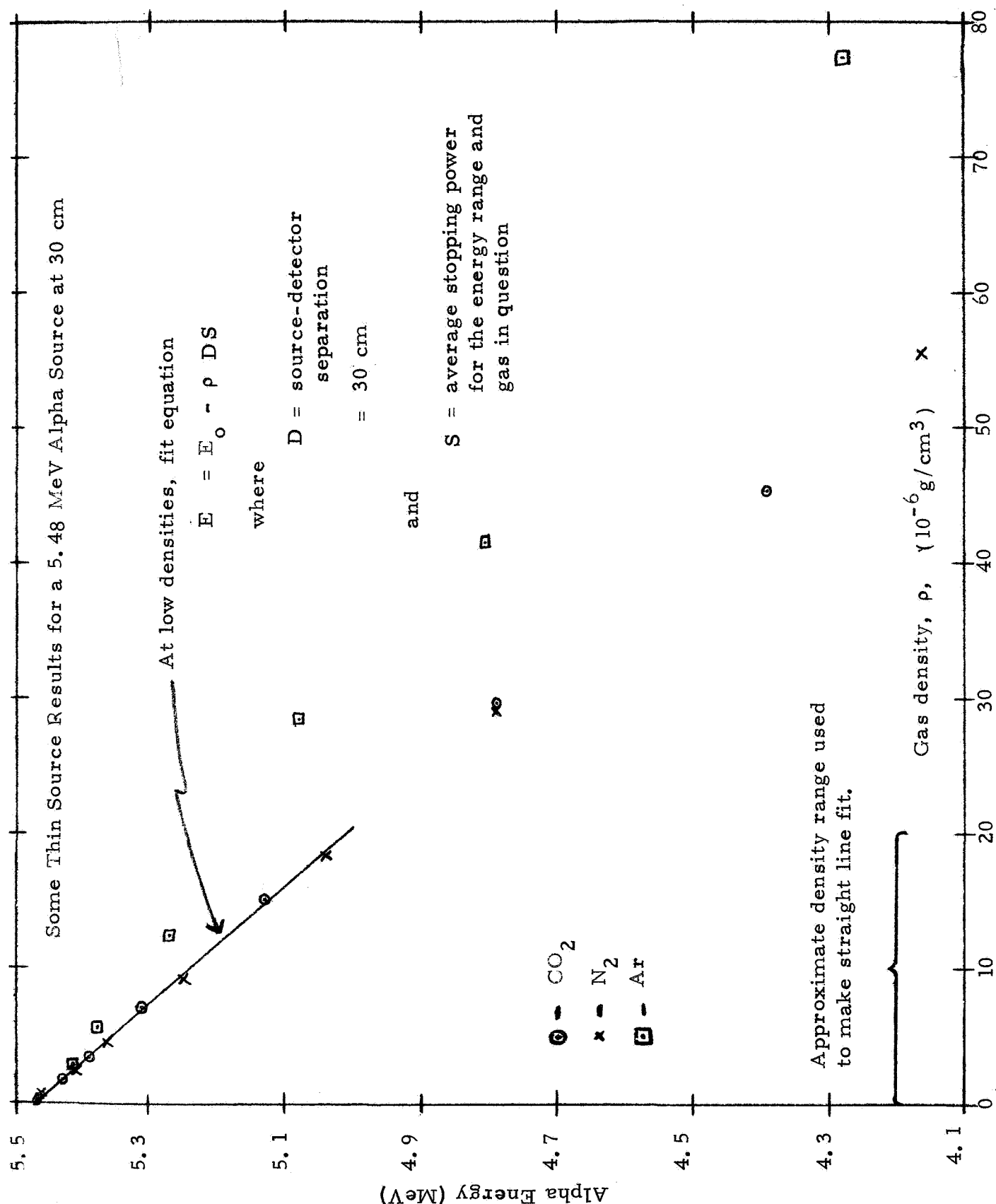


Figure 4.3 Calibration Points for CO_2 , N_2 and Ar with 5.48 MeV Am^{241} Source, Showing Region of Straight Line Fit at Low Densities.

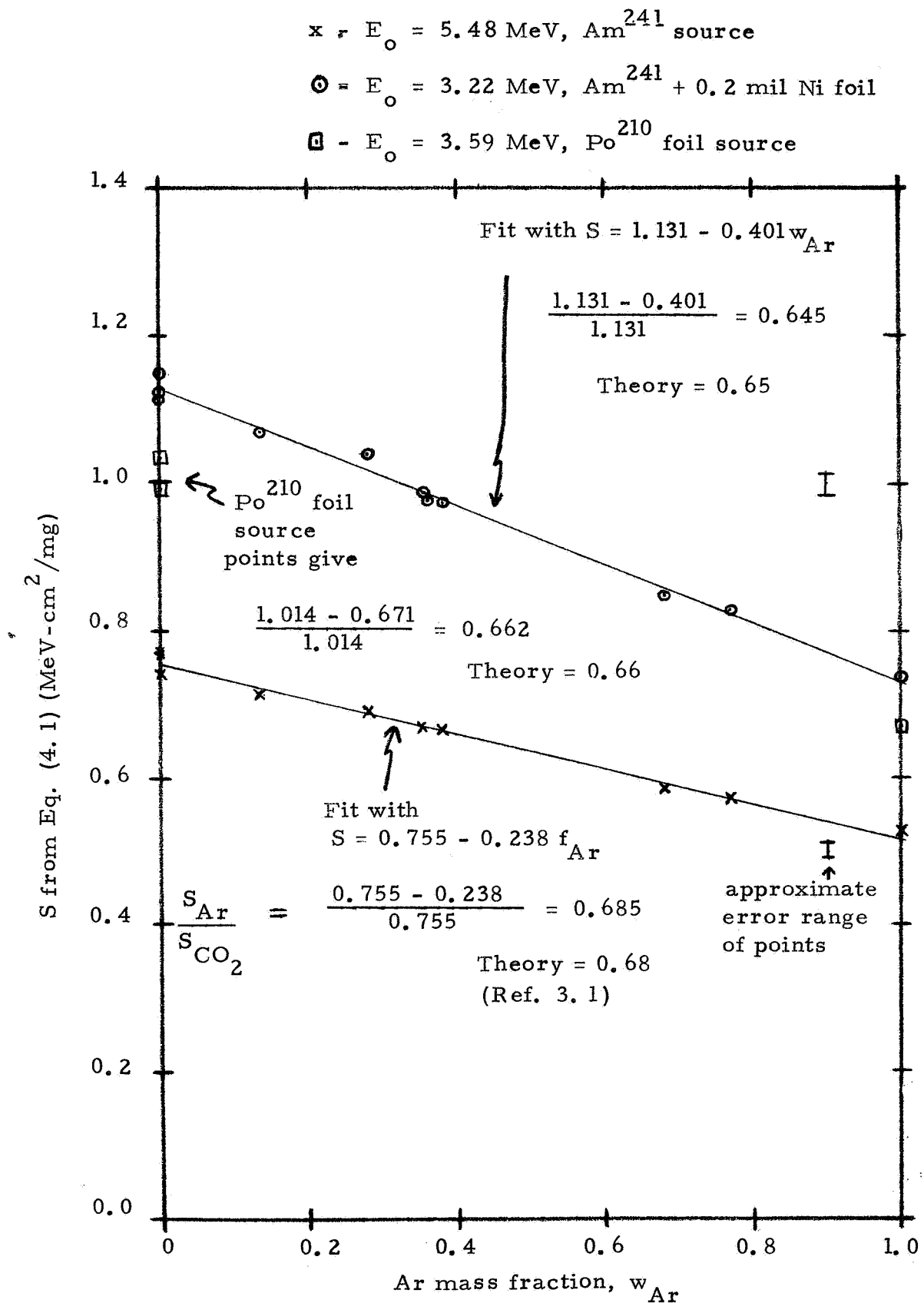


Figure 4.4 Plots of Average Stopping Power vs. Argon Mass Fraction of Gas.

Table 4.2

Comparison of Some Average Stopping Powers

$$\text{Fits of } E = E_0 - \rho D S$$

a) $E_0 = 5.48 \text{ MeV}$, Am^{241} source - uncovered

Gas Composition (Volume %)	S [MeV/(mg/cm ²)]		
	D = 10 cm (S ± 0.02)	D = 30 cm (S ± 0.02)	D = 100 cm (S ± 0.03)
100% CO ₂	0.76	0.76	0.78
100% N ₂	0.77	0.78	0.80
100% Ar	0.53	0.53	
70% CO ₂ + 30% Ar		0.69	0.70
70% N ₂ + 30% Ar		0.67	0.62
$\frac{1}{3}$ CO ₂ + $\frac{1}{3}$ N ₂ + $\frac{1}{3}$ Ar		0.69	0.75

b) $E_0 = 3.59 \text{ MeV}$, Po^{210} foil source - uncovered

Gas Composition (Volume %)	S [MeV/(mg/cm ²)]	
	D = 30 cm (S ± 0.03)	D = 100 cm (S ± 0.05)
100% CO ₂	0.99	1.18
100% N ₂	1.04	1.03

The data shown in Table 4.2 and Figure 4.4 bring experimental support to two major conclusions of Section 3.1. From Table 4.2 it is seen that a calibration curve should depend only on ρD , and thus measurements made at one value of D can be easily transformed to another value. The results of Figure 4.4, which substantiate the form of Eq. (4.2), provide experimental verification for Eq. (3.32) (also verified by the stopping power measurements shown in Section 3.2) and in particular its application in Eq. (3.11). Note that Equations (3.33) and (3.34), with the N_2 coefficient (1.035) set equal to 1, have been shown to hold to within a few percent, at least over the range 5.5 to 3 MeV. The stopping power measurements (Section 3.2.1) show that within about 2% the following relation should hold (assuming a system calibrated with CO_2)

$$\rho_m = (\rho_{CO_2} + \rho_{N_2}) + 0.67 \rho_{Ar} \quad (4.3)$$

for density ranges where the alpha energy losses are for particles greater than 1 MeV. Note that (4.3) cannot hold to better than about 2% if significant amounts of N_2 are present. Under such conditions (3.34) would have to be used along with composition information for all three components, N_2 , CO_2 and Ar. If measurement accuracies of better than 1% are desired, then very precise composition information is required and the procedure using Eq. (3.8) must be employed.

Some complete calibration curves are plotted in Figures 4.5 and 4.6. The effective density plotted is

$$\rho_{eff} = \rho_{CO_2} + \rho_{N_2} + 0.67 \rho_{Ar} \quad (4.4)$$

for Figure 4.5 which is for a 5.48 MeV Am^{241} source, while for Figure 4.6

$$\rho_{eff} = \rho_{CO_2} + \rho_{N_2} + 0.65 \rho_{Ar} \quad (4.5)$$

for the 3.22 MeV from an Am^{241} source covered with 0.2 mil Ni. The lowered effective Ar density ($0.65 \rho_{Ar}$) is a better value for the range 3 to 1 MeV, while $0.67 \rho_{Ar}$ is best for the range 5.5 to 1 MeV.

Figure 4.5 shows that (4.4) holds to within a few % for a number of Ar concentrations. Since 1 MeV alpha energy corresponds to $140 \times 10^{-6} \text{ g/cm}^3$, the full energy Am^{241} source can be used at a source-detector separation of about 55 cm if a range of $0-80 \times 10^{-6} \text{ g/cm}^3$ of CO_2 is desired. Figure 4.6 shows a similar plot for Am^{241} + 0.2 mil Ni foil at 30 cm from the detector. Again, the results show that (4.5) holds to a few % for a variety of gas compositions, limited of course to CO_2 , N_2 and Ar.

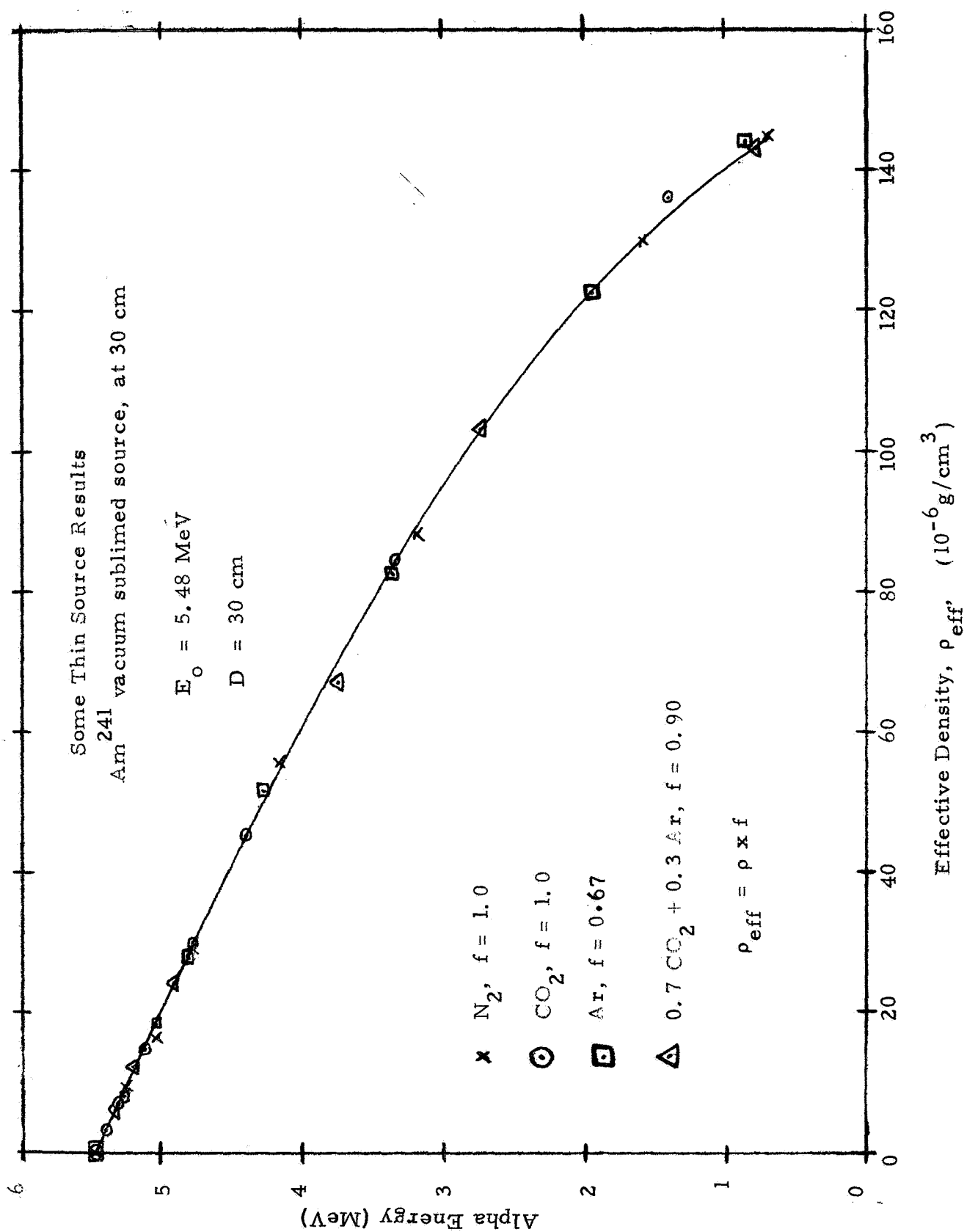


Figure 4.5 Calibration Curve for Am^{241} (5.48 MeV) at 30 cm.

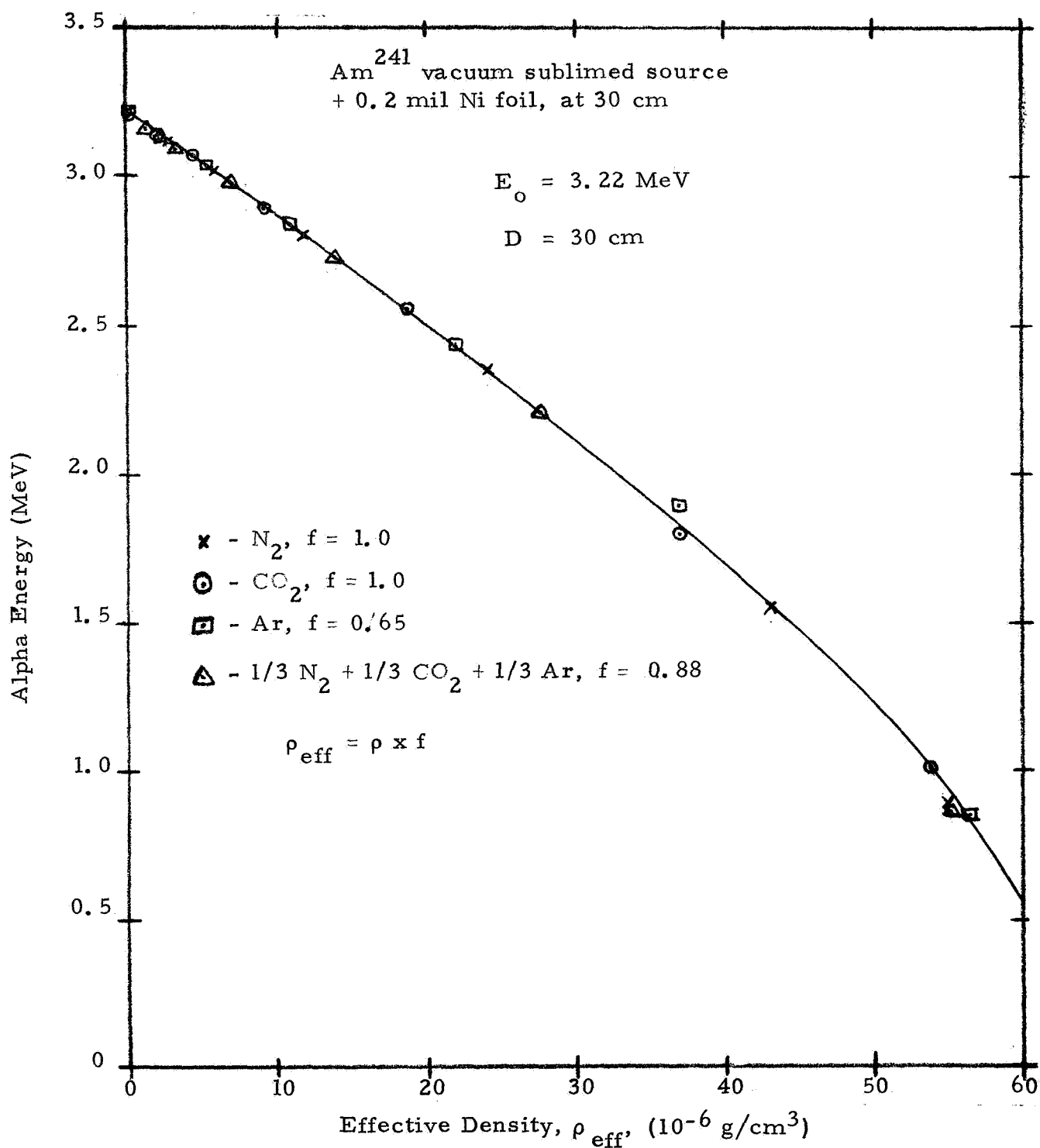


Figure 4.6 Calibration Curve for Am²⁴¹ (3.22 MeV) at 30 cm.

Calibration curves for 1.53 MeV alphas were shown earlier in Figures 3.9 and 3.10. These figures illustrate the form of the curves when actual rather than effective density is plotted. The results of these two figures show that an energy cut-off lower than 1 MeV can be used if a foil covering is placed over the detector. Such a system, while having a slightly different calibration curve, will not yield significantly different results from a system using a slightly higher alpha energy and a 1 MeV cut-off energy.

Table 4.3 lists some thin source system parameters. These are based on a maximum density of $80 \times 10^{-6} \text{ g/cm}^3$ of CO_2 to reduce the alpha energy to about 1 MeV. Source strengths are calculated to give a flux of $1000 \text{ } \alpha' \text{ s/}(\text{sec-cm}^2)$ at the detector. The statistical errors are taken from Table 3.1 and are for 4000 counts (a 1 second averaging time at $4000 \text{ } \alpha' \text{ s/sec}$ count rate).

4.1.2 Expected Errors for the Thin Source Method

The errors for the thin source method are calculated from Eq. (3.47). For the present two cases are considered, $\delta \bar{E}_{\text{TM}} = 0$ and $0.01 E_0$ in (3.48). Under these conditions the system errors listed in Table 4.4 are obtained. An electronic drift error of 0.5% is assumed, so values of $\delta \bar{E}_{\text{st}}$ and $\delta \bar{E}_{\text{drift}}$ have been taken from Table 3.1.

The values of $\delta \rho_{\text{st}}$ are the pure statistical component of the density error, while $\delta \rho_1$ has an 0.5% electronic drift error added and $\delta \rho_2$ has an additional 1% telemetry error added (both on an rms basis). Errors are listed only for 0 and $80 \times 10^{-6} \text{ g/cm}^3$ density, since errors for intermediate densities are approximate interpolations of the extreme errors. Also given in Table 4.4 are the 2% errors, which are the limits for density accuracy if only Ar composition information is available. It should be noted that if electronic drift errors are reduced to 0.1% then they become equal to the statistical errors and $\delta \rho_1 \approx \sqrt{2} \delta \rho_{\text{st}}$.

The results shown in Table 4.4 allow three main conclusions to be made. First, the thin source system error is minimum for high alpha source energies and large separations, although the change for energies greater than 3 MeV (and separation greater than 18 cm) is not very significant. Second, the thin source system provides greatest accuracy at high densities both on an absolute error and a relative error basis. Third, for 4000 counts the statistical errors are not important if electronic drift and telemetry errors are greater than 0.1%.

4.1.3 Alpha Source Manufacture, Reproducibility and Stability

Experimental data have been accumulated on the stability of two types of alpha sources for the thin source configuration. One type is Am^{241} vacuum sublimed on a platinum backing, and data have been obtained for four sources of this type. The other type, of which one was tested, is a Po^{210} foil source with a 3 micron gold-palladium face. The sources were manufactured by The

Table 4.3

Some Thin Source System Parameters

System based on Am²⁴¹ vacuum sublimed sources, with foils to reduce energy. Separations are calculated to reduce the alpha energy to 1 MeV at 80×10^{-6} g/cm³ of CO₂. Statistical error is for 4000 counts (from Table 3.1).

Initial Alpha Energy (MeV)	Statistical Error, $\delta \bar{E}_{st}$ (keV)	Source-detector separation D (cm)	Source Activity for $1000 \alpha' s / (\text{sec-cm}^2)$ at the detector	
			(dps)	(μ Ci)
5.5	6.0	55	3.80×10^7	1030
4.0	3.8	31	1.21×10^7	330
3.0	2.7	18	4.07×10^6	110
2.0	2.1	7.5	7.07×10^5	19
1.5	1.9	3.3	1.37×10^5	3.7
1.0	1.9	-	-	-

Table 4.4

Expected Errors for the Thin Source System

Initial Alpha Energy E_0 (Mev)	Source- detector separation D (cm)	Error at 0 g/cm ³ density (10 ⁻⁶ g/cm ³)			Error at 80 x 10 ⁻⁶ g/cm ³ density (10 ⁻⁶ g/cm ³)		
		$\delta \rho_{st}$	$\delta \rho_1$	$\delta \rho_2$	$\delta \rho_{st}$	$\delta \rho_1$	$\delta \rho_2$
5.5	55	0.15	0.72	1.6	0.02	0.05	0.56
4.0	31	0.14	0.74	1.6	0.03	0.10	0.72
3.0	18	0.14	0.80	1.8	0.06	0.16	0.94
2.0	7.5	0.20	0.97	2.1	0.14	0.39	1.5
1.5	3.5	0.34	1.4	3.0	0.30	0.84	2.5
		(2% error = 0.0)			(2% error = 1.6)		

Note: $\delta \rho_1$ is with a 0.5% electronic drift error, and $\delta \rho_2$ is with an additional 1% full scale telemetry error, both added to the statistical error on an rms basis.

Radiochemical Centre, Amersham, England, and can be obtained from their American representative, Amersham/Searle (Des Plaines, Illinois, U. S. A.).

The Am^{241} sources have a nominal activity of $100\mu\text{ Ci}$ on a 7mm diameter area. The platinum foils are mounted on 25 mm diameter x 5 mm thick aluminum holder, and the overall source weighs 6.9 g. Table 4.5 lists some data obtained on the four Am^{241} sources over a period of six months. It should be noted that the activity is constant within experimental error (about 3% or $1\mu\text{ Ci}$), and that the standard deviation on the alpha peak is constant in time and equal to about 40 keV for all four sources. The standard deviation for particles above 0.5 MeV is also shown to be roughly constant at 0.4 MeV. Values for this standard deviation are not given for the earliest set of measurements since a different detector was used, and that detector had an additional low energy background produced by particles striking a ring of silicon between the sensitive area and the guard ring. The measured source intensities and resolutions show that source manufacture is reproducible, although all four sources are a factor of three less than their nominal intensities.

The Am^{241} sources with a platinum backing are considered more stable than those with a stainless steel backing (Ref. 4.4). Activities to $100\mu\text{ Ci/cm}^2$ will easily pass wipe tests. Higher specific activities may result in flaking of the Am^{241} layer if the foil is bent, but a thin gold covering and a rigid mount should prevent this from happening. Source energy can easily be adjusted by evaporating gold over the Am^{241} . These sources should be able to survive the Martian lander heat treatment, although possible reaction of the Am^{241} with the decontamination atmosphere would have to be checked experimentally. A slight gold coating evaporated over the Am^{241} should eliminate any chemical reaction problem that may be found. It is thus felt that Am^{241} vacuum sublimed sources are quite suitable for use in the thin source configuration.

The Po^{210} rolled foil source has sealed edges to the foil and a 3 micron gold-palladium face. The initial activity was nominally $100\mu\text{ Ci}$, while the measured activity was near $60\mu\text{ Ci}$. Results of stability checks for this source are given in Table 4.6. It can be seen that over a period of six months the standard deviation on the alpha peak was constant at about 0.37 MeV. Activity decreased approximately with the half-life. The inequality of the calculated and measured activities for 10/23/68 is attributed to the difference in effective detection area of the detector used on that date.

The results listed in Table 4.6 show that under laboratory conditions (room temperature and atmospheric pressure) the Po^{210} foil suffers no degradation other than decay of the activity. However, with its low melting point (254°C) and known ability to migrate it is not felt that the Po^{210} foil can withstand the heat cycles of the decontamination procedure (Ref. 4.5). Severe contamination is quite likely to occur if the Po^{210} foil is heated. It is thus felt that Po^{210} is not a suitable source for use in the thin source configuration.

Table 4. 5

Data on the Stability of Am²⁴¹ Vacuum Sublimed Sources

Am²⁴¹ vacuum sublimed on a platinum disc - nominally 100μ Ci

Source Number	Date of test (mo/day/yr)	Measured activity (μ Ci)	Standard deviations, σ	
			Peak(keV)	E ≥ 0. 5 MeV(in MeV)
5021	11/4/68	33	37	
	11/7/68	32	38	
	4/22/69	32	41	0. 44
5022	11/4/68	33	39	
	1/2/69	33	47	
	1/6/69	32	43	0. 43
	4/22/69	32	40	0. 41
5023	11/4/68	33	39	
	1/3/69	32	45	0. 38
	4/22/69	32	41	0. 46
5024	11/4/68	33	40	
	1/3/69	32	44	0. 38
	4/23/69	32	42	0. 41

Table 4. 6

Data on the Stability of a Po²¹⁰ Foil Source

Po²¹⁰ rolled foil source with a 3 micron gold-palladium face

Date of test (mo/day/yr)	Calculated activity (μ Ci) ^{a)}	Measured activity (μ Ci)	Standard deviation of peak, σ (MeV)
10/23/68	64	59	0. 37
11/12/68	(58)	58	0. 39
12/31/68	45	46	0. 36
4/23/69	26	27	0. 37

a) Activity for 11/12/68 is assumed, the others are calculated on the basis of a 138 day half-life. The measurement for 10/23/68 was made with a different detector and the inequality of calculated and measured activities is most likely the result of different effective areas for the detectors.

Cm^{242} foil and evaporated sources are currently being manufactured by The Radiochemical Centre, so if a short half-life alpha source (163 days) is wanted these might be tested in the future. Cm^{242} is not expected to suffer from migration like Po^{210} , but experience with Cm^{242} is quite limited as it has only recently become available commercially.

4.2 Thick Source Method

The thick source method has been investigated using two types of alpha source. Most of the tests were made with three high specific activity Am^{241} foil sources. These sources contain Am^{241} in a silver matrix and have a 3 micron gold-palladium face. The activity is nominally 15 m Ci in a 25 mm diameter active area. The sources are manufactured by The Radiochemical Centre. The other type source used was a Po^{210} microsphere source manufactured by the 3M Company, St. Paul, Minnesota. One 3 m Ci Po^{210} microsphere source was ordered for testing. These sources are manufactured commercially for static eliminators.

Spectra of the three Am^{241} foil sources and of the Po^{210} microsphere source are shown in Figures 4.7 to 4.9. One of the Am^{241} foil sources was manufactured a few months before the other two, and shows a significantly different spectrum. It thus appears that, while source uniformity can be achieved by manufacture in one lot, there is still likely to be variation between lots. This point is discussed more fully in Section 4.2.3.

4.2.1 Experimental Calibration Curves

The results from stopping power measurements and some of the thin source method tests show that CO_2 - N_2 differences become several percent for energy losses by particles below 1 MeV. This is illustrated by the experimental results shown in Figure 4.10 where thick source data with a 0.25 MeV threshold show several percent deviation between the CO_2 and N_2 points. The measurements were made with Am^{241} foil 112572/1 covered one-half with 0.45 mil Al foil and the other half with 0.60 mil Al foil.

The data in Figure 4.11 show that the CO_2 - N_2 differences of Figure 4.10 can be reduced to less than a few percent by covering the detector with 0.45 mil of Al foil. A 0.25 MeV detector threshold then becomes an effective threshold of 3 MeV when referred to energy loss in the gas. Note that the Ar data are plotted both directly and using an effective density

$$\rho_{\text{eff}} = \rho_{\text{Ar}} \times 0.67 \quad (4.6)$$

The results of Figure 4.11 show that a detector threshold of 0.25 MeV can be used without causing increased CO_2 - N_2 differences. For reference, the alpha

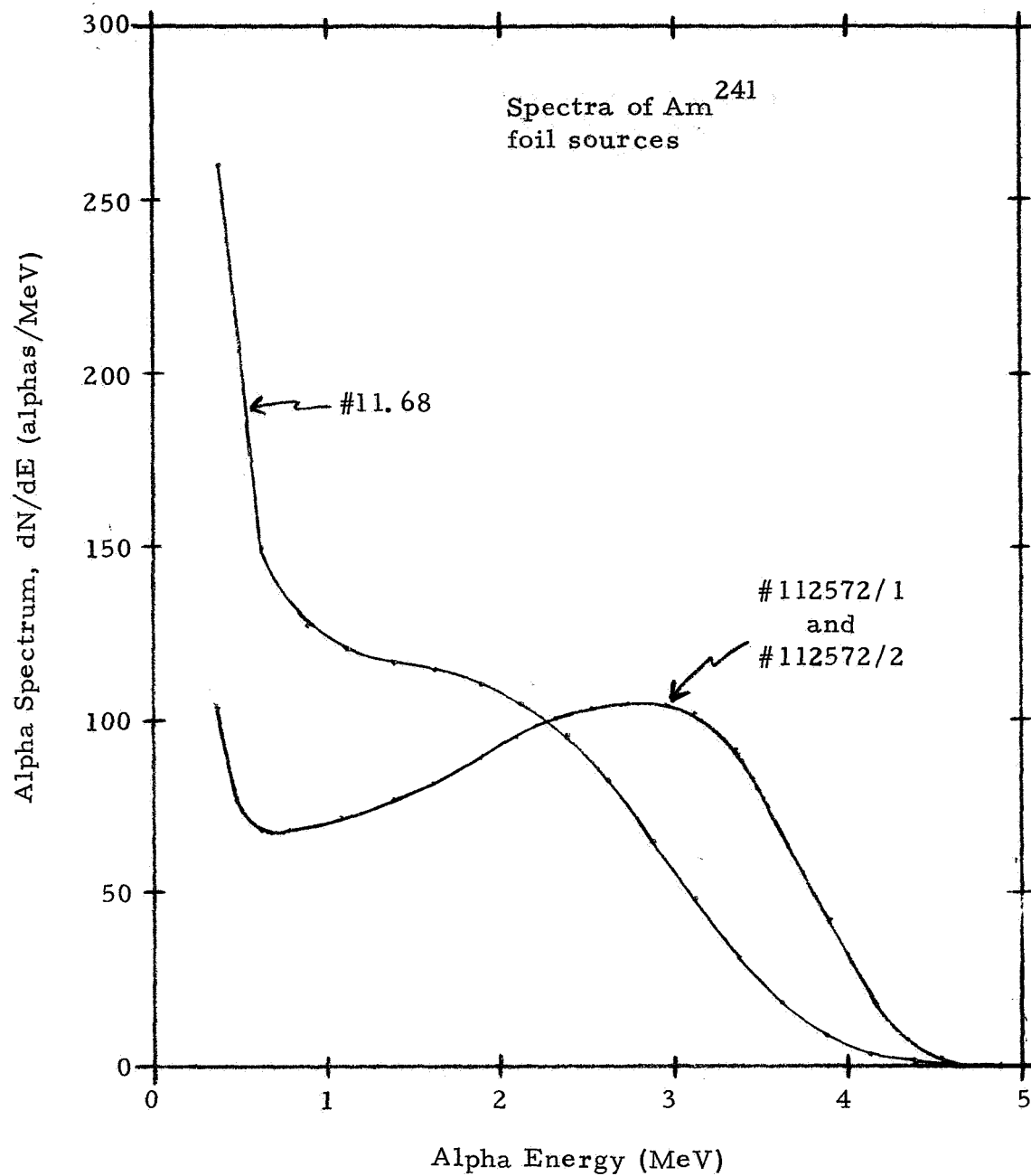


Figure 4.7 Spectra of the Three Am²⁴¹ Foil Sources

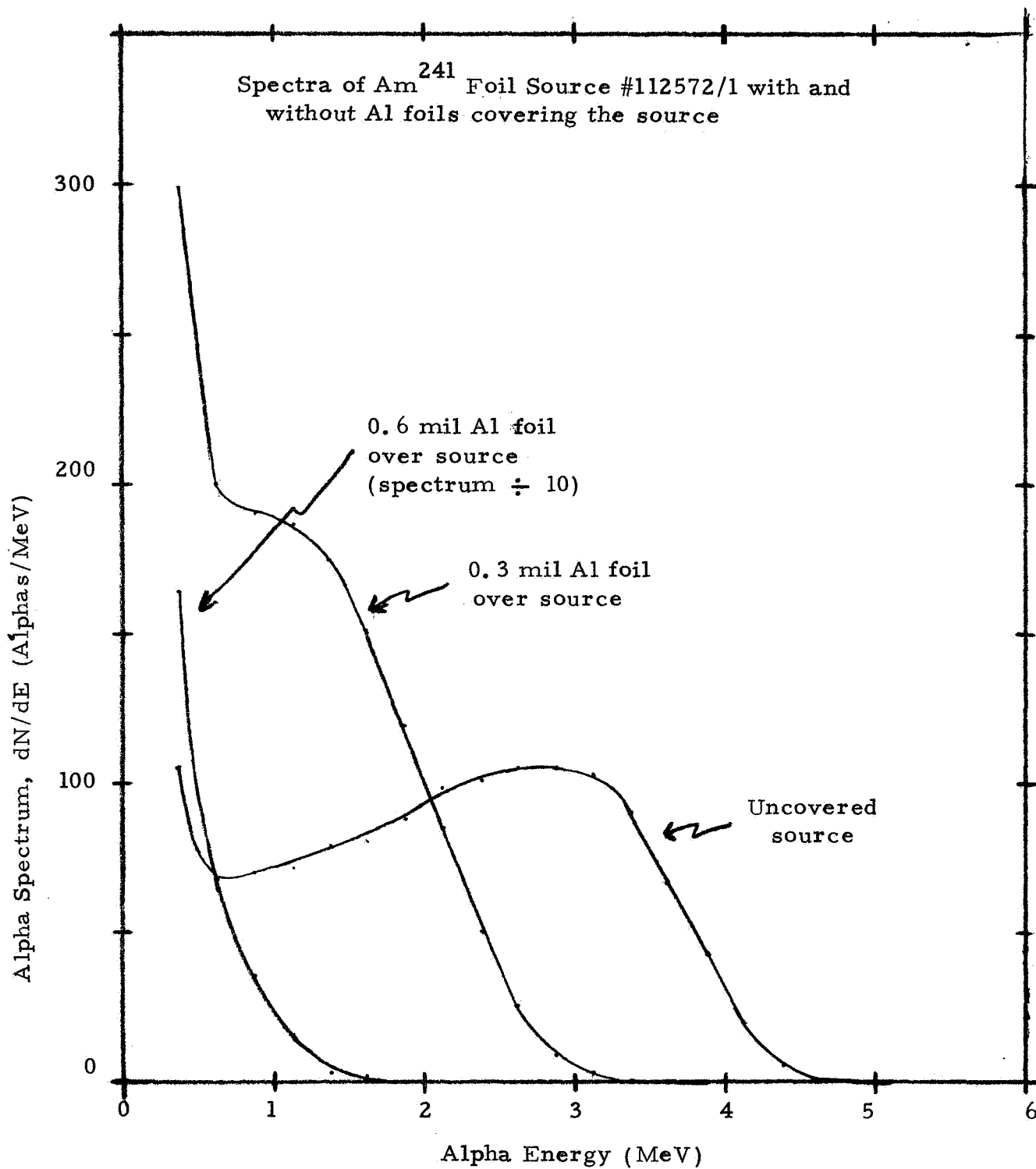


Figure 4. 8a Spectra of an Am^{241} Foil Source with and without Al Foil Coverings.

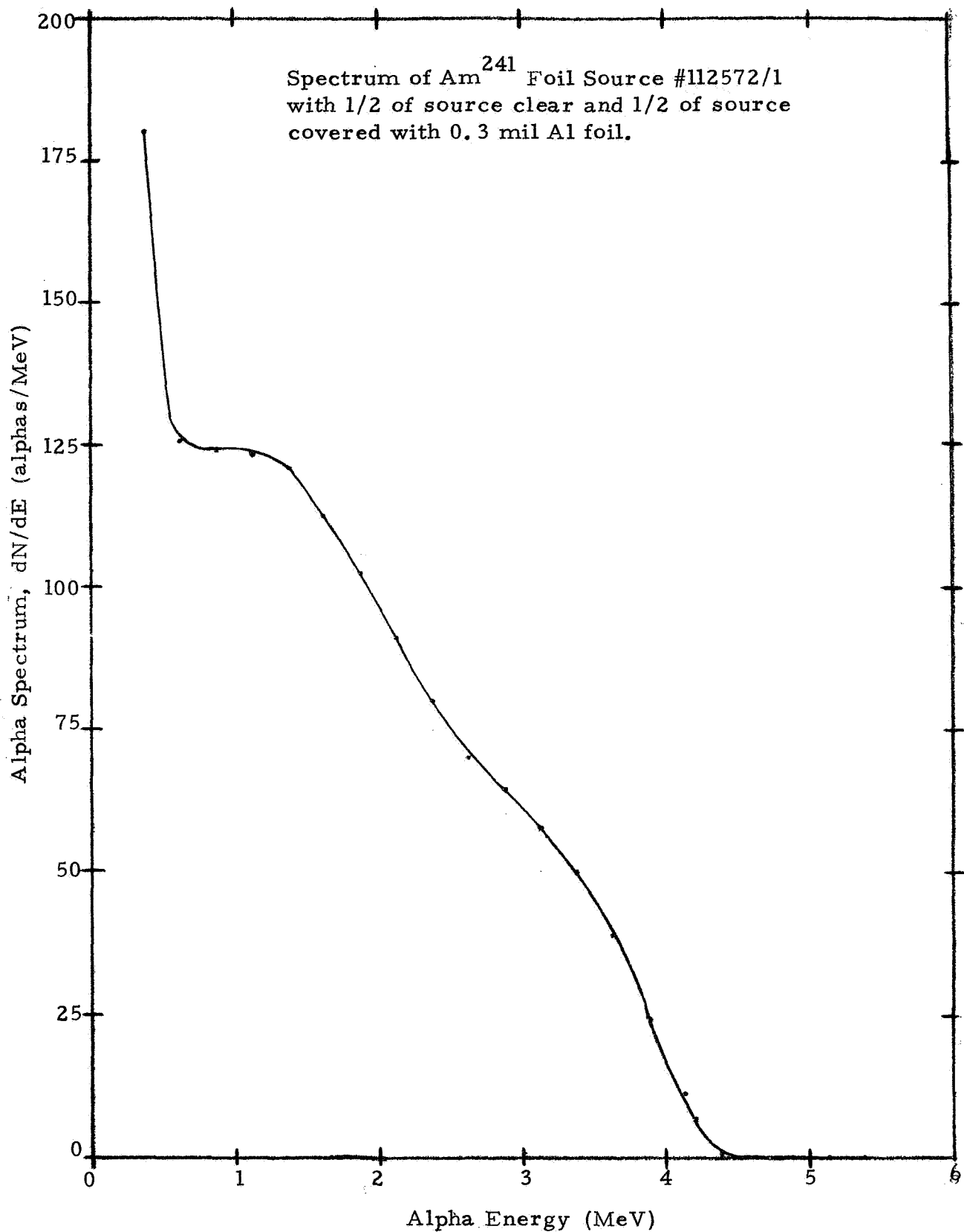


Figure 4. 8b Spectrum of an Am^{241} Foil Source with a Partial Al Foil Covering.

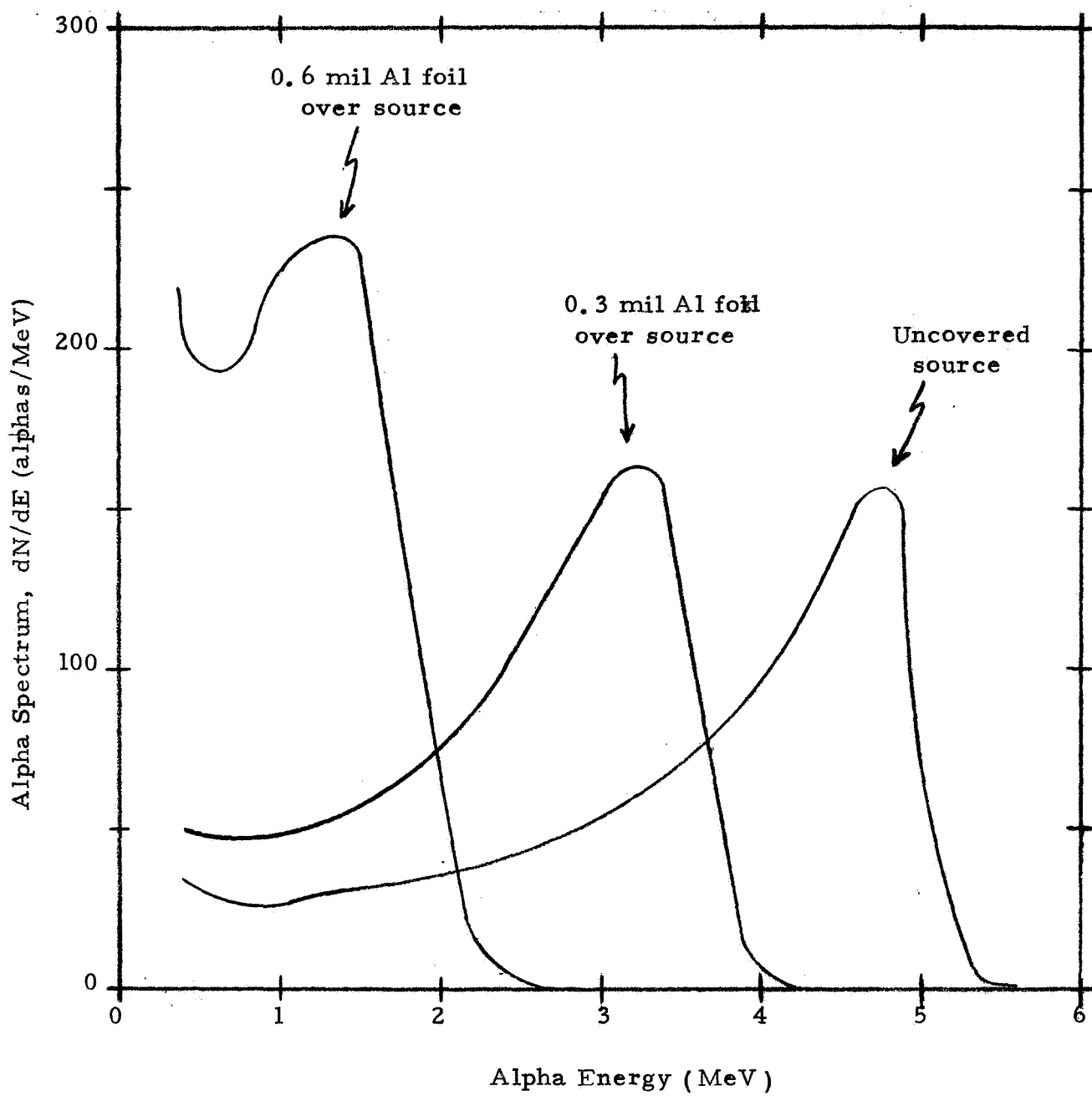


Figure 4.9 Spectra of the Po^{210} Microsphere Source with and without Al Foil Coverings.

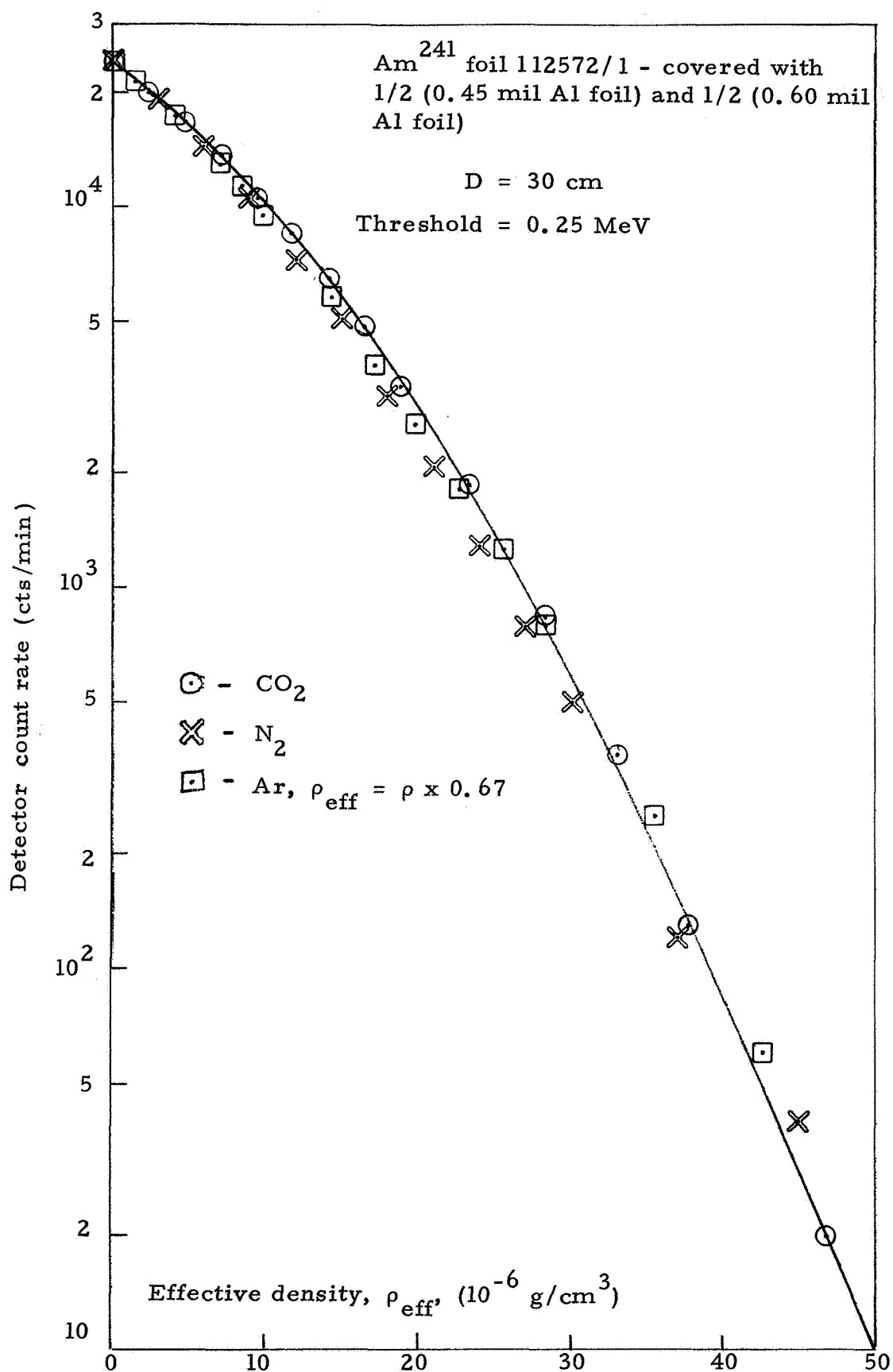


Figure 4. 10. Calibration Points for CO₂, N₂ and Ar Using An Am²⁴¹ Foil Source and a 0.25 MeV Threshold - No Detector Covering Foil.

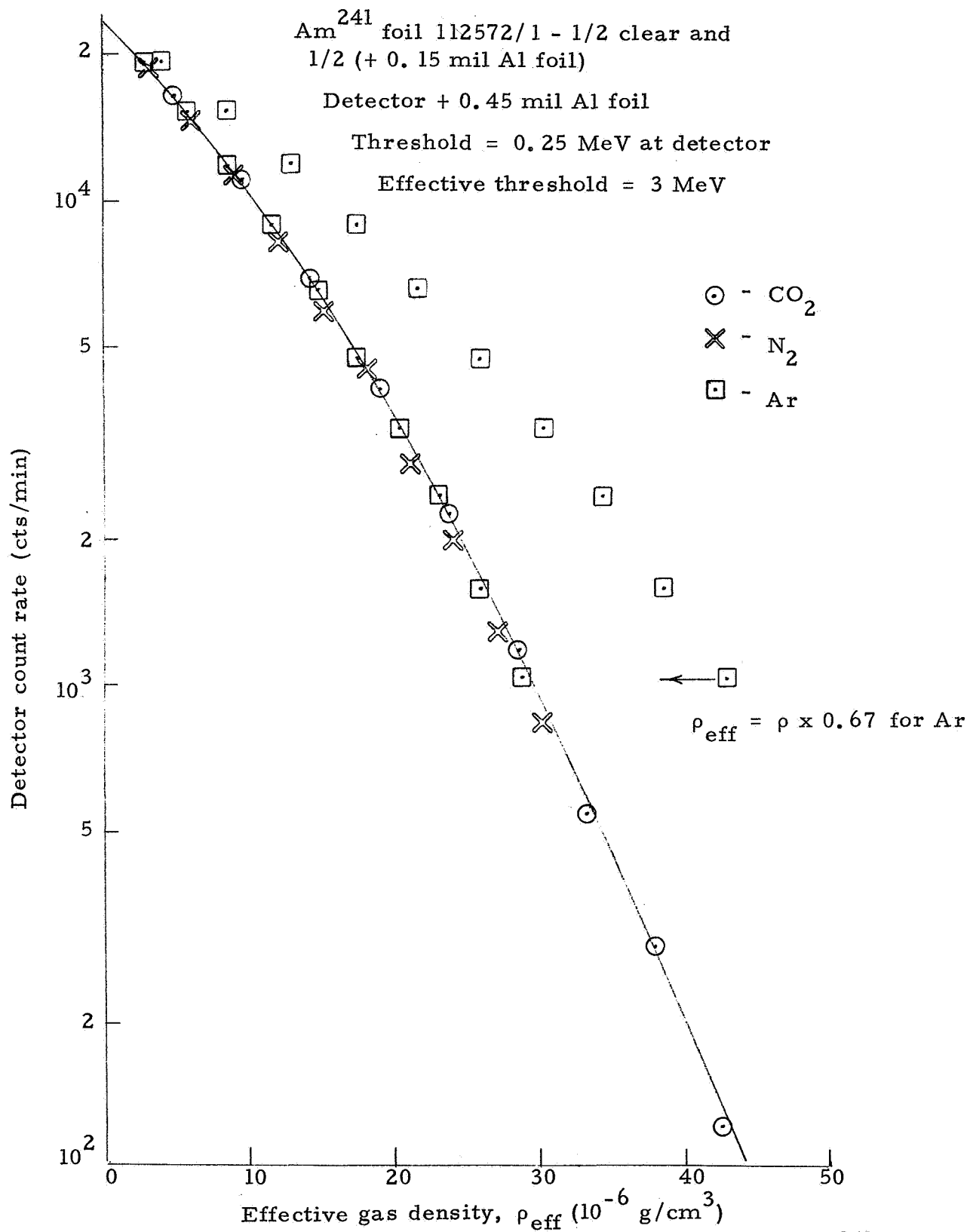


Figure 4. 11. Calibration Points for CO₂, N₂ and Ar Using an Am²⁴¹ Foil Source and a 0.25 MeV Threshold - Detector Covered with 0.45 mil Al Foil.

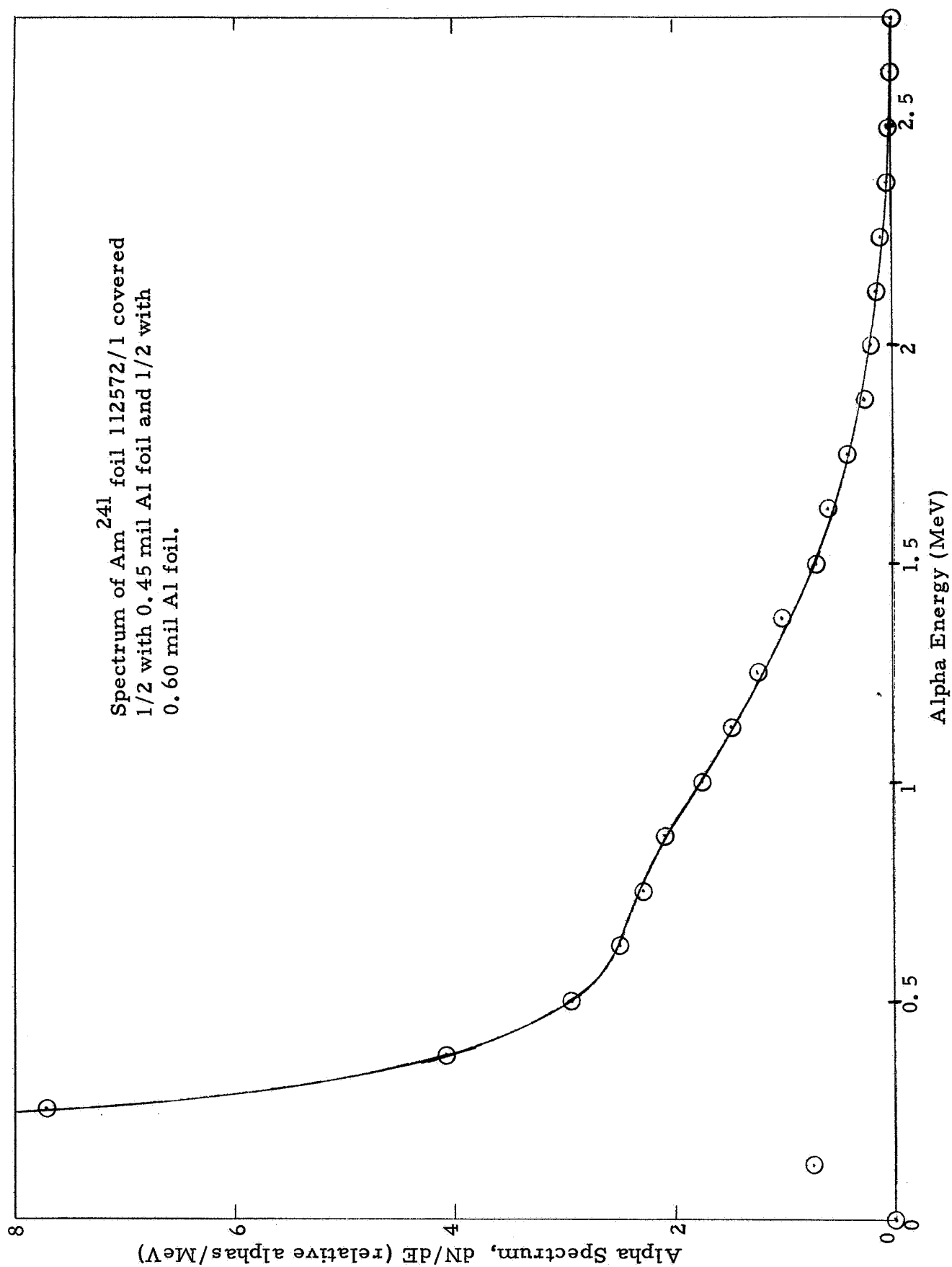


Figure 4.12. Spectrum of Am^{241} Foil Source Covered One-half with 0.45 mil Al Foil and One-half with 0.60 mil Al Foil.

spectrum incident on the detector is plotted in Figure 4. 12.

The importance of using a low detector threshold is verified by the radiation damage data discussed in Section 3. 3, and the statistical error formulation of Section 3. 4. 2. Radiation damage considerations limit the total flux of alpha particles incident on the detector to about 1000/cm²-sec). From Eq. (3. 51) it is seen that the fractional error in the measured count rate is

$$\frac{\delta C}{C} = \frac{1}{\sqrt{CT}} \quad (4. 7)$$

and by assuming

$$\left| \frac{d\rho}{dC} \right| \approx \frac{\rho}{C} \quad (4. 8)$$

(3. 52) then gives

$$\frac{\delta\rho}{\rho} \approx \frac{\delta C}{C} = \frac{1}{\sqrt{CT}} \quad (4. 9)$$

Thus, statistical error minimization argues for using as large a count rate as feasible. Since a high detector threshold effectively wastes that portion of the alpha spectrum lying below the threshold, it can be easily seen that the best overall system response is obtained with the lowest feasible energy threshold. In practice, 0. 25 MeV is a quite suitable threshold as it is far enough above the noise level to avoid counting noise pulses, even for a detector with a large leakage current.

The use of a low detector threshold can be combined with the requirement that energy loss in the gas be for particles above 1 MeV by covering the detector with a foil. This is shown quite clearly by Figures 4. 10 and 4. 11. Figure 4. 13 shows the data for CO₂ and N₂ taken with a 0. 04 mil gold foil over the detector and a 0. 225 MeV threshold. This provides an effective threshold of about 1. 0 MeV. The Am²⁴¹ foil source had several 0. 15 mil Al foils with varying size holes to generate the source spectrum shown in Figure 4. 14.

The Po²¹⁰ microsphere source 30 cm from the detector gives the results shown in Figure 4. 15. The effective density for Ar is taken as 0. 67ρ. The data in Figure 4. 15 show that a spectrum peaked at high energy (see Figure 4. 9 for the source spectrum) has the most rapid change in count rate at high densities.

Calibration data for the Am²⁴¹ foil sources 11. 68 and 112572/1 are given in Figures 4. 16 and 4. 17. Again, the Ar effective density is taken as 0. 67ρ. Spectra of these sources are shown in Figure 4. 7.

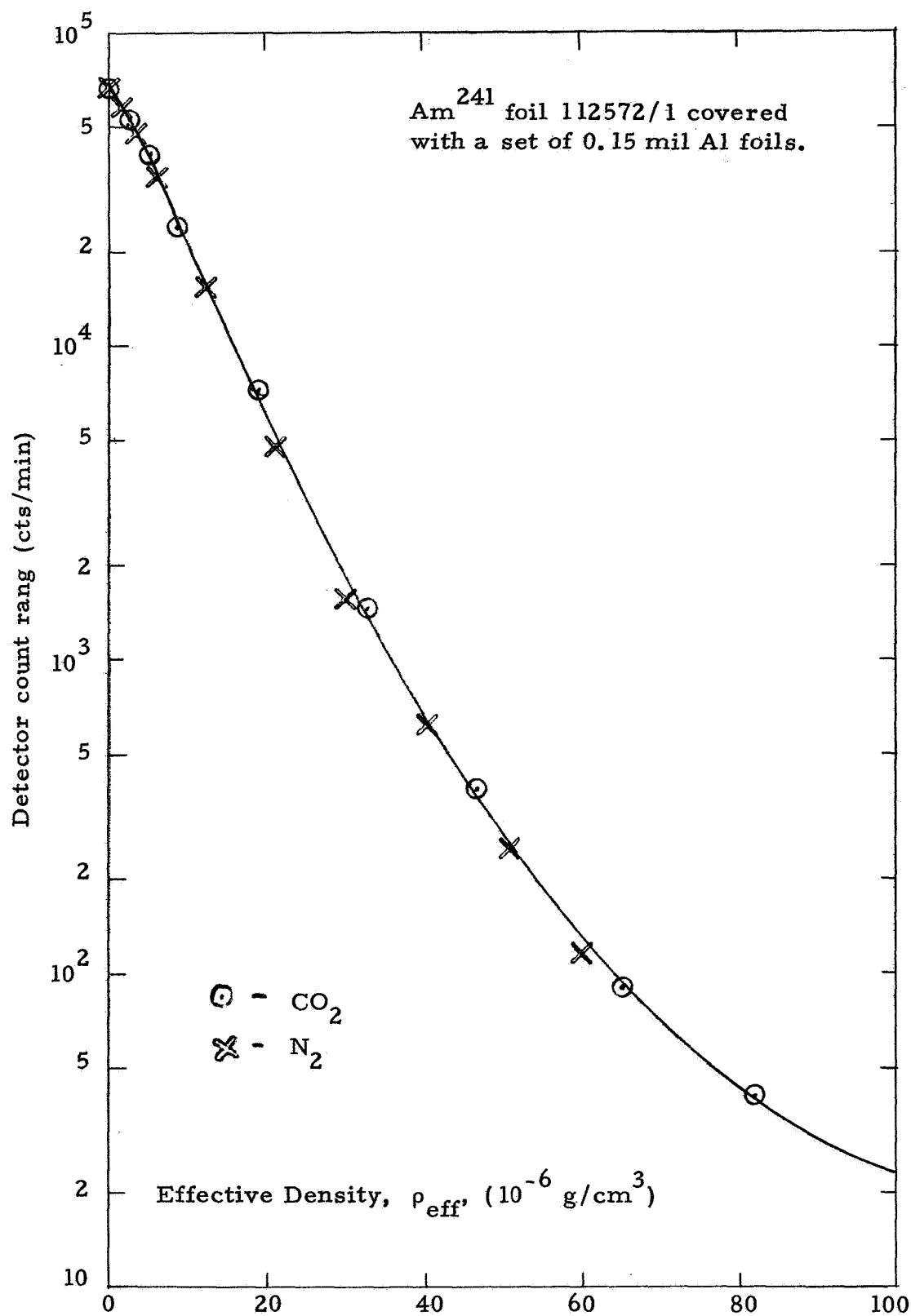


Figure 4.13. Calibration Points for CO₂ and N₂ Using an Am²⁴¹ Foil Source Covered with Al Foils to Generate the Spectrum of Figure 4.14.

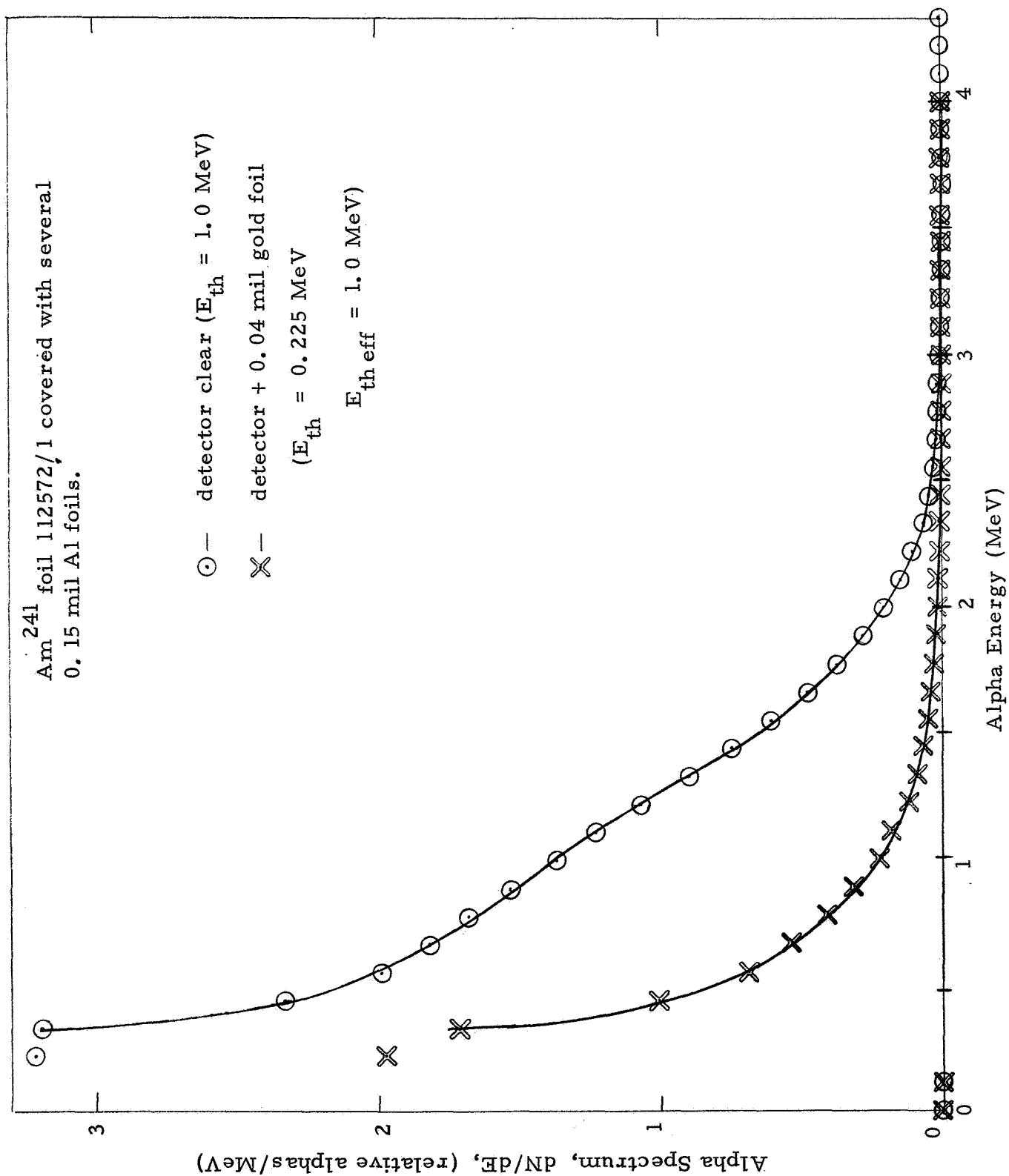
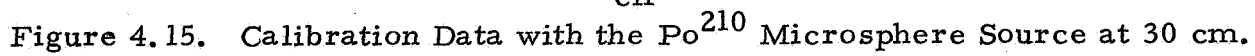


Figure 4.14. Spectrum of Am²⁴¹ Foil Source Covered with Several 0.15 mil Al Foils.



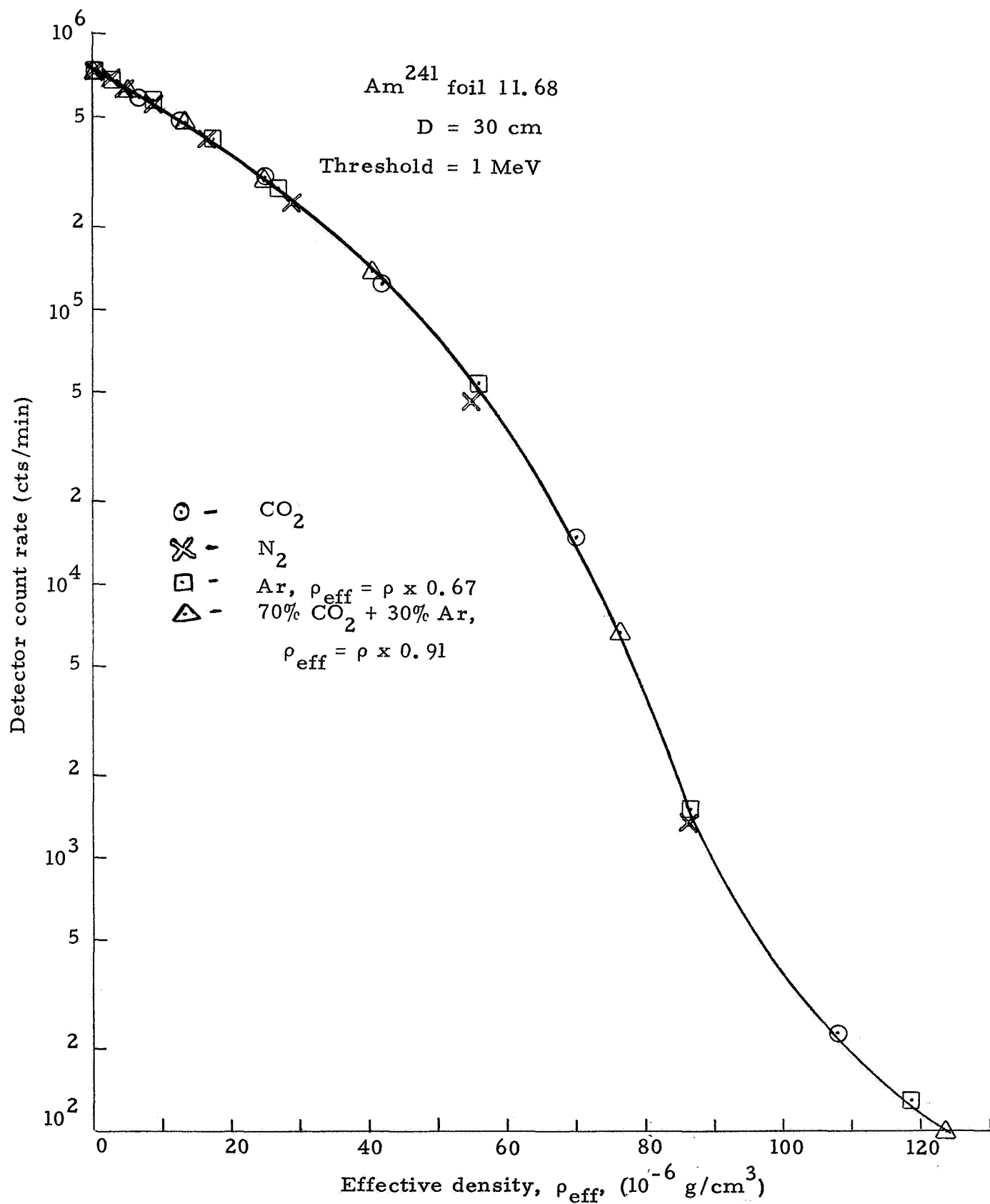


Figure 4.16. Calibration Data with the Am²⁴¹ Foil Source #11.68 at 30 cm.

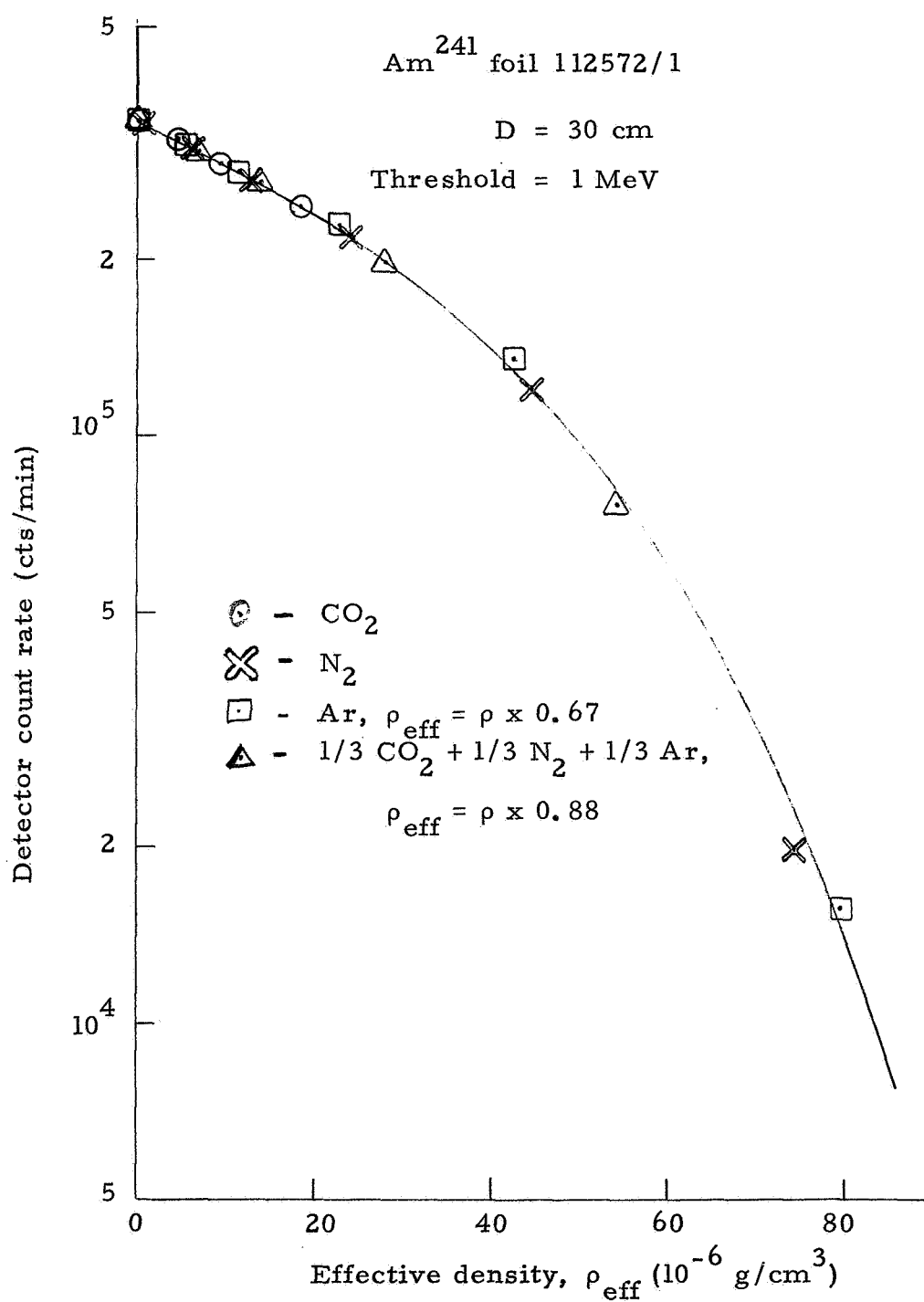


Figure 4.17. Calibration Data with the Am²⁴¹ Foil Source # 112572/1 at 30 cm.

The results shown in Figures 4. 10 to 4. 17 support the following general conclusions. First, it is desirable to have a high effective threshold when referred to energy loss in the gas. Second, a high effective threshold and a low detector threshold can be achieved by covering the detector with a foil. Third, with the use of a high effective threshold the $\text{CO}_2\text{-N}_2$ differences can be reduced to a few percent or less. This also results in an effective Ar density of 0.67ρ . Fourth, alpha spectra peaked near the effective threshold give the largest change in count rate at low densities, while spectra peaked at higher energies give the largest change at high densities.

The general conclusion of this section is that a thick source system can be designed with the response giving an effective density defined by (4. 4) to within a few percent. Determination of the actual gas density then requires knowing the Ar density or mass fraction. If system accuracy greater than a few percent is desired then composition information is required and the methods outlined in Section 3. 1. 2 must be used to convert the CO_2 calibration curve to that for the (known) gas mixture.

4. 2. 2 Expected Errors for the Thick Source Method

The errors for the thick source method are calculated by use of Equations (3. 51) to (3. 55), with $\left| \frac{d\rho}{dC} \right|$ being obtained from the calibration curve for the system under consideration. We note that the statistical and telemetry errors depend on the shape of the calibration curve (Eq. (3. 52)) while the electronic drift error depends only on the source-detector separation and stopping powers of the gas and detector foil at fixed energies (Eq. (3. 53)).

Since a digital system output reduces the telemetry errors to zero we consider the statistical errors first. Figure 4. 18 shows the calibration curves for five thick source systems as well as the constant error system (Eq. 3. 20) and the constant fractional error system (Eq. 3. 22). The curves labeled 3 to 7 are derived from the experimental curves shown earlier, but have been adjusted to yield a maximum density measurement of $80 \times 10^{-6} \text{ g/cm}^3$ and to give a maximum count rate of 4000/sec. Table 4. 7 gives the necessary data to understand the curves shown in Figure 4. 18.

From the curves in Figure 4. 18 the statistical errors can be easily derived, and these are plotted in Figure 4. 19 for a 4000 count maximum. The two dotted curves show the constant error response (Eq. (3. 20)) and the constant fractional error response (Eq. (3. 22)) with $\Delta\rho_{st} = 0.04\rho$. The following conclusions can now be made. First, strongly peaked spectra (Figure 4. 13 for low energy, Figure 4. 15 for high energy) produce a corresponding minimum in the measurement error. Second, approximately constant-error systems can be made (curve 7) and the resulting errors agree quite closely with the theoretical system (curve 1). Finally, a constant fractional error system can be approximately generated (curves 3, 4 and 6 compared to curve 2), but the error

Table 4. 7
Data on the Thick Source Systems Described in
Figures 4. 18, 4. 19 and 4. 20

Curve Number	Source for Calibration Curve	Adjusted Source - Detector Distance (cm)		Effective Threshold (MeV)	Alpha Source Used
		No TM error Figs. 4. 18 and 4. 19	With TM error Fig. 4. 20		
1	Eq. (3. 20)	-	-	-	
2	Eq. (3. 22)	-	-	-	
3	Fig. 4. 11	20	11	3	Am ²⁴¹ foil 112572/1 with Al foils
4	Fig. 4. 13	20	11	1	Am ²⁴¹ foil 112572/1 with Al foils
5	Fig. 4. 15	48	48	1	Po ²¹⁰ micro- sphere source
6	Fig. 4. 16	35	22	1	Am ²⁴¹ foil 11. 68
7	Fig. 4. 17	40	30	1	Am ²⁴¹ foil 112572/1

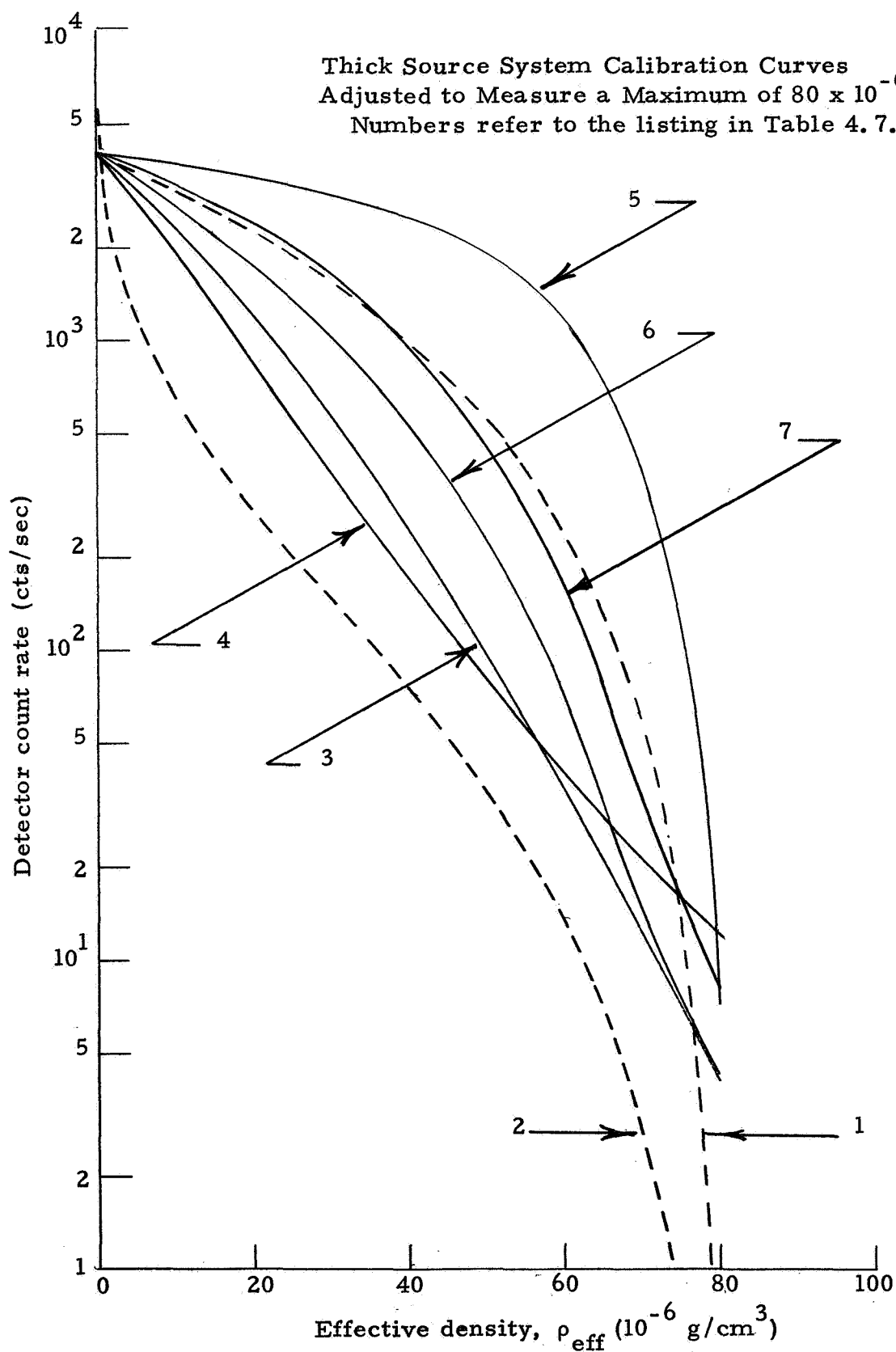


Figure 4.18. Plots of Several Thick Source System Calibration Curves.

Thick Source Design
Maximum Performance System
Density Errors

Numbers refer to listing in Table 4.7

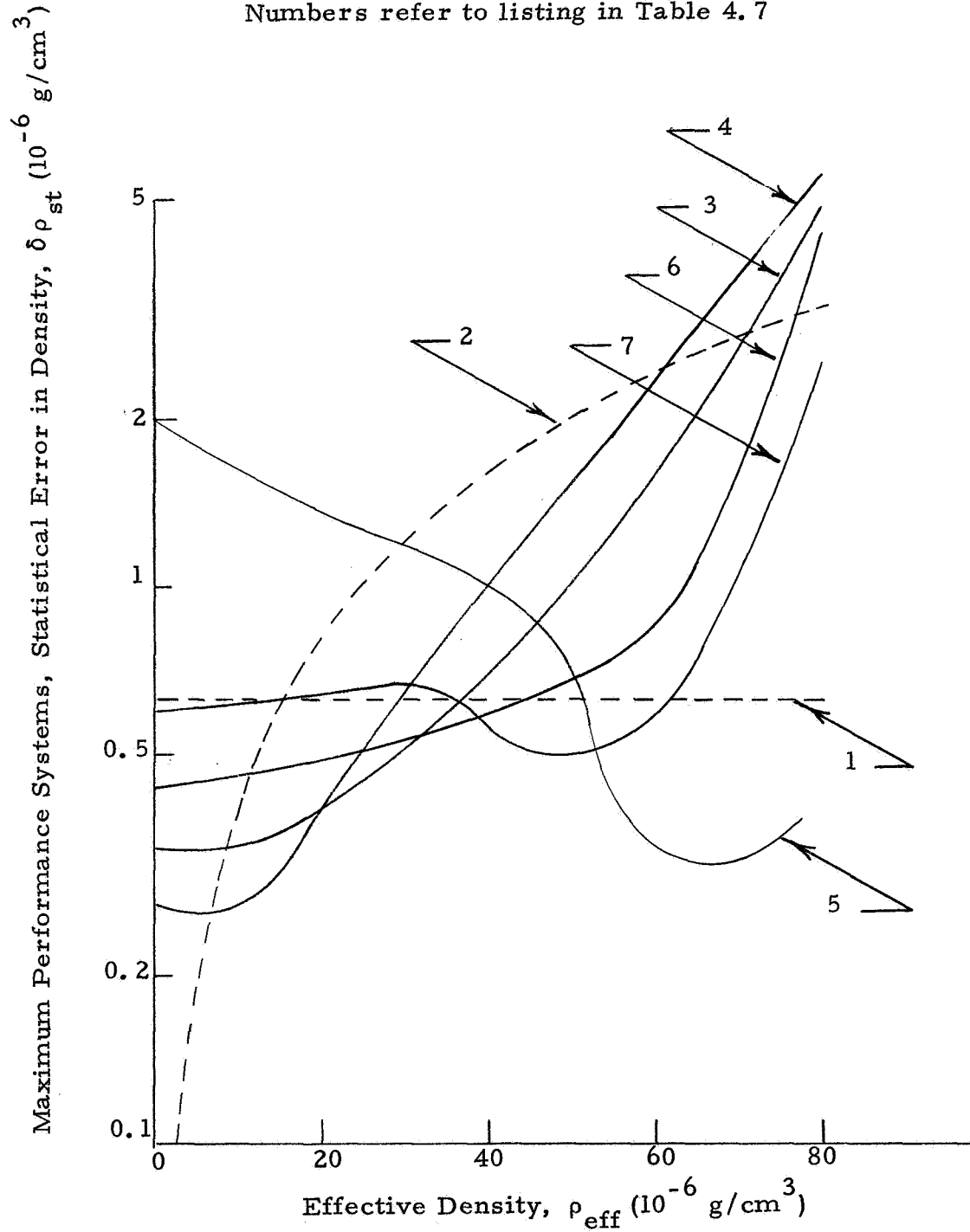


Figure 4.19. Statistical Error in Density for Several Thick Source Systems - Maximum Performance Designs.

at low densities tends to flatten at a few $\times 10^{-7}$ g/cm³.

The constant fractional error curve 2 is for a 4% statistical error. If only Ar composition information is obtained, then composition effects can lead to errors of a few percent and statistical errors lying appreciably below curve 2 will be masked by these composition errors. The constant fractional error systems are thus preferable for the general case where composition information is limited.

It is not likely that the error at low densities can be reduced below 1×10^{-7} g/cm³ when a 4000 cps limit is imposed on the system (4 cm² detector, 1000 a' s/(sec-cm²), 1 second counting time). Such low errors require an alpha spectrum very strongly peaked at a low energy threshold (as seen by the detector). The spreading of a monoenergetic alpha peak with increasing energy loss (see Figure 3.2) make it impossible to generate a low energy (≈ 0.5 MeV) peak with a full-width-at-half-maximum of less than 0.5 MeV. Such a spectrum, filled in to 5.5 MeV and used at a separation of 55 cm, would still yield a minimum statistical error of about 1×10^{-7} g/cm³. Use of a narrow, but high energy, alpha peak with a threshold set near the peak energy can reduce the statistical error at low densities, but leads to electronic drift errors considerably larger than 1×10^{-7} g/cm³.

The electronic drift errors are considered next. From Eq. (3.53)

$$\delta \rho_{\text{drift}} \approx \frac{1.0 \times 10^{-3}}{D} \delta E_{\text{th}} \quad (4.10)$$

where use has been made of

$$\frac{1}{S(E'_{\text{th}})} \frac{S_f(E'_{\text{th}})}{S_f(E_{\text{th}})} \approx \frac{1.0 \times 10^{-3} \text{ g/cm}^2}{\text{MeV}} \quad (4.11)$$

Equation (4.11) holds to about 30% for values of E_{th} near 0.25 MeV. Using $\delta E_{\text{th}} = 0.005 E_{\text{th}}$ and $E_{\text{th}} = 0.25$ MeV yields the values for $\delta \rho_{\text{drift}}$ listed in Table 4.8. The last column lists the drift errors for a 2 MeV threshold and is given to substantiate the remark made earlier that use of a narrow high energy alpha peak to reduce statistical errors at low densities will result in increased drift errors. Since the drift errors in Table 4.8 are considerably less than the statistical errors in Figure 4.19, the errors shown in Figure 4.19 are those for the maximum performance system (see Section 4.3.3).

Telemetry errors arise only for the case where the system output is an analog signal. Under such conditions the telemetry system will introduce

Table 4.8

Electronic Drift Errors for the Thick Source System

Source-Detector Separation (cm)	0.5% drift errors	
	$E_{th} = 0.25 \text{ MeV}$ $\delta\rho_{\text{drift}} (10^{-6} \text{ g/cm}^3)$	$E_{th} = 2.0 \text{ MeV}$ $\delta\rho_{\text{drift}} (10^{-6} \text{ g/cm}^3)$
10	0.13	1.0
20	0.06	0.50
30	0.04	0.33
40	0.03	0.25
50	0.03	0.20
55	0.02	0.18

Table 4.9

Comparison of the Various Density Measuring Systems

System	Power required (mw) ¹⁾	Weight (lbs)	Volume (in ³)	Approximate density errors	
				At $\rho =$	
				At $\rho = 0$ $\delta\rho$ (10 ⁻⁶ g/cm ³)	80 x 10 ⁻⁶ g/cm ³ $\delta\rho$ (10 ⁻⁶ g/cm ³)
<u>Thin source</u>					
Minimum	100	0.5	10	3 ²⁾	1.1 ²⁾
Intermediate	150	0.5	10	1.6-2 ²⁾	0.6-1 ²⁾
Maximum	225	0.7	13	0.7-0.8 ³⁾	0.1-0.2 ³⁾
<u>Thick Source</u>					
Minimum	125	0.5	10	0.6-0.8 ²⁾	4-8 ²⁾
Maximum	165	0.7	13	0.3-0.5 ³⁾	3-5 ³⁾
3% error =				0	2.4

1) To circuits - if a converter is used multiply by 2 (rough).

2) Includes 0.5% electronic drift, statistical, and 1% telemetry errors.

3) Includes 0.5% electronic drift and statistical errors.

an additional error which is assumed to be 1% of the full scale reading. For a 4000 count maximum this is an uncertainty of 40 counts. Using this value for δC_{TM} in Eq. (3.52) and the calibration curves in Figure 4.18 then give telemetry errors which are unreasonably large for densities greater than about $50 \times 10^{-6} \text{ g/cm}^3$. To reduce the telemetry errors at large densities requires that the source-detector distance be decreased. Approximate optimum values are listed in Table 4.7. Using the smaller source-detector distances then gives the total system errors plotted in Figure 4.20. These errors are the statistical and telemetry errors added on an rms basis. The errors at minimum density now become $6 \times 10^{-7} \text{ g/cm}^3$ or greater. Best overall system performance is with curve 3, yielding a minimum density error of about $7 \times 10^{-7} \text{ g/cm}^3$. Note that curves 1 and 2 have not been adjusted as have the experimental curves.

4.2.3 Alpha Source Manufacture, Reproducibility, and Stability

Data have been obtained on three Am^{241} foil sources and one Po^{210} microsphere source. The Am^{241} foil sources were manufactured by The Radiochemical Centre, and the Po^{210} microsphere source by the 3M Company, St. Paul, Minnesota. The latter source is normally manufactured for static eliminators. The spectra of the three Am^{241} foil sources are shown in Figure 4.7. The measured activities of these sources are

#11.68	-	5.0 m Ci
#112572/1	-	11.7 m Ci
#112572/2	-	11.7 m Ci

The first foil was obtained in November 1968, and has shown no noticeable degradation in source spectrum shape or activity over a several month period. The other two foils were received in January 1969, and have shown no degradation over a four month period. Foils 112572/1 and 112572/2 show nearly identical spectra and activities, but differ from foil 11.68. It can thus be concluded that Am^{241} foil source manufacture is reproducible in one lot, but may show variations between lots.

The foil sources are not expected to suffer from the heat cycles of the decontamination procedure. Since they have a 3 micron gold-palladium overlay there should also be no difficulty with the decontamination atmosphere, though this must be checked experimentally (Ref. 4.5).

The Po^{210} microsphere source should be quite reproducible, since it is in commercial production for static eliminators. Tests with one source of about 1.3 m Ci activity show no noticeable degradation over a four month period other than the 138 day decay of the Po^{210} . However, the manufacturer states that heating of the source above 200°F (93°C) will result in severe contamination, so the microsphere source will not survive the decontamination procedure. The manufacturer (3M Company) is currently working on a new method of bonding nickel plated microspheres to a metal surface, but even this

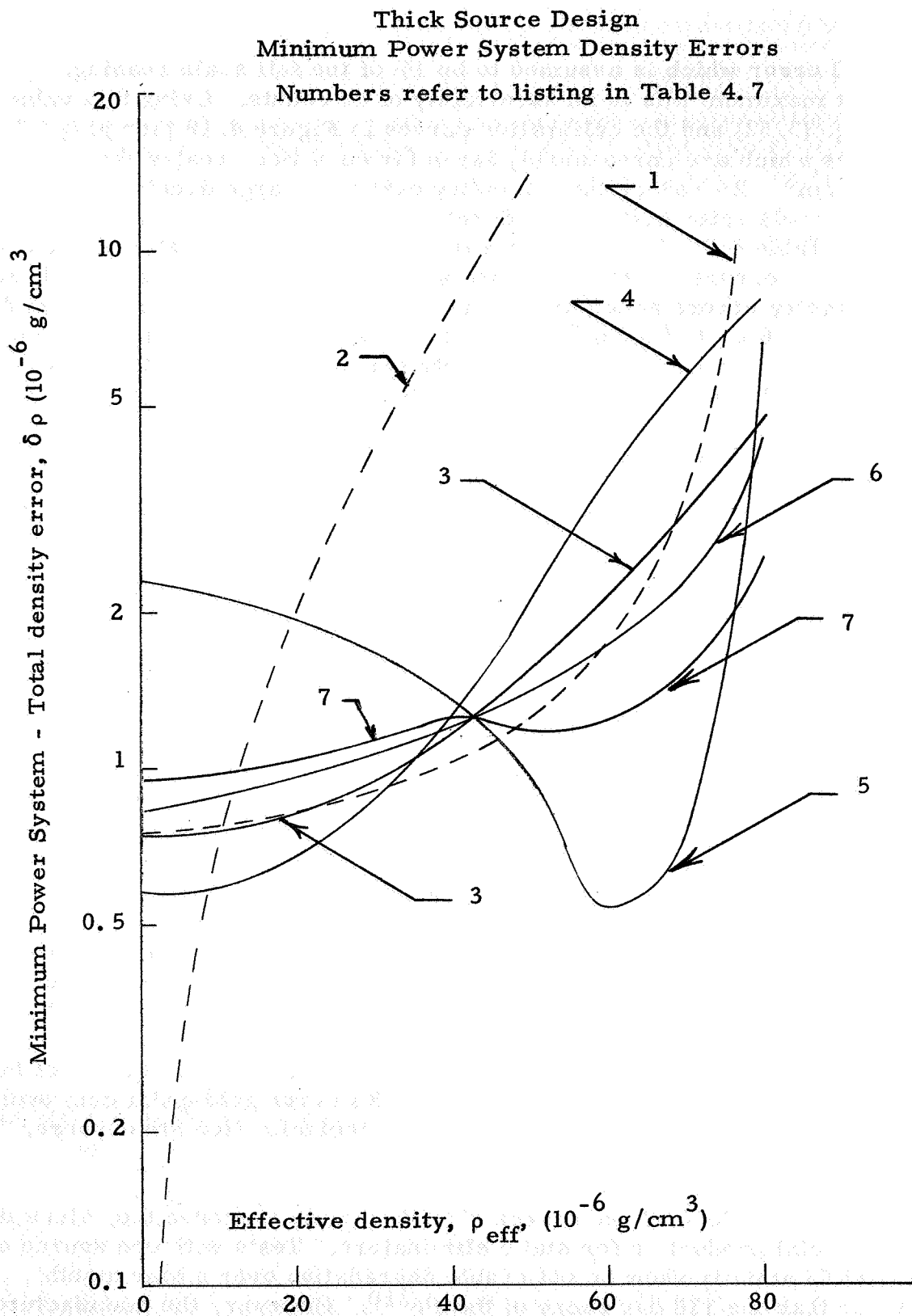


Figure 4.20. Total Density Errors for Several Thick Source Systems Including a One Percent Telemetry Error - Minimum Power Designs.

arrangement might result in a slight amount of Po^{210} migration under heating (Ref. 4.6). It is thus concluded that the Po^{210} microsphere source is unsuitable for use in the thick source system.

Cm^{242} foil sources are now available from The Radiochemical Centre, so if a short half-life alpha source is desired it may be possible to test these sources in the future. They are expected to be as stable as the Am^{241} foil sources.

The preceding discussion shows that Am^{241} foil sources are currently the most suitable for the thick source configuration. Source stability is excellent, but source reproducibility is still only fair. Sources ordered at one time are likely to have identical spectra, but may differ from sources ordered at a different time. Adjustment of the source spectrum can be accomplished by evaporating additional gold onto the gold-palladium face. To produce broad alpha spectra the specific activity should be 3 m Ci/cm² or greater. Total source activity should be about ten times that required on the basis of detector radiation damage since foil adjustment of the spectrum makes use of only about one-tenth of the unadjusted spectrum.

4.3 Proposed System Designs

4.3.1 General Discussion

The density measuring system designs are based on two approaches. The minimum weight and power system is ideal for spacecraft, but with its analog output it is subject to telemetry errors (assumed to be 1% of full scale). The other approach yields a digital output which eliminates telemetry errors, but requires more weight and power.

The basic system construction is shown in Figures 4.21 to 4.23. The source and detector housings can be located anywhere on the lander structure. Experimental tests show that objects near, but not obstructing, the source-detector path do not affect the system calibration curve. However, if the lander structure is at a temperature different from the gas then the gas temperature can be affected by the lander structure and thus the true ambient gas density changed. The latter effect is calculated approximately in Appendix B where it is shown that a wind velocity of several ft/sec should minimize any effects of a difference in gas and lander temperatures. It is recommended, though, that the source-detector path be as far as possible from parts of the lander structure.

4.3.2 Thin Source Method

The thin source method results in three system designs. The minimum power and weight electronics design is shown in Figure 4.24 along with estimated power requirements. Unfortunately, the output of this system is

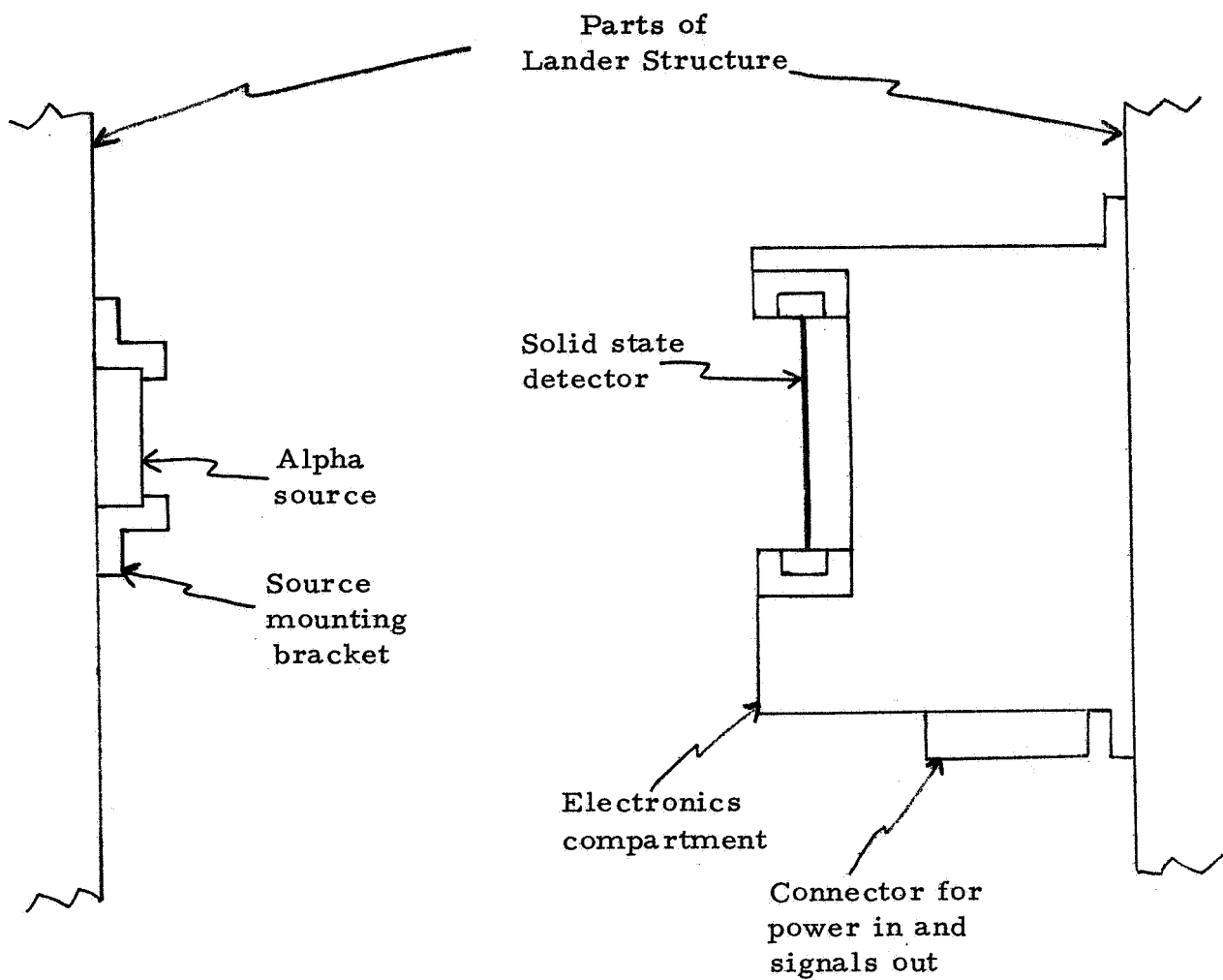


Figure 4.21 Physical Layout of an Alpha Particle Density Measuring System, as Mounted on Portions of the Lander Structure - Full Scale

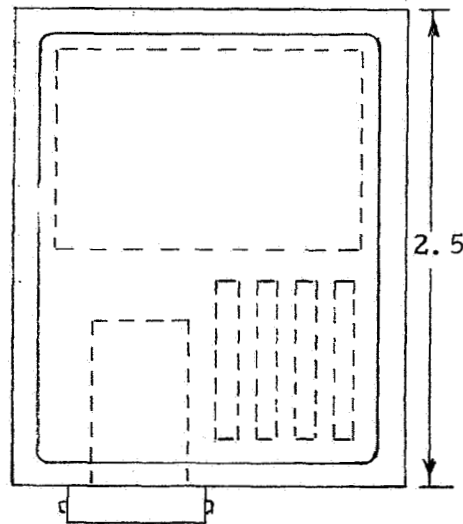
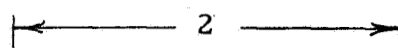
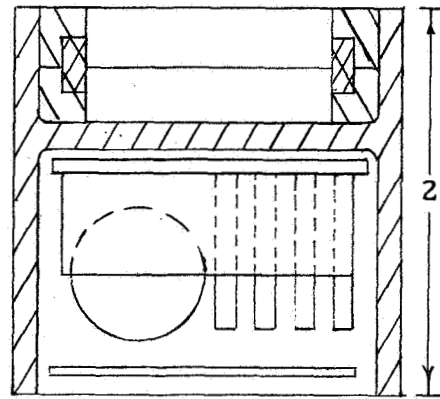


Figure 4.22. Design of the Electronics and Detector Housing for the Minimum Power Configuration. Dimensions are in inches.

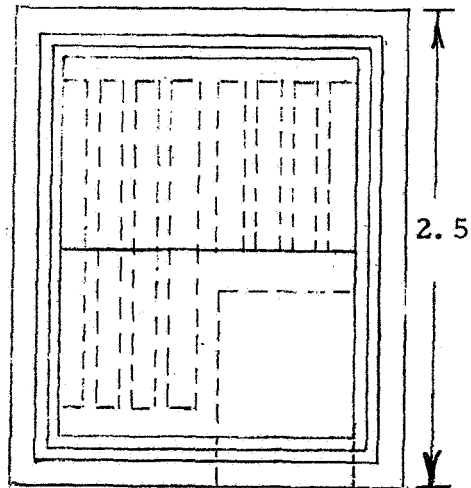
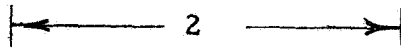
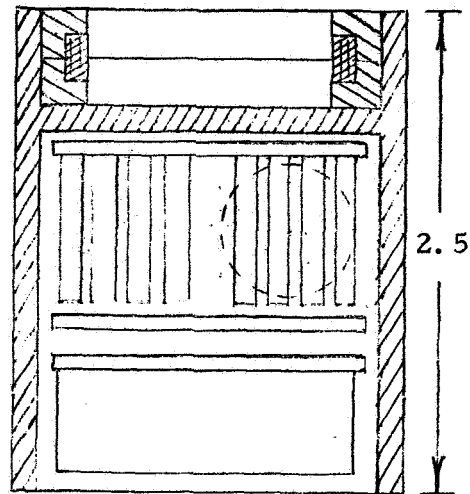
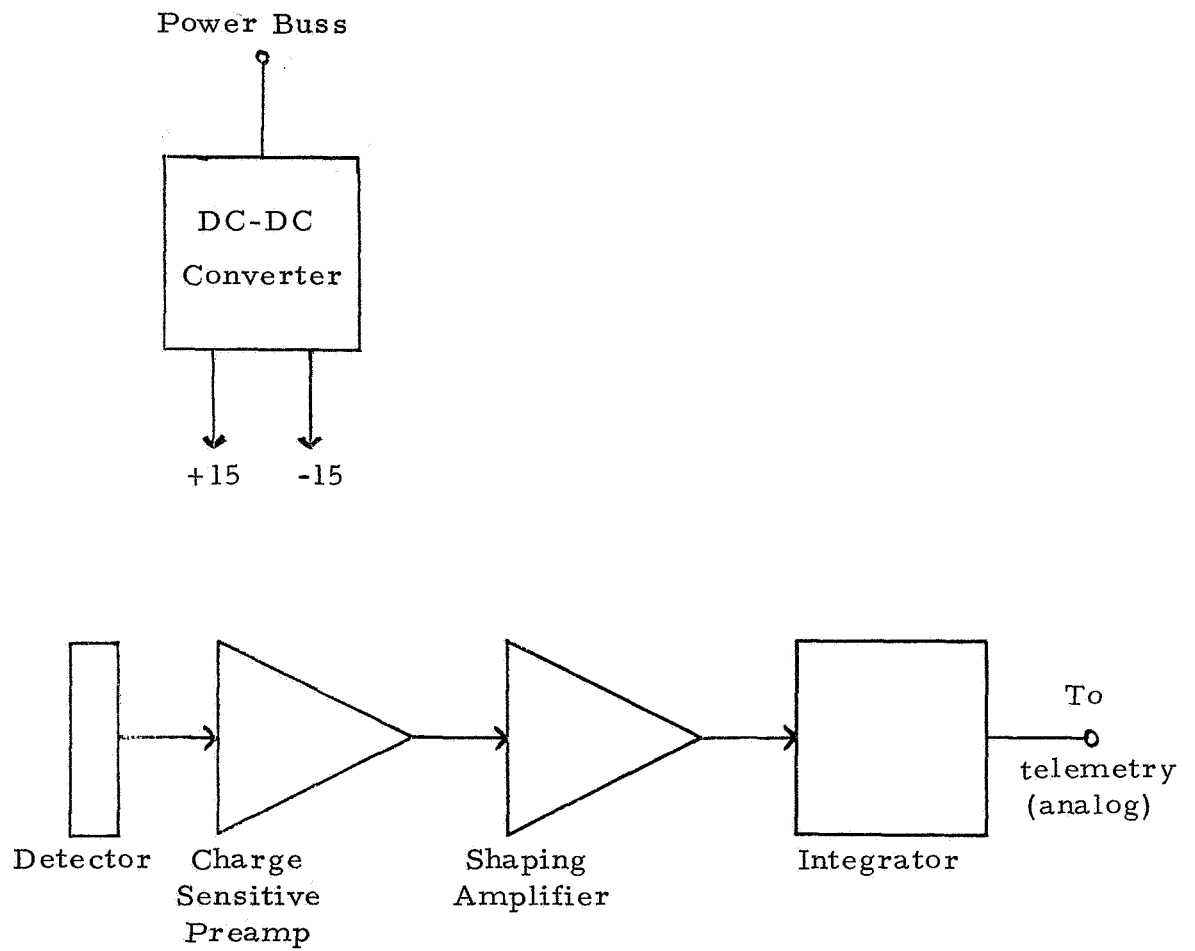


Figure 4.23. Design of the Electronics and Detector Housing for the Maximum Performance Configuration. Dimensions are in inches.



Power Required

To circuits - 100 mw

To converter - 200 mw

Figure 4.24. Electronics Design for Minimum Weight and Power Consumption - Thin Source System.

more strongly count-rate dependent so that an additional 1.6% error is added onto the 1% TM error. This results in errors of $3 \times 10^{-6} \text{ g/cm}^3$ at low density and $1.1 \times 10^{-6} \text{ g/cm}^3$ at high density for the high energy alpha source systems. To overcome the count-rate dependence the circuit of Figure 4.25 can be used. This increases the power consumption somewhat, but reduces the low and high density errors to 1.6×10^{-6} and $0.6 \times 10^{-6} \text{ g/cm}^3$, respectively. Both systems should weigh about 0.5 lb and use a volume of 10 in^3 .

The electronics design for the maximum performance system is shown in Figure 4.26. This system provides an 8 bit digital signal to telemetry as well as a method of calibrating the system by use of a weak full energy source over the detector. The primary source would have to be less than the calibration source by about 1 MeV in energy to allow the calibration mode to work properly. The up-down counter uses 7 binary bits for prescaling and the top 8 bits for feedback to a variable discriminator. This system seeks the median position of the spectrum which in the present case is near the alpha peak. Analysis of the up-down counter operation using computer simulation shows that the standard deviation on the output is given approximately by

$$\sigma_m \approx \sqrt{\frac{0.6 \sigma_p E_o}{N}} \quad (4.12)$$

where σ_p is the standard deviation on the energy of one alpha particle, E_o is the maximum alpha energy, and N is the total number of counter steps required to raise the variable threshold from 0 to E_o MeV. If we wish to average over 4000 counts then we must have

$$\sigma_m \approx \sigma_p / \sqrt{4000} \quad (4.13)$$

Using (4.12) and (4.13) then gives

$$N \approx 2400 E_o / \sigma_p \quad (4.14)$$

Table 3.1 gives $E_o / \sigma_p \approx 15$ for most values of E_o , so

$$N \approx 36,000 = 2^{15.1} \quad (4.15)$$

Thus 15 binary counters will yield an average over approximately 4000 input counts. The only requirement on the feedback to the variable discriminator

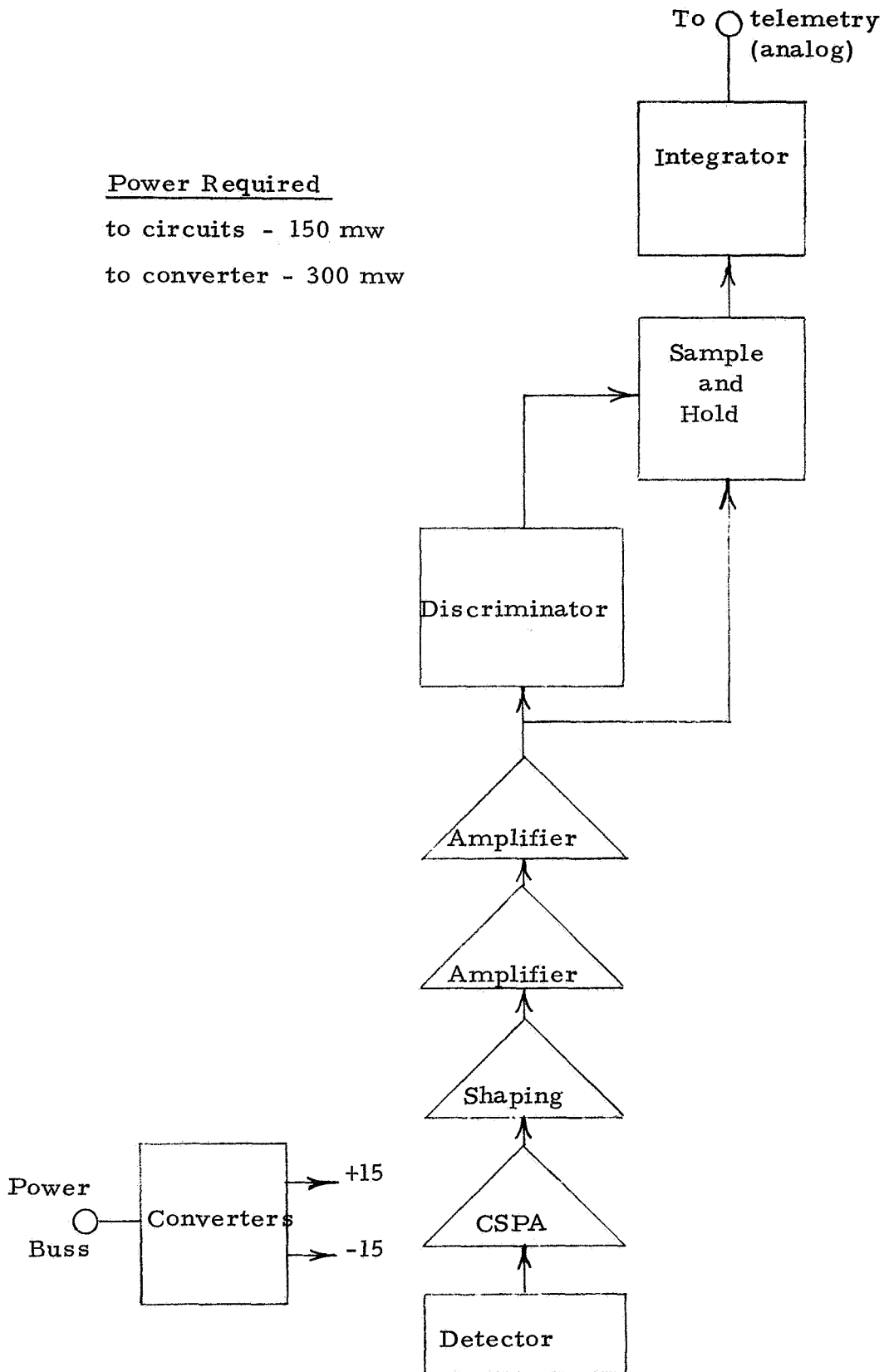


Figure 4.25. Electronics Design for Intermediate Power Consumption - Thin Source System.

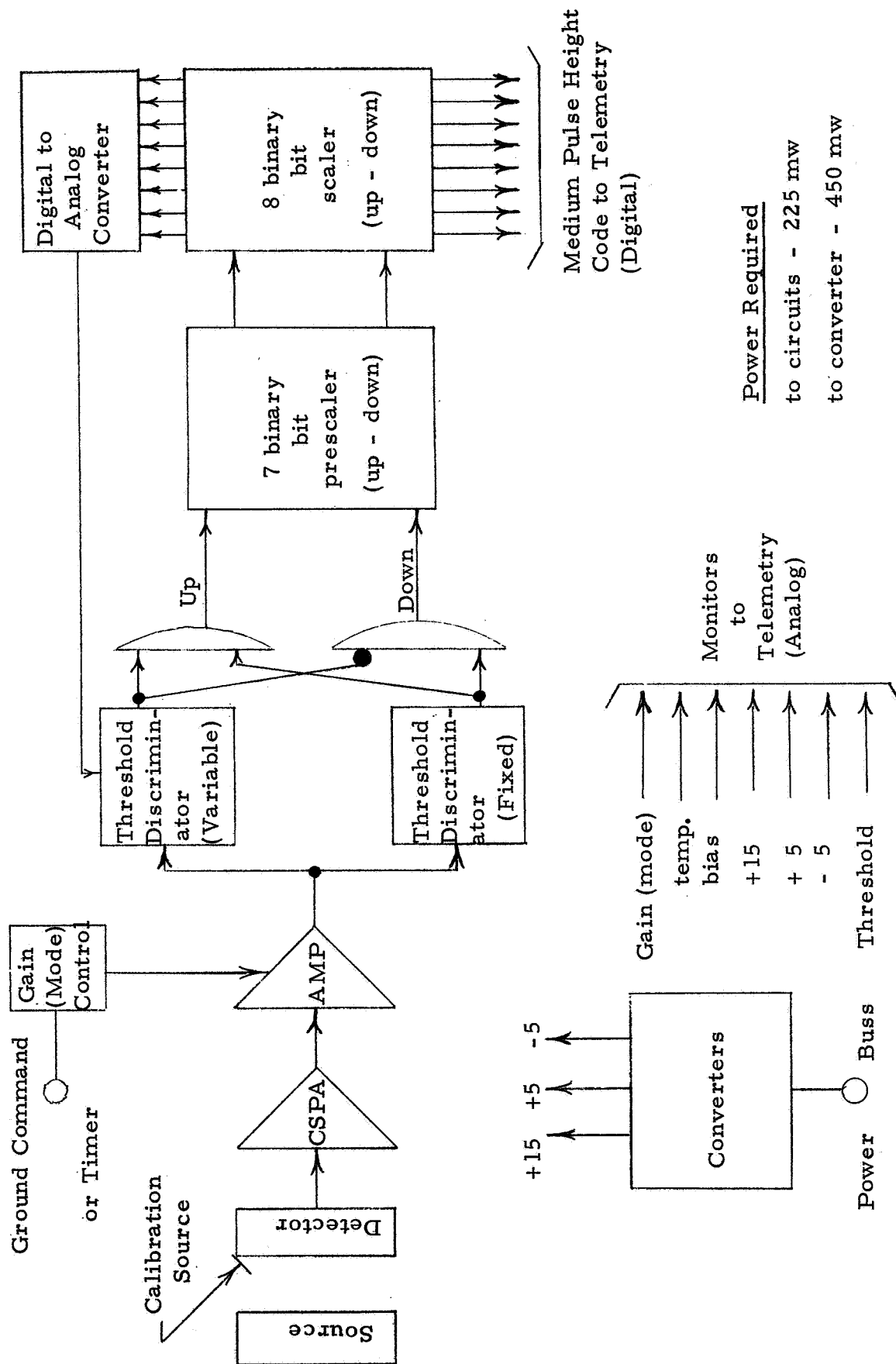


Figure 4.26. Electronics Design for Maximum Performance - Thin Source System.

is that the minimum step be less than σ_m . This is generally true for feedback from the top 8 binary bits.

The maximum performance system uses the power listed in Figure 4.26. The estimated weight is 0.7 lb and the total volume is 13 in³. The electronics housing would be that shown in Figure 4.23. The minimum and intermediate systems would use the housing in Figure 4.22.

The errors of the minimum power system would be as discussed above. The intermediate system errors are the $\delta\rho_2$ of Table 4.4, while the maximum system errors are the $\delta\rho_1$ of Table 4.4.

4.3.3 Thick Source Method

The thick source method results in two system designs. The minimum system electronics design is shown in Figure 4.27 along with estimated power requirements. This system would have a 1% TM error included in its response and thus the errors plotted in Figure 4.20 apply. The system would weigh about 0.5 lb and occupy a volume of 10 in³. It uses the electronics housing shown in Figure 4.22.

The maximum performance system electronics is shown in Figure 4.28 along with estimated power requirements. This system would use the housing in Figure 4.23, weigh about 0.7 lb, and occupy 13 in³. The errors for this system are just the statistical errors shown in Figure 4.19.

4.3.4 Comparison of Methods

A brief comparison of the thin source and thick source systems is made in Table 4.9. The data are taken primarily from Figures 4.19 and 4.20, Table 4.4, and Sections 4.3.2 and 4.3.3. It is easily seen that the thick source system can provide better accuracy at low densities while the thin source method provides better accuracy at high densities. The 3% density errors listed show that if only limited composition information is available then the thick source method is preferable since great accuracy at high densities is not required. In general, the thick source system is the more desirable since it allows measurements to be made with an approximately constant fractional error.

The major difficulties with the thick source method are that source reproducibility is only fair, and higher activities are required, since spectrum shaping with foils causes the loss of a significant fraction of the alpha particles. The former requires that each source have a separate calibration curve and that any interchange of sources be noted. This limitation need not be a serious drawback, however. The second difficulty arises only for Am²⁴¹ which has a high x-ray output. Thus the Am²⁴¹ thick source (at a given source-detector separation) will have a few times the x-ray output of the Am²⁴¹ thin source. The x-ray background will not affect the density measuring systems, but may

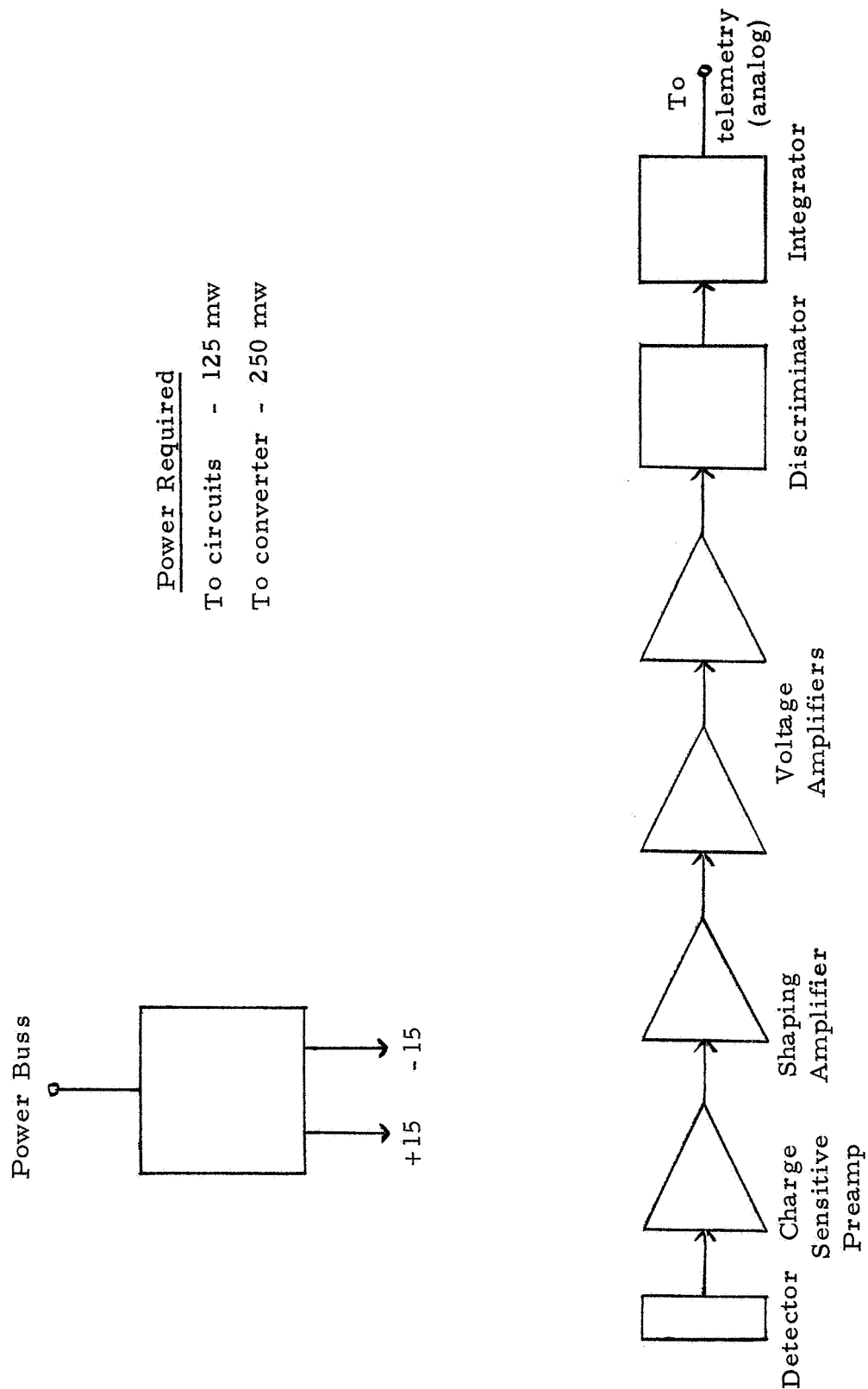


Figure 4.27. Electronics Design for Minimum Weight and Power Consumption - Thick Source System

Power Required

To circuits - 165 mw

To converter - 330 mw

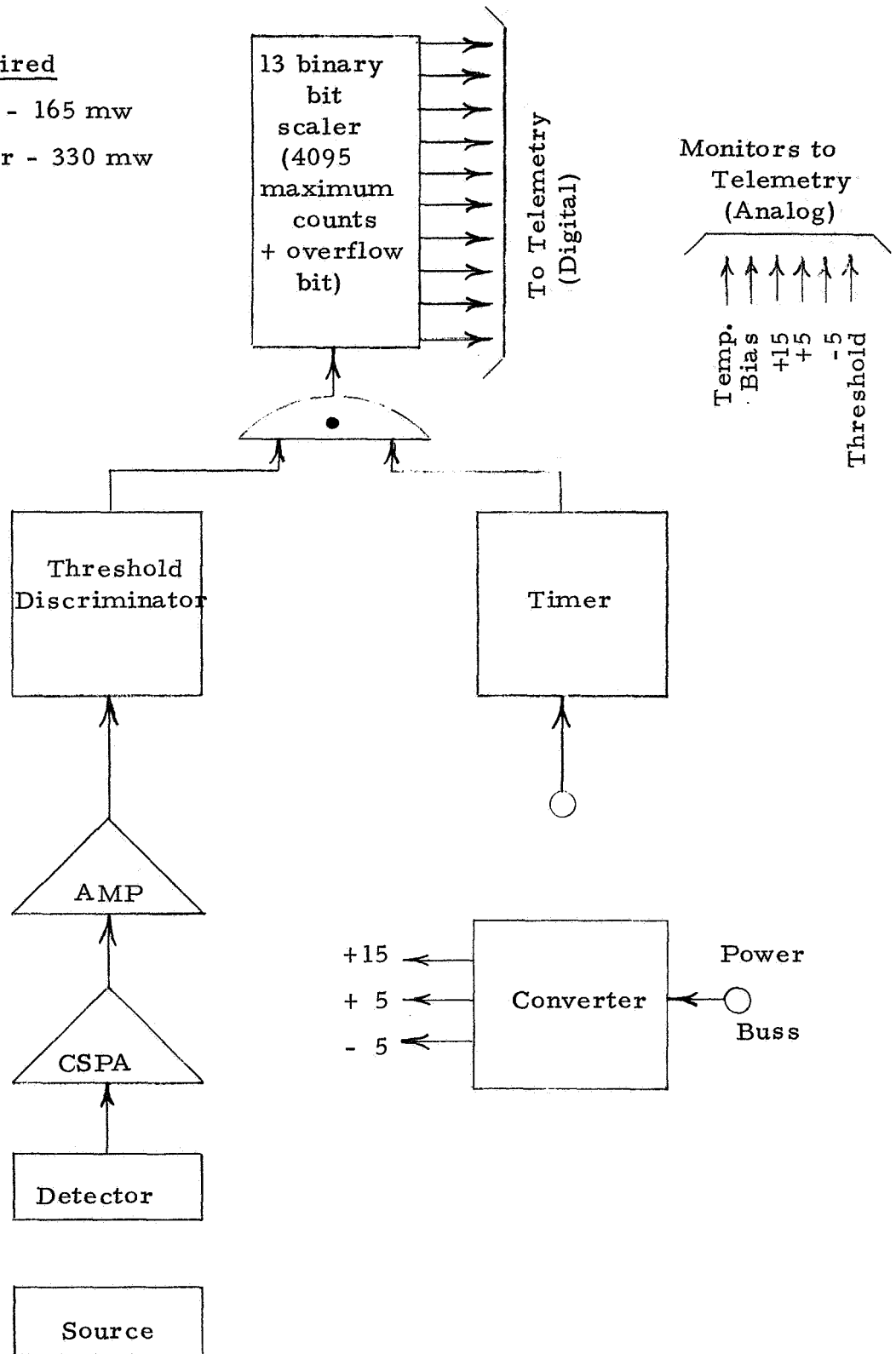


Figure 4.28. Electronics Design for Maximum Performance - Thick Source System.

affect other experiments on the lander. The latter point must be checked, and if any difficulty does arise it may be necessary to use weaker sources or else use Cm^{242} sources, which have only recently become available.

The best thick source system appears to be curve 3, which is based on the data from Am^{241} foil 112572/1 covered 1/2 with 0.15 mil Al foil. The detector was covered with 0.45 mil Al foil so the 0.25 MeV threshold was effectively about 3 MeV. This system works well at source-detector separations of 10-20 cm. Use of a thinner foil over the detector would lower the effective threshold and allow larger separations to be used.

5. ARGON COMPOSITION MEASUREMENT

5.1 General Discussion

The preceding sections show that for gases composed solely of CO_2 , N_2 and Ar it is possible to design an alpha particle density measuring system which gives an effective, or measured, density of

$$\rho_m = \rho_{\text{CO}_2} + \rho_{\text{N}_2} + 0.67 \rho_{\text{Ar}} \quad (5.1)$$

Equation (5.1) holds to about 2% and is applicable to the case where no composition information is available. The alpha particle systems can thus give a ρ_m which deviates from the true gas density by as much as 49% of ρ_m when used in pure Ar. For the Martian atmosphere VM-6 this reduces to a 12% deviation.

The alpha particle system can be made to yield true densities accurate to $\pm 2\%$ if the calibration is taken as the average of the CO_2 and N_2 calibrations, and if the percentage composition or density information is available from some other system. In the following sections two methods are described for obtaining the Ar density. Both methods are also affected by the CO_2 - N_2 density, so in effect a second equation of the form (5.1) is obtained. From these equations it is then possible to obtain $\rho_{\text{CO}_2} + \rho_{\text{N}_2}$ and ρ_{Ar} , separately. Both of these densities will have a minimum uncertainty of about 2% unless CO_2 - N_2 composition information is also available. Such additional information can be obtained from, say, radio propagation data (see e. g., Eq. (7) of Ref. 5.1), or from an on-board mass spectrometer. For the present we consider only the alpha particle systems and the Ar measuring systems described below.

5.2 Neptunium M X-Ray Attenuation

5.2.1 Theoretical Formulation

The use of x-ray attenuation to distinguish Ar from CO₂ and N₂ is based on the strong increase of x-ray absorption coefficients with Z ($\mu \propto Z^3$ for low Z , see Ref. 5.2). Since C, N and O have $Z = 6, 7$ and 8 , while Ar has $Z = 18$, it is seen that CO₂ and N₂ should have nearly equal absorption coefficients while that for Ar should be much larger. Since the x-ray absorption coefficient increases sharply for energies above the K absorption edge of an element, it will generally be advantageous to work with an x-ray energy above the K edges of the elements of interest. For C, N, O and Ar the K edges are at 0.283, 0.399, 0.531 and 3.203 keV, respectively, so it is obvious that the maximum sensitivity for Ar will occur with x-ray energies above 3.2 keV.

Since the x-ray absorption coefficient is roughly proportional to $E^{-2.5}$, the maximum sensitivity of an x-ray attenuation system occurs at low x-ray energies. For a system which has maximum sensitivity to Ar and minimum sensitivity to CO₂ and N₂, it is thus natural to seek an x-ray source with an energy just above the Ar K edge at 3.2 keV. An almost perfect source for the x-ray attenuation system thus appears to be Am²⁴¹ which emits a 3.33 keV Np M x-ray (average of the 3.253 and 3.428 keV lines). The intensity of the Np M x-rays is about 0.07 x-ray/a, as calculated from data given in Ref. 4.3. Thus vacuum sublimed Am²⁴¹ sources should be quite suitable as a source for the x-ray attenuation system.

The geometry for the x-ray attenuation system is much as shown in Figure 4.1, except that an x-ray source is used and the detector is now a proportional counter. For such a system the detector response is given by

$$I = I_0 e^{-(\rho_{\text{CO}_2} \mu_{\text{CO}_2} + \rho_{\text{N}_2} \mu_{\text{N}_2} + \rho_{\text{Ar}} \mu_{\text{Ar}}) D} \quad (5.2)$$

where $\mu_{\text{CO}_2} = 135 \text{ cm}^2/\text{g}$, $\mu_{\text{N}_2} = 107 \text{ cm}^2/\text{g}$, and $\mu_{\text{Ar}} = 1291 \text{ cm}^2/\text{g}$ for the 3.33 keV Np M x-rays (obtained from Ref. 5.3). If ρ is expressed in 10^{-6} g/cm^3 and $D = 30 \text{ cm}$, then (5.2) becomes

$$I = I_0 e^{-0.0387 (\rho_{\text{Ar}} + 0.105 \rho_{\text{CO}_2} + 0.083 \rho_{\text{N}_2})} \quad (5.3)$$

Here I is the detector response in x-rays/sec and I_0 is the response at zero density.

The form of (5.3) indicates that the Np M x-ray attenuation system

should give a measured density of

$$\rho'_m = \rho_{Ar} + 0.105 \rho_{CO2} + 0.083 \rho_{N2} \quad (5.4a)$$

$$\approx \rho_{Ar} + 0.094 (\rho_{CO2} + \rho_{N2}) \quad (5.4b)$$

where the system calibration is made with Ar. Note that the coefficient 0.094 in the second form of (5.4) is only accurate to about 10%.

Equations (5.1) and (5.4) can be combined to give

$$(\rho_{CO2} + \rho_{N2}) = 1.07 \rho_m - 0.72 \rho'_m \quad (5.5)$$

and

$$\rho_{Ar} = 1.07 \rho'_m - 0.100 \rho_m \quad (5.6)$$

The statistical errors are then

$$\delta(\rho_{CO2} + \rho_{N2})_{st} = \left\{ (1.07 \delta \rho_m)^2 + (0.72 \delta \rho'_m)^2 \right\}^{1/2} \quad (5.7)$$

and

$$\delta(\rho_{Ar})_{st} = \left\{ (1.07 \delta \rho'_m)^2 + (0.100 \delta \rho_m)^2 \right\}^{1/2} \quad (5.8)$$

The systematic errors arise from the variations in the coefficients of Equations (5.1) and (5.2). The errors are 0.67 ± 0.02 , 0.094 ± 0.01 , and ± 0.02 in the N_2 coefficient in (5.1). From this it is found that the systematic errors are

$$\begin{aligned} \delta(\rho_{CO2} + \rho_{N2})_{sys} &= \left\{ (0.02 \rho_m)^2 + (0.02 \rho'_m)^2 \right\}^{1/2} \\ &\approx 0.02 \rho \left\{ 1.01 - 0.49 w_{Ar} + 0.93 w_{Ar}^2 \right\}^{1/2} \end{aligned} \quad (5.9)$$

and

$$\begin{aligned}\delta(\rho_{\text{Ar}})_{\text{sys}} &= \left\{ (0.02 \rho_{\text{m}})^2 + (0.01 \rho_{\text{m}})^2 \right\}^{1/2} \\ &\approx 0.01 \rho \left\{ 1.04 + 0.02 w_{\text{Ar}} + 3.39 w_{\text{Ar}}^2 \right\}^{1/2}\end{aligned}\tag{5.10}$$

where ρ is the total density and w_{Ar} is the Ar mass fraction. Using (5.9) and (5.10) we find that

	$w_{\text{Ar}} = 0$	$w_{\text{Ar}} = 1$	
$\delta(\rho_{\text{CO}_2} + \rho_{\text{N}_2})_{\text{sys}} =$	0.020	0.024	$\times \rho$
$\delta(\rho_{\text{Ar}})_{\text{sys}} =$	0.010	0.021	$\times \rho$

(5.11)

Thus, if statistical errors can be made sufficiently small the two systems should give $\rho_{\text{CO}_2} + \rho_{\text{N}_2}$ and ρ_{Ar} to within about 2% each, assuming no additional composition information is available.

5.2.2 Experimental Results

The experimental tests were made with a layout similar to that shown in Figure 4.1. Vacuum sublimed Am^{241} sources are required, since gold layers greater than about $500 \mu\text{g}/\text{cm}^2$ absorb most of the Np M x-rays, thus making foil sources unsuitable. The x-rays were detected with a 90% Ar-10% CH_4 filled proportional counter having a 0.5 inch diameter, 2 mil thick Be window, and a 0.5 inch depth. The detection efficiency of the proportional counter is plotted in Figure 5.1 (the solid curve), while the measured Np M x-ray spectrum is shown in Figure 5.2.

Figure 5.1 also shows the locations of the Np M x-ray and the Ar K x-ray, as well as the detection efficiency for a 90% Kr + 10% CH_4 gas fill. Since the ideal detector has unit efficiency for the Np M x-ray, and zero efficiency for other energies, particularly for the interfering Ar K x-ray which is produced by the various x-rays from Am^{241} as well as the α particles, the chosen proportional counter is about the most suitable available detector for the Np M x-ray attenuation system. Even so, the spectrum in Figure 5.2 shows that a significant amount of background exists in the measured Np M x-ray spectrum. This background arises from the higher energy x-rays in

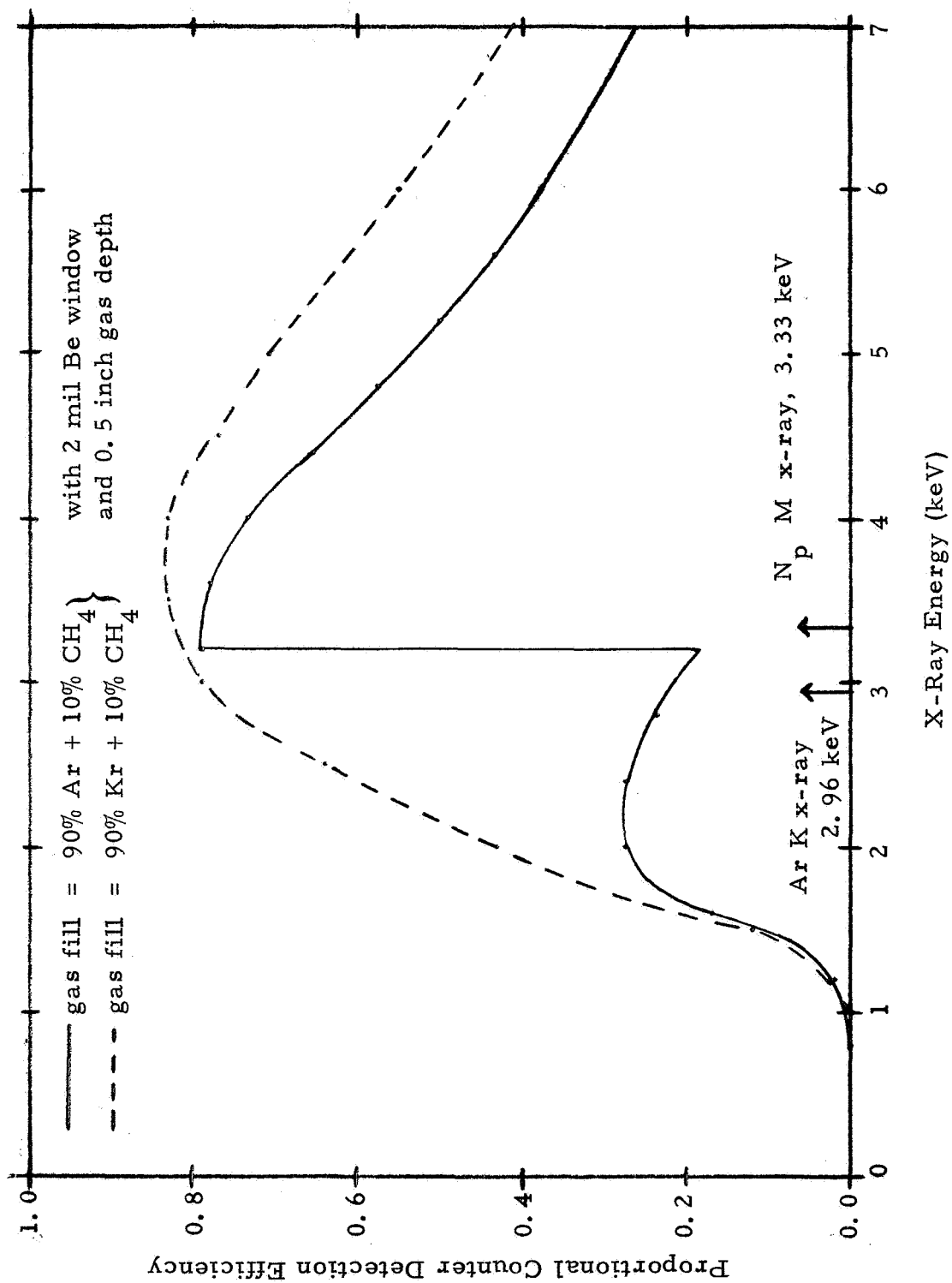


Figure 5.1 Proportional Counter Detection Efficiency for X-Rays.

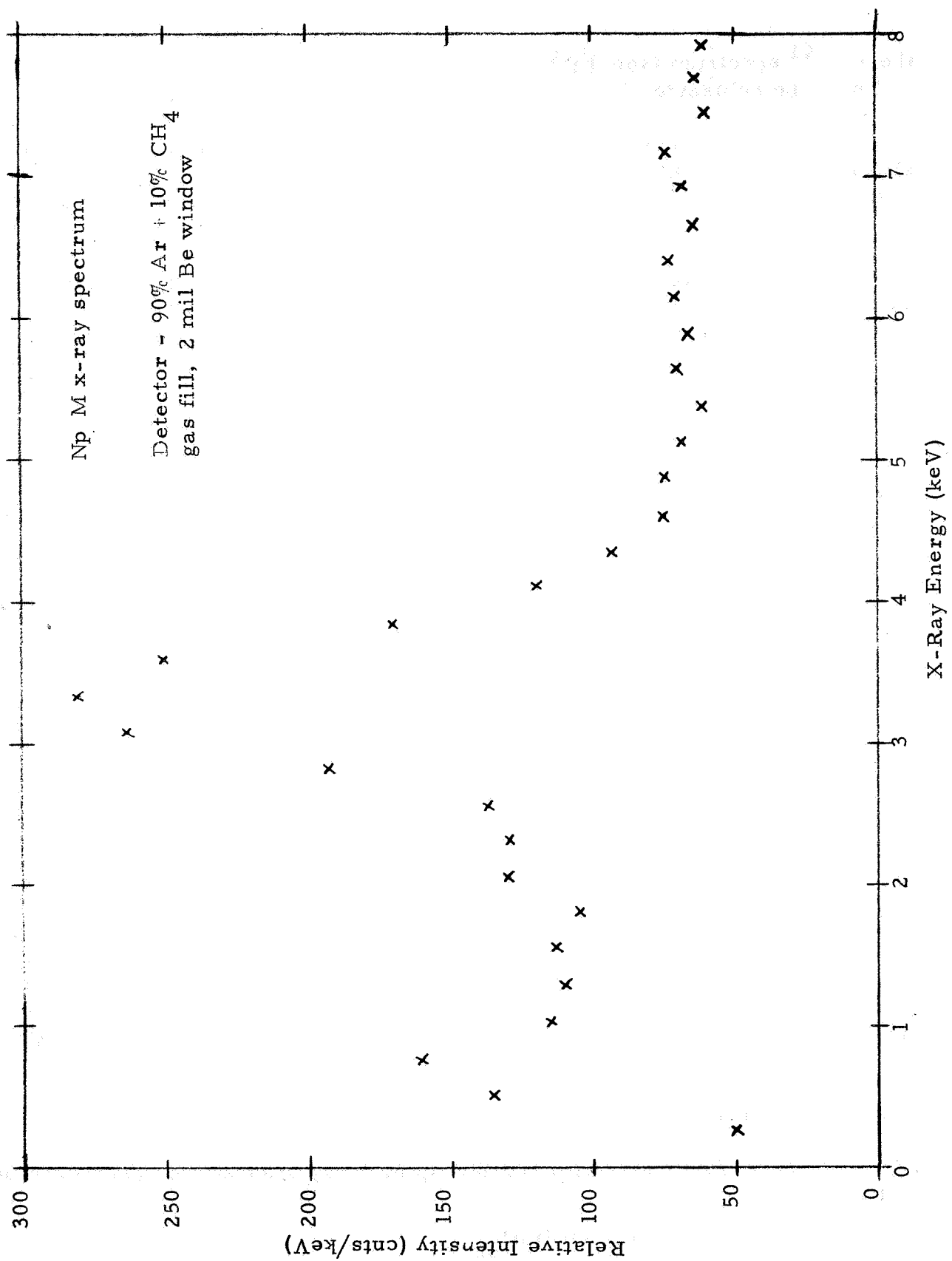


Figure 5.2 Np M X-Ray Spectrum.

the Am^{241} spectrum (see Table 4.1), cosmic rays, and natural radioactivity, and must be subtracted to obtain a true measure of the Np M x-ray attenuation.

Results obtained with Am^{241} sources covered with 3 mils of Be are shown in Figure 5.3. The Be stops the α particles but transmits about 75% of the Np M x-rays. This is important to prevent interference from the Ar K x-rays produced by α excitation. Source-detector separation is 30 cm, and results are shown for CO_2 , N_2 , and Ar. The theoretical curves are based on Eq. (5.3). The agreement between theory and experiment is quite satisfactory. The data plotted in Figure 5.3 have had background subtracted by using a higher energy window and multiplying the counts in this window by about 1.2 to account for the slight decrease in background at higher energies. It should be noted that although the α particles striking Be produce some neutrons, since the α sources are about 1 m Ci or less this component of radiation can be neglected.

Figure 5.4 shows data taken with an uncovered α source, and plotted using the effective density of (5.4b). The high density Ar data show contamination by the α -produced Ar K x-rays. The experimental points at lower densities show reasonable agreement (within the statistical errors) with Eq. (5.4b) for CO_2 , N_2 and Ar gas composition. Figure 5.5 is a similar plot for Ar and N_2 , but with a 2 inch ID Al pipe surrounding the source-detector path. Here the Ar K x-ray production is reduced, though not eliminated, and the deviation of theory and experiment for Ar at high densities is substantially less. Note the excellent agreement of N_2 and Ar with Eq. (5.4b).

The experimental results allow us to make the following general conclusions. First, the CO_2 , N_2 and Ar x-ray attenuation measurements are in reasonable agreement with the theoretical formulation (5.3). Second, the α source should be covered with a low Z foil (say, Be) to stop the α particles but allow the Np M x-rays to escape. This is necessary to avoid contamination by the α -produced Ar K x-rays. Third, an Ar filled proportional counter ($\text{Ar} + \text{CH}_4$ or $\text{Ar} + \text{CO}_2$) is best for the system. Fourth, background will form about 10% of the measured, unattenuated x-ray intensity and must be subtracted. This limits the maximum usable attenuation to about a factor of 10, and the maximum source-detector separation to about 30 cm for pure Ar. Fifth, the experimental results are in reasonable agreement with Eq. (5.4b), thus allowing calibration in terms of an effective density with no distinction between CO_2 and N_2 .

5.2.3 Expected Errors for the X-Ray Attenuation System

The calibration curve for the Np M x-ray attenuation system can be written as

$$N_x = N_o e^{-\mu D \rho' m} + B_x \quad (5.12)$$

Vacuum sublimed Am^{241} source + 3 mils Be

D = 30 cm

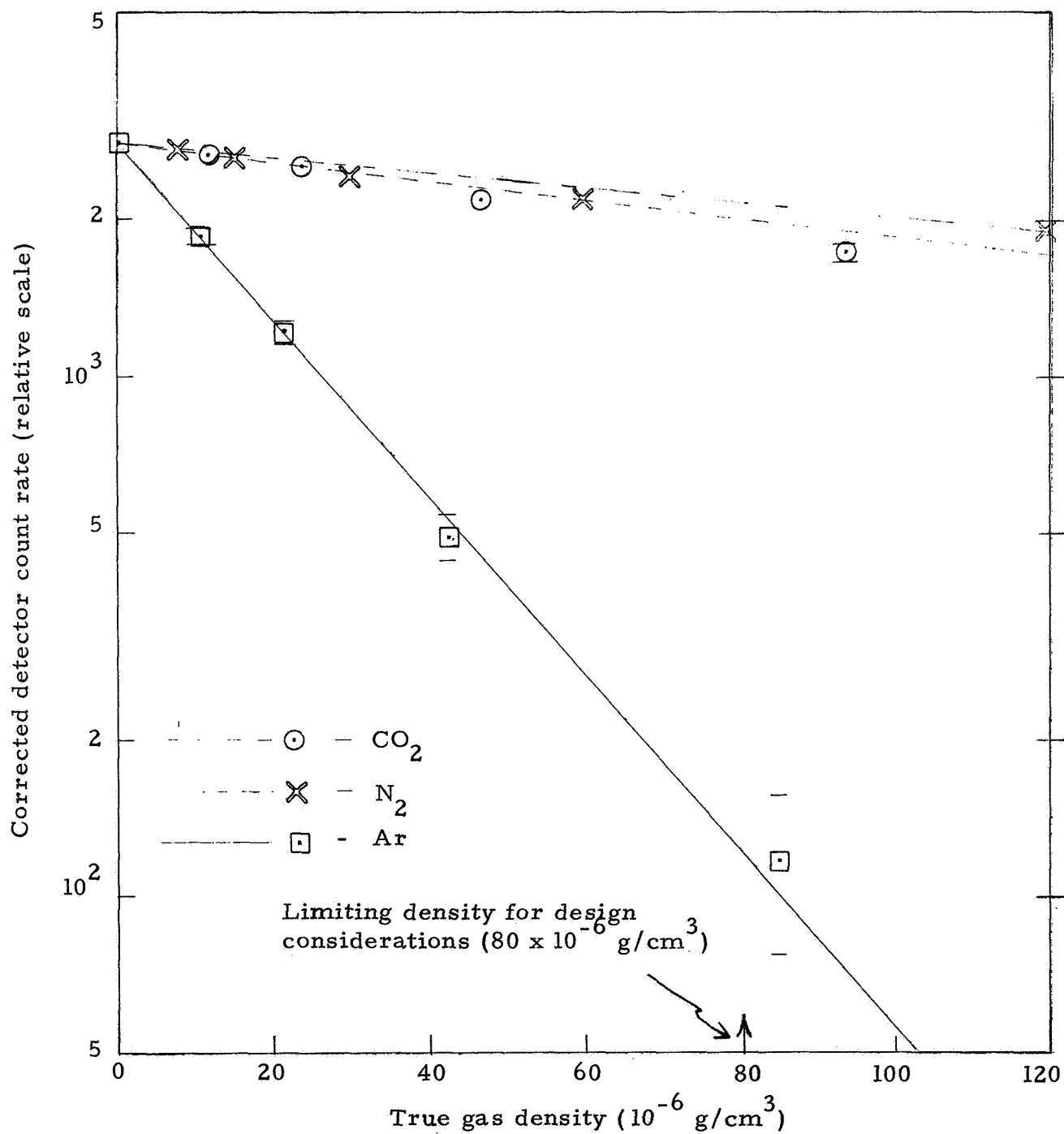


Figure 5.3. Np M X-Ray Attenuation Results - Source Covered with 3 mils Be.

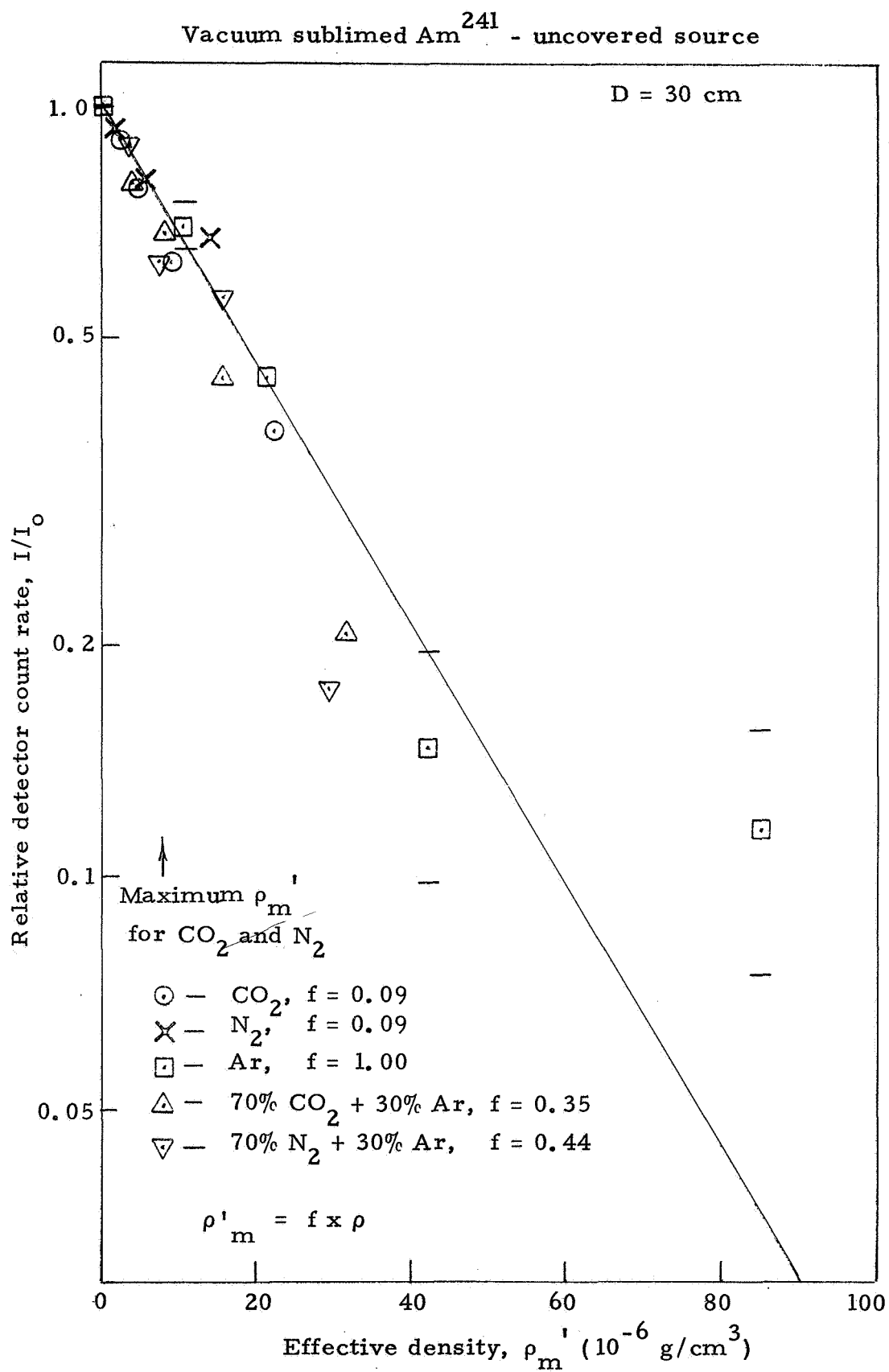


Figure 5.4. Np M X-Ray Attenuation Results - Source Uncovered.

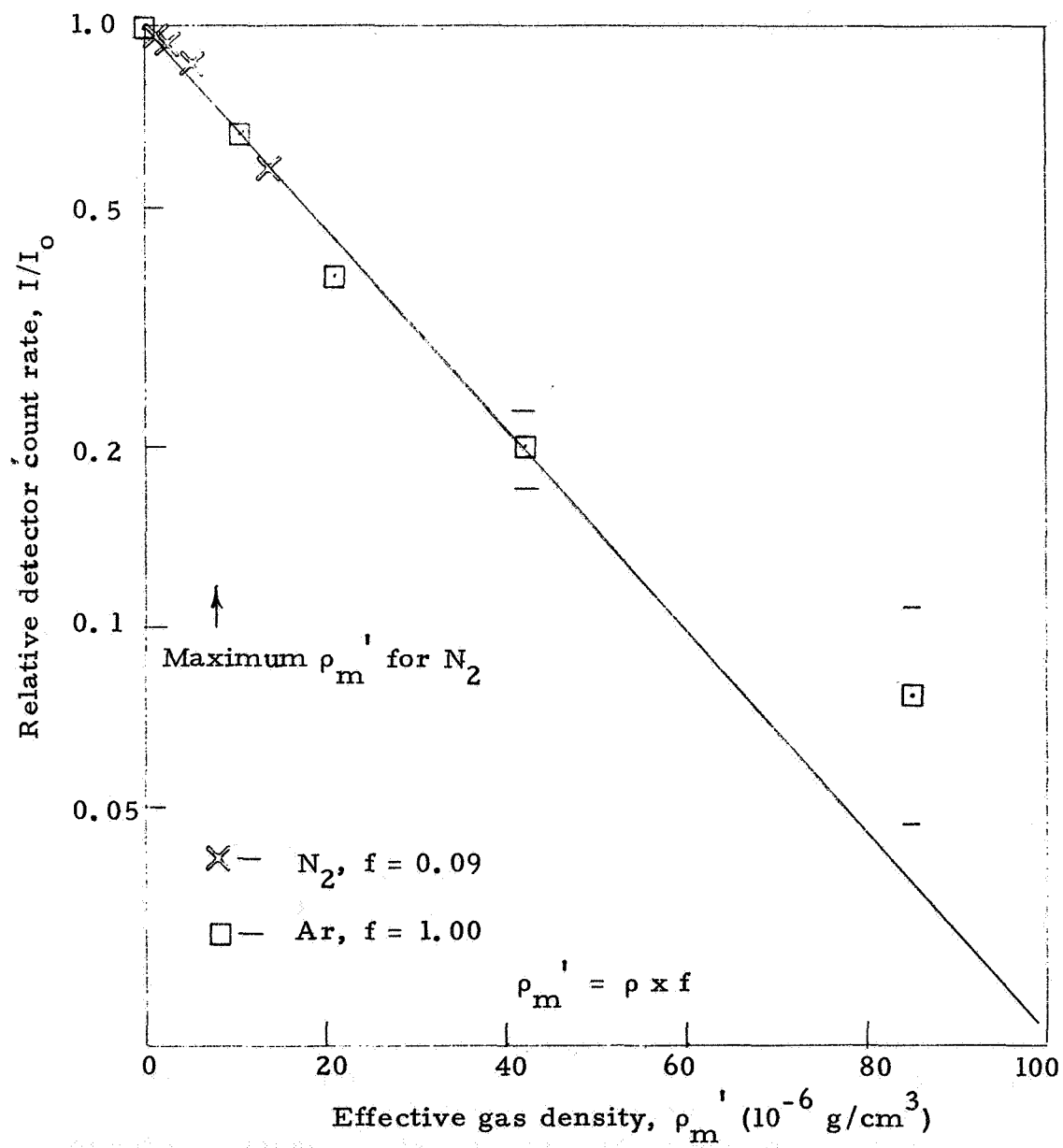


Figure 5.5. Np M X-Ray Attenuation Results - Source Partially Collimated.

which is (5.2) modified to include a background count rate B_x , measured at higher energy, and where μ is the absorption coefficient of Ar, N_x is the measured M x-ray, and N_0 is the true M x-ray count at zero density. Thus

$$\rho'_m = \frac{1}{\mu D} \ln \left(\frac{N_0}{N_x - B_x} \right) \quad (5.13)$$

and

$$\delta \rho'_m = \frac{1}{\mu D (N_x - B_x)} \left\{ (\delta N_x)^2 + (\delta B_x)^2 \right\}^{1/2} \quad (5.14a)$$

$$= \frac{\sqrt{(N_x + B_x)/T}}{\mu D (N_x - B_x)} \quad (5.14b)$$

Equation (5.14b) assumes that only statistical errors contribute to $\delta \rho'_m$ and that T seconds are used to make a measurement.

The values of N_0 and B_x are chosen as follows. The measured M x-ray yield is about 0.03 x-rays/a, and an α source activity of about 1 m Ci is assumed as reasonable. The proportional counter can be made with a 2" x 2" window ($\approx 25 \text{ cm}^2$), and with a detection efficiency as shown in Figure 5.1. Under these conditions $N_0 \approx 2000/\text{sec}$ and $B_x \approx 200/\text{sec}$. It is assumed here that the background is 10% of the zero density count rate, and is constant over the expected density range. Proper care in the construction of an actual system may reduce the background, but since the background on Mars may be higher it must still be measured. For the present, it is assumed that $B_x = 200/\text{sec}$ for all densities. Using this system, (5.14b) then gives the errors in ρ'_m listed in Table 5.1. These values must then be used along with $\delta \rho_m$ from the α particle system to obtain $\delta (\rho_{\text{CO}_2} + \rho_{\text{N}_2})$ and $\delta \rho_{\text{Ar}}$ from Equations (5.7) and (5.8). This is done in Sections 5.4 and 6.3.

5.2.4 Proposed System Designs

The electronics design for the Np M x-ray attenuation system is shown in Figure 5.6. The two level mode control changes the window alternately from being centered on the Np M x-ray to a higher level in order to measure background. Replacement of the ≈ 15 bit counter with an analog output count rate circuit would reduce circuit power by perhaps 40 mw. With the system designed to yield a minimum count rate equal to about 10% of the maximum of 2000/sec (= 20,000 counts in 10 sec), only the highest 10 bits need be read out by telemetry. The electronics housing would be about the

Table 5. 1

Statistical Errors for the Np M X-Ray
Attenuation System

From Eq. (5. 14b), with $N_o = 2000/\text{sec}$, $B_x = 200/\text{sec}$, and
 $T = 10 \text{ sec}$.

ρ'_m (10^{-6} g/cm^3)	N_x (sec^{-1})	$\delta \rho'_m$ (10^{-6} g/cm^3)
0	2200	0.20
10	1558	0.25
20	1122	0.32
40	625	0.55
60	395	1.02
80	290	2.01

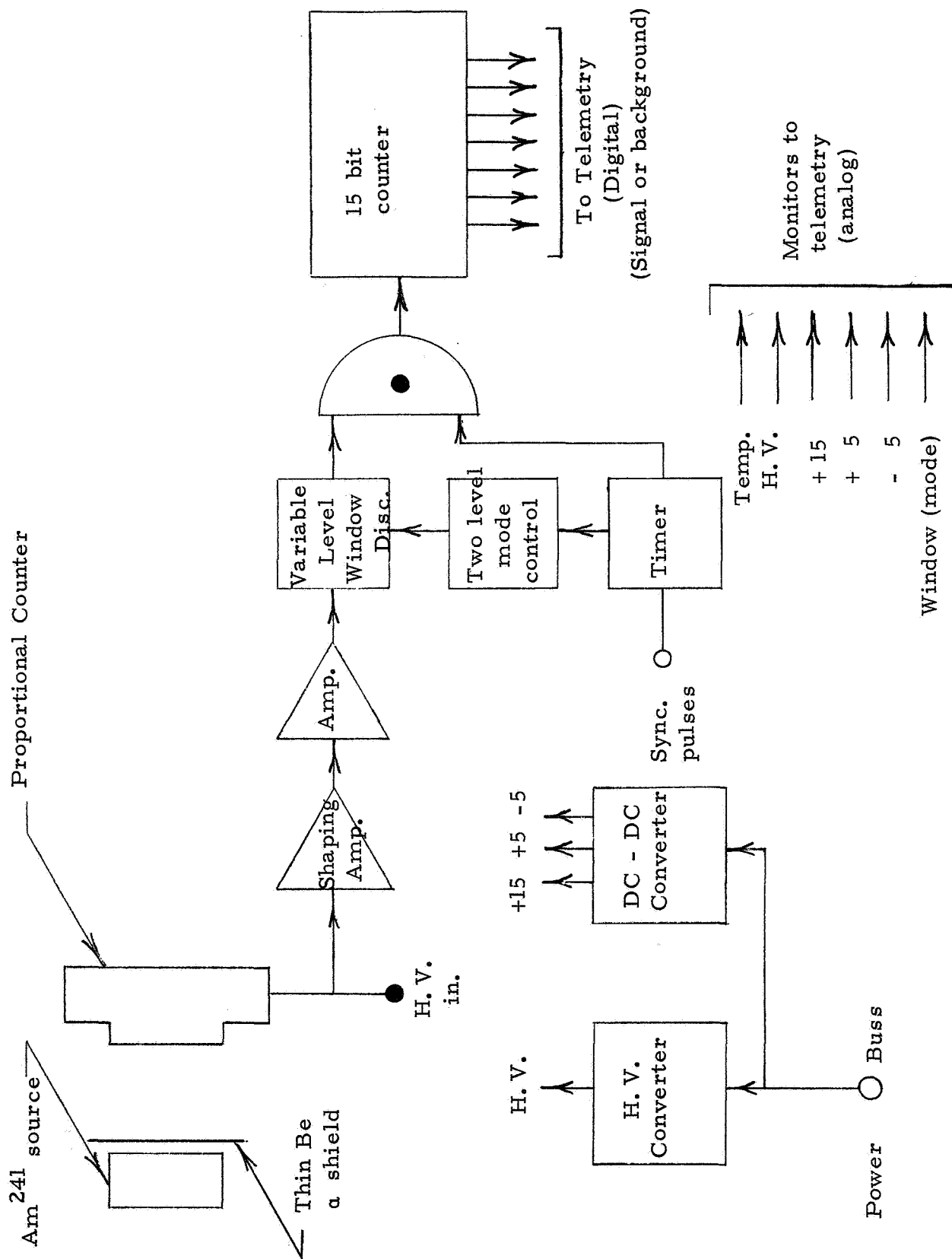


Figure 5.6. Electronics Design for the Np M X-Ray Attenuation System

size shown in Figure 4.23, except for the solid state detector.

The proportional counter for the maximum performance system has a window about 2" x 2" of 2 mil Be. The filling should be Ar with CO₂ used as the quench gas (CH₄ decomposes under high count rates and thus severely limits the proportional counter lifetime). The counter can be constructed of Be to minimize weight. Under these conditions the system would weigh about 1-1/4 lbs and occupy a total volume of about 20 in³.

Weight can be reduced further primarily by use of a smaller proportional counter. The electronics cannot be significantly reduced in weight and power requirements, but by using a smaller proportional counter (1 to 2 cm² area) the weight can be reduced to about 3/4 lb and the volume to 15 in³.

5.3 Argon Fluorescent X-Ray Measurement

5.3.1 Theoretical Formulation

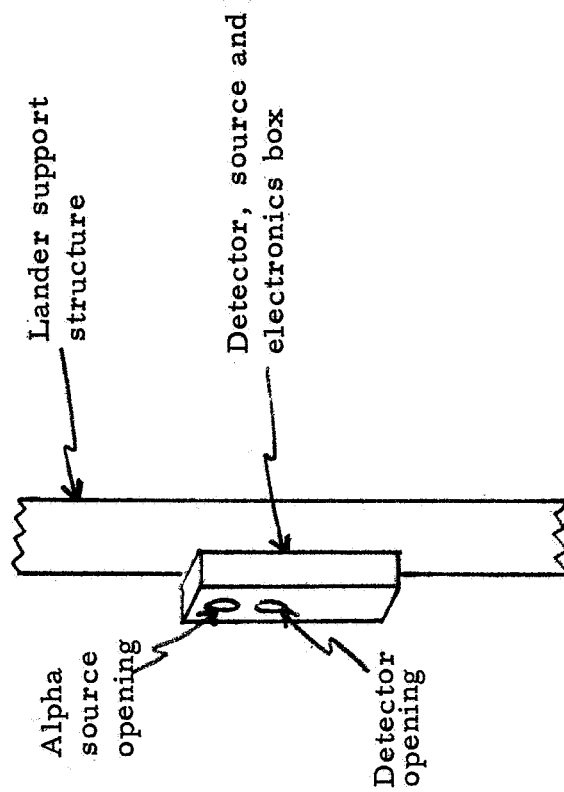
The production of fluorescent x-rays by heavy charged particles is a well-known phenomenon, and theoretical calculations of the cross sections have been in existence for quite some time (e.g., Ref. 5.4). A general discussion of the work before 1958 is given in Ref. 5.5. For the present it is only necessary to consider the production of Ar K x-rays by α particles.

A rough theoretical expression for the count rate of a proportional counter viewing Ar excited by α particles can be obtained as follows. The geometry of Figure 5.7 is assumed, with the source and proportional counter sufficiently close so that the distances from a given gas volume element to each are about equal. Under these conditions the detected x-ray count rate is

$$N_{xm} = \frac{A\epsilon}{4\pi} N_a \frac{\rho_{Ar} N_A}{M_{Ar}} \int_0^{r_{max}} e^{-r(\mu_{Ar} \rho_{Ar} + \mu_2 \rho_2)} \sigma_K[E(r)] \frac{dr}{r^2} \quad (5.15)$$

where A and ϵ are the proportional counter area and detection efficiency, N_a is the source emission intensity in α 's/sec, N_A is Avogadro's number, M_{Ar} is the atomic weight of Ar, μ_{Ar} is the attenuation coefficient of Ar for its own K x-rays, ρ_{Ar} is the density of Ar in the gas, μ_2 is the attenuation coefficient of CO₂-N₂ for the Ar K x-rays (assumed equal), ρ_2 is the CO₂-N₂ density in the gas, r is the distance from the source to the gas volume (assumed equal to the distance from the proportional counter to the gas volume), r_{max} is the range of the α particles in the gas, and $\sigma_K[E(r)]$ is the K x-ray production cross section for Ar by α particles of energy E and residual range r.

Equation (5.15) will be evaluated using the following approximations. E(r) is taken as



Volume in front of detector
and source should be
free of obstruction

Figure 5.7 Outline of the Argon Fluorescent X-ray Detection System to be Used on a Martian Lander

$$E(r) = \left[r \rho_m / R_o \right]^\beta \quad (5.16)$$

where ρ_m is given by (5.1). By fitting the $\text{CO}_2\text{-N}_2$ stopping power data of Figure 3.8 at 1 and 5 MeV it is found that $\beta = 0.43$ and $R_o = 4.53 \text{ mg MeV}^\beta / \text{cm}^2$. The cross section can be approximated by

$$\sigma_K(E) = \sigma_o E^\gamma \quad (5.17)$$

with σ_o and γ constants. From Ref. 5.5, $\gamma \approx 4$ can be used for an initial estimate, though α particles of a few MeV are in the region where γ begins to decrease.

Using (5.16) and (5.17) in (5.15), assuming r_{max} large enough to be set to infinity, and $\beta \gamma \approx 2$, there results

$$N_{\text{xm}} \approx K w_{\text{Ar}} (\rho_m)^2 \quad (5.18)$$

where K is a constant and w_{Ar} is the Ar mass fraction. Equation (5.18) also assumes a monoenergetic α source (not necessarily true), and that μ of CO_2 , N_2 and Ar for the Ar K x-rays are all about equal (approximately true). In light of all the approximations Eq. (5.18) should be considered as only a starting point for experimental analysis. A more exact calculation would not be profitable since N_{xm} also depends on the source spectrum shape, and because $\sigma_K[E(r)]$ is not known very well.

5.3.2 Experimental Results

Data were obtained with a configuration similar to that shown in Figure 5.7. The proportional counter used had a 0.5 inch diameter, 2 mil thick Be window, a 0.5 inch depth and a gas fill of 90% Kr + CH_4 at one atmosphere. This gas fill provides good detection efficiency for the Ar K x-rays, as shown by Figure 5.1. The α source used was the nominally 15 m Ci (measured to be 11.7 m Ci) Am^{241} foil source #112572/1, whose spectrum is shown in Figure 4.7.

The results of five gas compositions are shown in Figure 5.8. Note the maximum in the yield of one of the curves. This is expected theoretically as at very high densities the α particles are stopped so near the source that few x-rays can reach the proportional counter. The data are replotted on a log-log

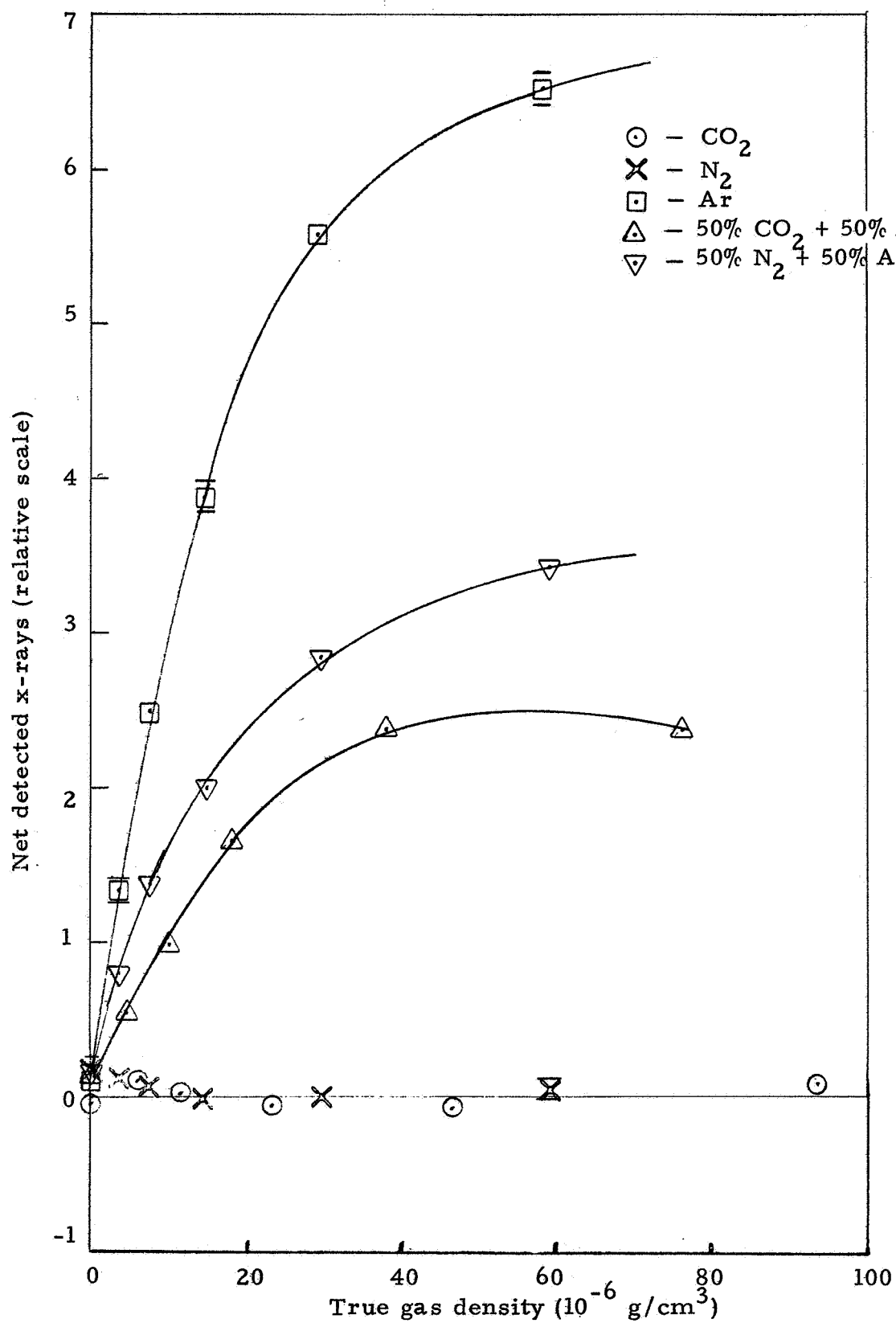


Figure 5.8. Results of the Ar K X-Ray Production Measurements.

scale in Figure 5.9. This is done to allow fitting an equation of the form

$$N_{xm} = N_o w_{Ar}^a \rho_m^b + N_b \quad (5.19)$$

Thus the plots are of $N_{xm} - N_b$, where N_{xm} is the measured detector count rate for the Ar K x-ray peak, N_b is the background measured at a higher energy, and $N_o w_{Ar}^a \rho_m^b$ is the true contribution from the Ar K x-rays. Here a and b are constants to be determined experimentally.

The data in Figure 5.9 give the results for b which are listed in Table 5.2. Figure 5.10, taken from points on the curves of Figure 5.8, allows values of a to be calculated, and these are also listed in Table 5.2. As shown in Table 5.2, the experimental results can be roughly fitted by (for a 1.27 cm² window on the proportional counter)

$$N_{xm} = \left(1.3 w_{Ar}^{1.5} \rho_m^{0.75} + 7.5 \right) \text{ cnts/sec} \quad (5.20)$$

The result (5.20) is not sufficiently accurate for use with a final design system, but it does allow estimates of system accuracy to be made. An actual system must use calibration curves similar to either Figures 5.9 or 5.10.

5.3.3 Expected Errors for the Fluorescent X-Ray System

The errors can be calculated from the approximate response (5.20). Assuming an approximately 10 m Ci Am²⁴¹ foil source and a 25 cm² detector area the response becomes

$$N_{xm} \approx \left(26 w_{Ar}^{1.5} \rho_m^{0.75} + 148 \right) \text{ cnts/sec} \quad (5.21)$$

where it is assumed that the background also increases with detector window area. From (5.21) the statistical errors then give

$$\delta w_{Ar} = \frac{w_{Ar} (N_x + 296)^{1/2}}{1.5 N_x T^{1/2}} \quad (5.22)$$

where

$$N_x = 26 w_{Ar}^{1.5} \rho_m^{0.75} \quad (5.23)$$

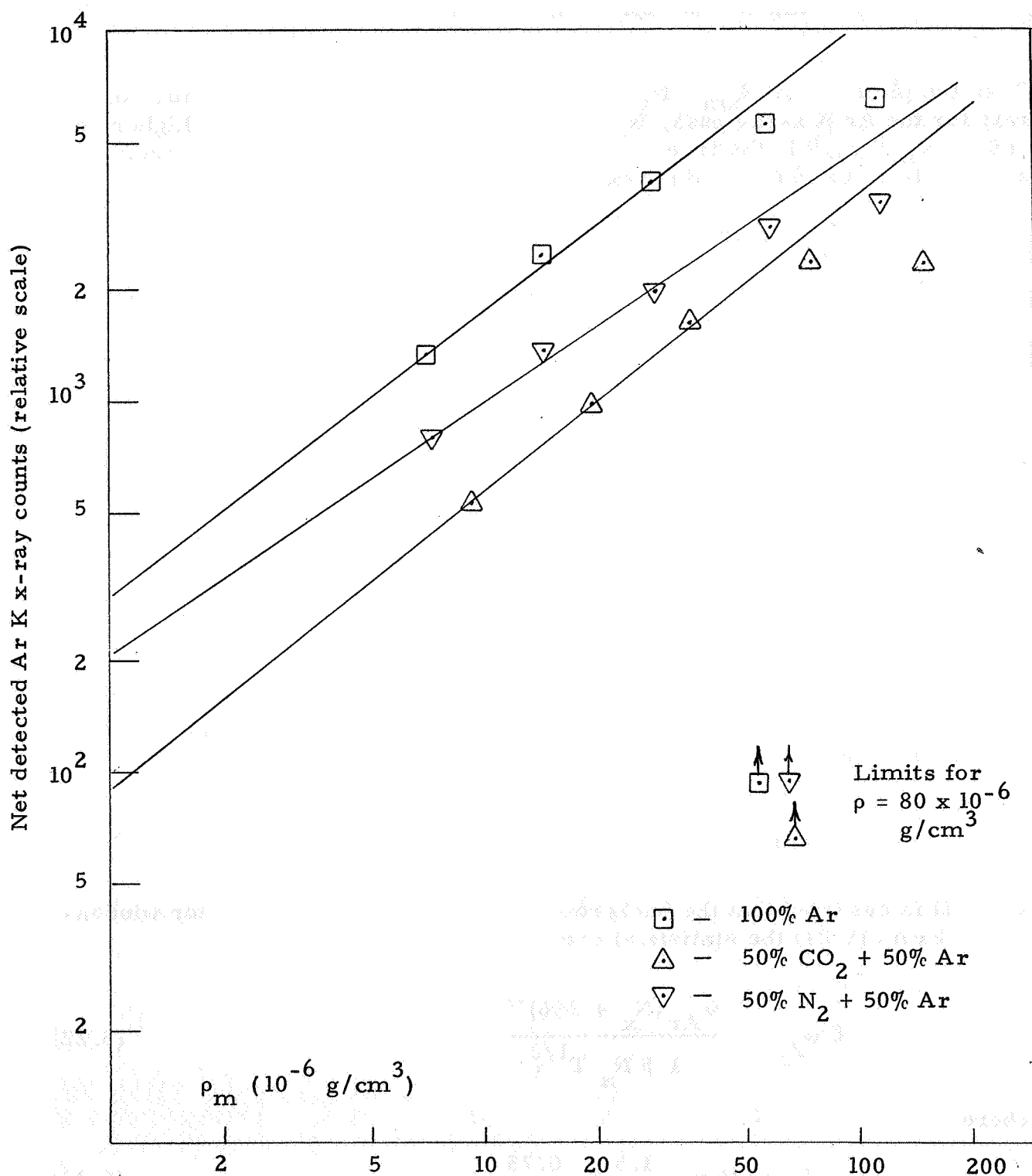


Figure 5.9. Power Law Fits to the Ar K X-Ray Data.

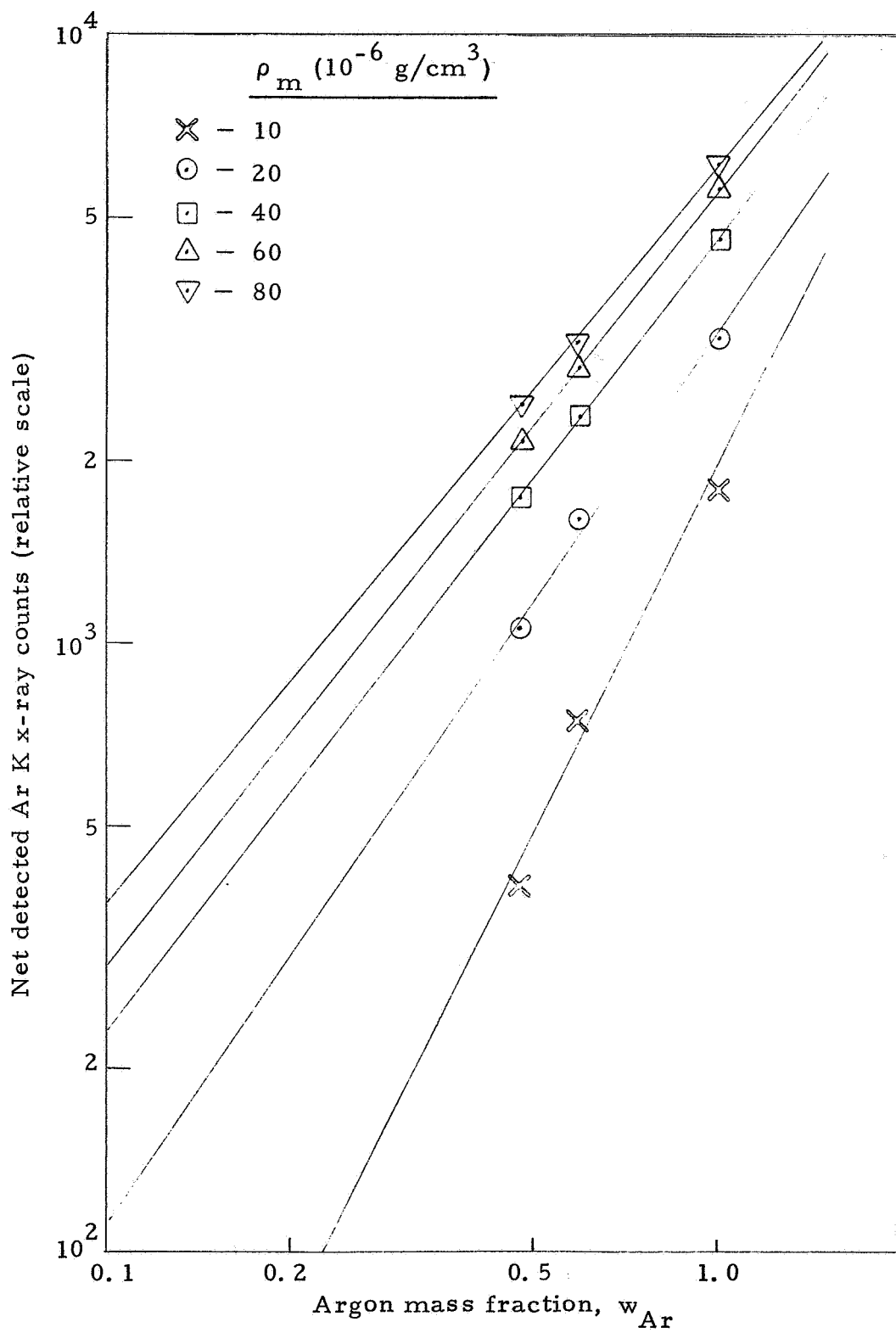


Figure 5.10 Plots of the Ar K X-Ray Data on an Ar Mass Fraction Scale.

Table 5.2

Results of the Ar K X-Ray Measurements

$$\text{Fit of } (N_{xm} - N_b) = N_o w_{Ar}^a \rho_m^b$$

From Figure 5.9:

From Figure 5.10:

w_{Ar}	b	$\rho_m (10^{-6} \text{ g/cm}^3)$	a
1.00	0.77	10	2.01
0.59	0.68	20	1.48
0.48	<u>0.80</u>	40	1.31
Average =	0.75	60	1.29
		80	<u>1.22</u>
			Average ≈ 1.5

If ρ_m is in 10^{-6} g/cm^3 , then

$$N_o \approx 1.3 \text{ cts/sec}$$

$$N_b \approx 7.5 \text{ cts/sec}$$

so

$$N_{xm} \approx \left(1.3 w_{Ar}^{1.5} \rho_m^{0.75} + 7.5 \right) \text{ cts/sec}$$

and T is the counting time in seconds. Equation (5.22) breaks down for $\rho_m = 0$, and $w_{Ar} = 0$. For $\rho_m = 0$ there is obviously no composition information available. For $w_{Ar} = 0$ the error becomes, using $T = 10$ sec,

$$\delta w_{Ar} = \frac{0.444}{\rho_m \cdot 0.50} \quad (5.24)$$

where (5.24) is the maximum value of w_{Ar} allowed by the statistical errors (one standard deviation). The results of (5.22) and (5.24) are listed in Table 5.3 for $T = 10$ sec. It is assumed that ρ_m is obtained from the α particle system, and errors in ρ_m are neglected. The system then yields the Ar mass fraction, w_{Ar}

From Eq. (5.1) and

$$w_{Ar} = \rho_{Ar} / (\rho_{CO2} + \rho_{N2} + \rho_{Ar}) \quad (5.25)$$

there results

$$\rho_{CO2} + \rho_{N2} = \rho_m \left[\frac{1 - w_{Ar}}{1 - 0.33 w_{Ar}} \right] \quad (5.26)$$

and

$$\rho_{Ar} = \rho_m \left[\frac{w_{Ar}}{1 - 0.33 w_{Ar}} \right] \quad (5.27)$$

From (5.26) and (5.27) there follows

$$\delta(\rho_{CO2} + \rho_{N2}) = \left\{ \left(\frac{1 - w_{Ar}}{1 - 0.33 w_{Ar}} \right)^2 (\delta \rho_m)^2 + \frac{(0.67 \rho_m \delta w_{Ar})^2}{(1 - 0.33 w_{Ar})^4} \right\}^{1/2} \quad (5.28)$$

and

$$\delta \rho_{Ar} = \left\{ \left(\frac{w_{Ar}}{1 - 0.33 w_{Ar}} \right)^2 (\delta \rho_m)^2 + \frac{(\rho_m \delta w_{Ar})^2}{(1 - 0.33 w_{Ar})^4} \right\}^{1/2} \quad (5.29)$$

These equations are used below in Section 5.4.

Table 5.3

Expected Errors for the Fluorescent X-Ray System

10 second integration time

$$w_{\text{Ar}} = \text{Ar mass fraction} ; \rho_m = \rho_{\text{CO}_2} + \rho_{\text{N}_2} + 0.67 \rho_{\text{Ar}}$$

ρ_m (10^{-6} g/cm^3)	$w_{\text{Ar}} = 0.00$ δw_{Ar}	$w_{\text{Ar}} = 0.35$ δw_{Ar}	$w_{\text{Ar}} = 1.00$ δw_{Ar}
0	1.0	1.0	1.0
10	0.14	0.04	0.03
20	0.10	0.03	0.02
40	0.07	0.017	0.014
60	0.06	0.013	0.011
80	0.05	0.011	0.010

5.3.4 Proposed System Designs

The Ar K x-ray detection system uses electronics identical to those of the Np M x-ray attenuation system. The electronics design is thus given in Figure 5.6. The source-detector configuration must be as in Figure 5.7. The system weighs about 1-1/4 lbs and occupies 20 in³ for the maximum configuration. If a smaller proportional counter is used, this can be reduced to 3/4 lb and 15 in³. The proportional counter would be identical in physical construction to that mentioned in Section 5.2.4, while the gas fill would be Kr + CO₂.

5.4 Comparison of Methods

The Np M x-ray system and the Ar K x-ray system can be compared on the basis of the preceding discussions (Sections 5.2 and 5.3). Since both must be used in conjunction with the α particle system, we assume that ρ_m (Eq. 5.1) is known to 0.6×10^{-6} g/cm³ or 2%, whichever is larger. This approximates what can be achieved quite readily, and also allows for the 2% systematic errors arising from the slightly different response to CO₂ and N₂. Consideration is given to two special cases: $w_{Ar} = 0.00$, and $w_{Ar} = 0.35$. The latter is the approximate maximum Ar mass fraction expected by the VM atmosphere models.

The densities $\rho_{CO_2} + \rho_{N_2} \equiv \rho_2$, and ρ_{Ar} are calculated as shown in Sections 5.2 and 5.3, along with the errors given by Equations (5.7), (5.8), (5.28) and (5.29). The large uncertainty in w_{Ar} at low densities (see Table 5.3) makes Equations (5.28) and (5.29) somewhat ambiguous in that no experimental value for w_{Ar} exists for use in these equations. Thus, near $\rho_m = 0$ Equations (5.28) and (5.29) have used the value of w_{Ar} which gives the maximum density errors. With this condition, the two x-ray systems are compared in Table 5.4.

The results in Table 5.4 show that the Np M x-ray system yields far better results than the Ar K x-ray system. The last column lists 2% of the total gas density, ρ . As shown by (5.11), the systematic errors in ρ_2 and ρ_{Ar} are about 2% of ρ , so statistical errors smaller than 2% of ρ are meaningless. The same condition is expected to hold for the Ar K x-ray system. Since the analysis of data for the Np M x-ray system is far easier than for the Ar K x-ray system, and since the former uses a weaker α source (1 m Ci vs. 10 m Ci), it appears that the Np M x-ray system is in general superior to the Ar K x-ray system.

Table 5.4

Comparison of Ar Measurement Systems

All densities are in 10^{-6} g/cm^3

$$\rho_2 \equiv \rho_{\text{CO}_2} + \rho_{\text{N}_2}, \quad \rho = \text{true gas density}$$

$$1) w_{\text{Ar}} = 0.00$$

ρ_m	Np M X-Ray		Ar K X-Ray		2% of ρ
	$\delta \rho_2$	$\delta \rho_{\text{Ar}}$	$\delta \rho_2$	$\delta \rho_{\text{Ar}}$	
0	0.7	0.2	0.6	0.9	0
10	0.7	0.2	1.1	0.6	0.2
20	0.7	0.2	1.5	0.8	0.4
40	0.9	0.3	2.0	0.9	0.8
60	1.3	0.3	2.7	1.1	1.2
80	1.7	0.3	3.1	1.3	1.6

$$2) w_{\text{Ar}} = 0.35$$

ρ_m	Np M X-Ray		Ar K X-Ray		2% of ρ
	$\delta \rho_2$	$\delta \rho_{\text{Ar}}$	$\delta \rho_2$	$\delta \rho_{\text{Ar}}$	
0	0.7	0.2	0.6	0.9	0
10	0.7	0.2	0.6	1.4	0.2
20	0.7	0.3	0.7	2.0	0.5
40	0.9	0.3	0.8	2.8	0.9
60	1.3	0.4	1.1	3.6	1.4
80	1.8	0.5	1.4	4.0	1.8

6. SUMMARY

The results of this study may be summarized as follows.

6.1 Density Measurements

Gas density measuring systems based on the energy loss of α particles in the gas have been shown to be feasible. The systems are gas composition dependent, but for CO_2 , N_2 and Ar mixtures the response will give a measured density of

$$\rho_m = \rho_{\text{CO}_2} + \rho_{\text{N}_2} + 0.67 \rho_{\text{Ar}} \quad (6.1)$$

Equation (6.1) is only accurate to 2% of the total gas density, $\rho = \rho_{\text{CO}_2} + \rho_{\text{N}_2} + \rho_{\text{Ar}}$, if the system is calibrated with 50% CO_2 + 50% N_2 (by weight). This is shown by the measured stopping power ratios in Figure 6.1, which also shows that energy losses in the gas should be for α particles greater than about 1 MeV.

When gas composition is known then the 2% systematic error of Eq. (6.1) can be eliminated by converting the calibration curve to the known composition. For such cases the restriction to energy loss by α particles greater than 1 MeV is also eliminated.

6.1.1 Thin Source Method

The basic results for the thin source method are listed in Table 6.1, which is based on Table 4.4. Statistical errors are seen to be small compared to a 0.5% gain drift or the 1% of full scale telemetry errors. The thin source system gives greater accuracy at high density than at low density. The most suitable α source currently available is vacuum sublimed Am^{241} . Construction of the thin source systems described in Section 4.3 is quite straightforward.

6.1.2 Thick Source Method

The basic results for the thick source method are listed in Table 6.2. For the minimum power system the statistical errors dominate at low densities while the 1% telemetry errors dominate at high densities. The maximum performance system is dominated by the statistical errors. The 0.5% electronic drift error is negligible for source-detector separations greater than about 10 cm, where it is $0.13 \times 10^{-6} \text{ g/cm}^3$. The most suitable currently available source is the Am^{241} foil source, although source spectrum reproducibility is not as good as desirable. Construction of the thick source systems described in Section 4.3 is quite straightforward.

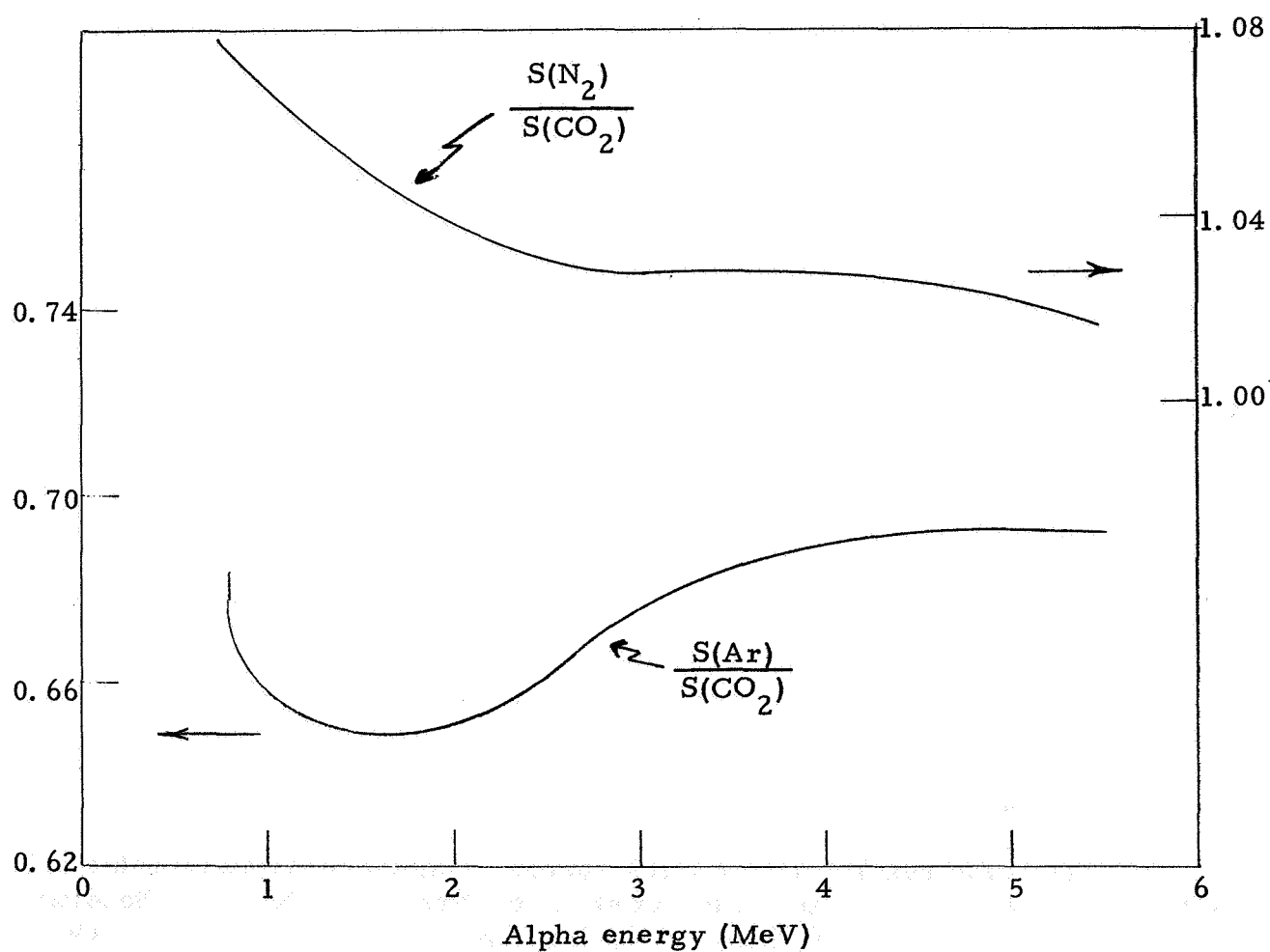


Figure 6. 1 Plots of N_2 to CO_2 and of Ar to CO_2 Stopping Power Ratios.

Table 6. 1
Estimated Errors of the Thin Source System

4000 counts used for statistical errors.
 0. 5% gain change used for electronic drift error.
 1% of full scale used for telemetry error.

Applies to 2 to 5 MeV α sources, at 8 to 55 cm source-detector separation.

All densities given in 10^{-6} g/cm³.

Gas density ρ_m	Statistical error $\delta \rho_{st}$	Electronic drift error $\delta \rho_{st}$	Telemetry error $\delta \rho_{TM}$	Systematic error (2%) (0. 02 ρ_m)	<u>Density errors for</u>		
					Minimum system (Fig. 4. 24)	Intermediate system (Fig. 4. 25)	Maximum system (Fig. 4. 26)
0	0. 15	0. 8	1. 6	0	3	1. 8	0. 8
80	$\approx 0. 05$	$\approx 0. 1$	≈ 1	1. 6	≈ 1	≈ 1	$\approx 0. 1$

Table 6.2
Estimated Errors of the Thick Source System

4000 counts used for statistical errors.
 0.5% gain change used for electronic drift error (assumed $D = 25$ cm).
 1% of full scale (40 counts) used for telemetry error.

All densities are in 10^{-6} g/cm³.

Gas density ρ_m	Electronic drift error	Systematic error (2%) ($0.02 \rho_m$)	Minimum System		Maximum System	
			Statistical error $\delta \rho_{st}$	Telemetry error $\delta \rho_{TM}$	Total error $\delta \rho_m$	Statistical error $\delta \rho_{st} (= \delta \rho_m)$
0	0.05	0	0.7	0.4	0.8	0.3
20	0.05	0.4	0.7	0.6	0.9	0.4
40	0.05	0.8	0.8	0.8	1.2	0.7
80	0.05	1.6	1.1	3.4	3.6	3

6.2 Argon Composition Measurement

6.2.1 X-Ray Attenuation Method

The Np M x-ray attenuation system measures an effective density of

$$\rho'_m = \rho_{Ar} + 0.094 (\rho_{CO_2} + \rho_{N_2}) \quad (6.2)$$

The coefficients of ρ_{CO_2} and ρ_{N_2} are actually $\pm 10\%$ from 0.094, so (6.2) is an approximation within these limits. The achievable accuracies for ρ'_m are listed in Table 6.3, which is taken from Table 5.1. The system uses a 1 mCi Am^{241} vacuum sublimed source. Construction of the system is not expected to be difficult.

6.2.2 Fluorescent X-Ray Method

The Ar fluorescent x-ray detection method yields usable results. Its response is approximated by

$$N_{xm} \approx \left(26 w_{Ar}^{1.5} \rho_m^{0.75} + 148 \right) \text{ cnts/sec} \quad (6.3)$$

In practice a series of calibration curves would be necessary, since (6.3) is a very rough approximation at high densities. As shown in Table 5.4, the Np M x-ray attenuation method yields smaller errors in $(\rho_{CO_2} + \rho_{N_2})$ and ρ_{Ar} , and also has a simpler data analysis procedure. The Ar K x-ray system can be easily constructed, but has no advantages over the Np M x-ray system and so will not be considered further.

6.3 Estimated Density Measurement Accuracy

6.3.1 Alpha Particle System Used with Argon Composition Measurement

The errors for this combination are calculated on the basis of Eq. (6.1) for the alpha particle system and Eq. (6.2) for the Np M x-ray attenuation system. The results of Section 5.2.1, Equations (5.5) to (5.11) then give the errors listed in Tables 6.4 and 6.5. Table 6.4 is for the thin source system and lists

$$\delta \rho = \delta \rho_{st} + \delta \rho_{sys} \quad (6.4)$$

Table 6.3

Estimated Errors of the X-Ray Attenuation System

Densities are in 10^{-6} g/cm^3 - taken from Table 5.1.

<u>ρ'_m</u>	<u>$\delta \rho'_m$</u>
0	0.2
20	0.3
40	0.6
80	2.0

Table 6.4

Errors for the Thin Source System Used with the
Np M X-Ray System

All densities in 10^{-6} g/cm^3 .

$$\delta \rho_2 \equiv \delta(\rho_{\text{CO}_2} + \rho_{\text{N}_2})$$

$$1) w_{\text{Ar}} = 0, \rho_{\text{CO}_2} + \rho_{\text{N}_2} = \rho, \rho_{\text{Ar}} = 0$$

ρ	$\delta \rho_{2 \text{ sys}}$	$\delta \rho_{\text{Ar sys}}$	Minimum		Intermediate		Maximum	
			$\delta \rho_2$	$\delta \rho_{\text{Ar}}$	$\delta \rho_2$	$\delta \rho_{\text{Ar}}$	$\delta \rho_2$	$\delta \rho_{\text{Ar}}$
0	0	0	3.2	0.4	1.9	0.3	0.9	0.2
20	0.4	0.2	3.1	0.5	2.1	0.5	1.3	0.4
40	0.8	0.4	2.9	0.7	2.3	0.7	1.5	0.6
80	1.6	0.8	2.7	1.1	2.7	1.1	1.7	1.1

$$2) w_{\text{Ar}} = 0.35, \rho_{\text{CO}_2} + \rho_{\text{N}_2} = 0.65\rho, \rho_{\text{Ar}} = 0.35\rho$$

ρ	$\delta \rho_{2 \text{ sys}}$	$\delta \rho_{\text{Ar sys}}$	Minimum		Intermediate		Maximum	
			$\delta \rho_2$	$\delta \rho_{\text{Ar}}$	$\delta \rho_2$	$\delta \rho_{\text{Ar}}$	$\delta \rho_2$	$\delta \rho_{\text{Ar}}$
0	0	0	3.2	0.4	1.9	0.3	0.9	0.2
20	0.4	0.24	3.1	0.6	2.1	0.5	1.1	0.5
40	0.8	0.5	3.0	0.9	2.3	0.9	1.4	0.8
80	1.6	1.0	2.7	1.5	2.7	1.5	2.0	1.5

Table 6.5

Errors for the Thick Source System Used with the
Np M X-Ray System

All densities in 10^{-6} g/cm^3 .

$$\delta \rho_2 \equiv \delta(\rho_{\text{CO}_2} + \rho_{\text{N}_2})$$

$$1) w_{\text{Ar}} = 0, \quad \rho_{\text{CO}_2} + \rho_{\text{N}_2} = \rho, \quad \rho_{\text{Ar}} = 0$$

ρ	$\delta \rho_{2 \text{ sys}}$	$\delta \rho_{\text{Ar sys}}$	<u>Minimum</u>		<u>Maximum</u>	
			$\delta \rho_2$	$\delta \rho_{\text{Ar}}$	$\delta \rho_2$	$\delta \rho_{\text{Ar}}$
0	0	0	0.9	0.2	0.4	0.2
20	0.4	0.2	1.4	0.4	0.9	0.4
40	0.8	0.4	2.1	0.6	1.6	0.6
80	1.6	0.8	5.5	1.2	4.8	1.2

$$2) w_{\text{Ar}} = 0.35, \quad \rho_{\text{CO}_2} + \rho_{\text{N}_2} = 0.65\rho, \quad \rho_{\text{Ar}} = 0.35\rho$$

ρ	$\delta \rho_{2 \text{ sys}}$	$\delta \rho_{\text{Ar sys}}$	<u>Minimum</u>		<u>Maximum</u>	
			$\delta \rho_2$	$\delta \rho_{\text{Ar}}$	$\delta \rho_2$	$\delta \rho_{\text{Ar}}$
0	0	0	0.9	0.2	0.4	0.2
20	0.4	0.24	1.4	0.5	0.9	0.5
40	0.8	0.5	2.0	0.8	1.5	0.8
80	1.6	1.0	4.8	1.6	4.2	1.6

where $\delta\rho_{st}$ is from Equations (5.7) and (5.8), and $\delta\rho_{sys}$ is from Equations (5.9) and (5.10). The necessary values of $\delta\rho_m$ and $\delta\rho'_m$ are taken from Tables 6.1 and 6.3. The results for the thick source system are given in Table 6.5, with the $\delta\rho_m$ values coming from Table 6.2.

The values for the systematic (composition dependent) errors are also listed in Tables 6.4 and 6.5. The systematic errors are the minimum achievable errors with these systems if only CO_2 , N_2 and Ar are likely gas constituents. The difference of $\delta\rho$ and $\delta\rho_{sys}$ is the statistical error of Equations (5.7) and (5.8). Note that this "statistical" error contains a non-random component arising from electronic drifts and that this component cannot be reduced by averaging successive measurements.

6.3.2 Alpha Particle System Used with Separate Gas Composition Measurement

An alpha particle density measuring system will generally be calibrated with one or several gases. This (or these) calibration curve(s) can then be converted to that of another gas composition by the methods outlined in Section 3.1. Thus, if a separate system provides a complete gas composition analysis it will be possible to convert ρ_m into a true gas density ρ .

For most gases the relation between ρ_m and ρ is

$$\rho_m \approx f\rho \quad (6.5)$$

where, e. g., if the calibration is made with CO_2 , then $f \approx 1.03$ for N_2 and $f \approx 0.67$ for Ar. Under these conditions

$$\delta\rho \approx \delta\rho_m/f \quad (6.6)$$

Since f is generally on the order of 1, the values of $\delta\rho$ are thus approximately equal to the values of $\delta\rho_m$ given in Table 6.1 for the thin source system, and in Table 6.2 for the thick source system.

6.3.3 Alpha Particle System Used with No Composition Information

When no composition information is available the error from composition uncertainty will generally dominate. This error depends on the estimated maximum mass fractions of the gases which may be present. Thus, a system calibrated with CO_2 will give a measured density which is about 49% lower than the true density when used in Ar. The percent errors depend on the gas used to obtain the calibration curve, since a system which is calibrated

with 0.5 CO₂ + 0.5 Ar (mass fractions) will give a measured density 17% high with CO₂ and 25% low with Ar.

The density errors mentioned thus far are defined by

$$\% \text{ error} = \frac{\rho_m - \rho}{\rho_m} \times 100 \quad (6.7)$$

If Eq. (6.5) holds then

$$\% \text{ error} = \frac{1 - f}{f} \times 100 \quad (6.8)$$

Note that

$$f = S_f / S_c \quad (6.9)$$

where S_f is the stopping power of the gas specified by f and S_c is the stopping power of the calibration gas.

Table 6.6 lists the systematic errors expected for a number of gas compositions when the α particle system is calibrated with a different gas. Note that maximum deviations occur for the extreme values of f which can be obtained for a given set of gases. f Values for some gases were obtained as described in Appendix C. Note that CO deviations are less than for N₂, but that if H₂O were to form a very large fraction of the gas then the measured densities would be 16% low.

7. CONCLUSIONS AND RECOMMENDATIONS

The principal conclusions may be summarized as follows:

1) Gas density measuring systems based on the energy loss of α particles have been shown to be feasible for measuring the Martian atmosphere. The response of these systems is composition dependent, but by confining energy loss in the gas to α particles greater than about 1 MeV the systems yield a measured density which is a constant fraction of the true density, to a few percent. For use in the Martian atmosphere with estimated composition limited to CO₂, N₂ and Ar, the systems give nearly equal response for CO₂ and N₂, so only the Ar component need be separately measured to give the true gas density.

2) The α particle systems can be classified as thin source or thick source systems. The thin source system measures the average energy loss of a narrow α spectrum, and gives greatest accuracy at high densities. The thick

Table 6.6

Composition Dependent Density Errors for the
Alpha Particle System Used Alone

All errors are given in percent deviation from the measured density (Equations (6.7) and (6.8)).

All gas compositions are given in mass fractions, w.

<u>Maximum concentration of allowed gas components, w</u>	<u>Composition of calibration gas</u>	<u>Maximum errors Gas composition, % error</u>
1 CO ₂ , 1 N ₂ , 1 Ar	1 CO ₂	$\begin{cases} 1 \text{ Ar} , & +49 \\ 1 \text{ N}_2 , & -3 \end{cases}$
1 CO ₂ , 1 N ₂ , 0.35 Ar	1 CO ₂	$\begin{cases} 0.35 \text{ Ar} + 0.65 \text{ CO}_2 , & +13 \\ 1 \text{ N}_2 , & -3 \end{cases}$
1 CO ₂ , 1 N ₂ , 0.35 Ar	0.83 CO ₂ + 0.17 Ar	$\begin{cases} 0.35 \text{ Ar} + 0.65 \text{ CO}_2 , & +7 \\ 1 \text{ N}_2 , & -8 \end{cases}$
1 CO ₂ , 1 CO	1 CO ₂	1 CO , -1
1 CO ₂ , 1 H ₂ O	1 CO ₂	1 H ₂ O , -16

source system uses a broad α spectrum and measures the fraction which lies above a fixed threshold. This system can be made to give a nearly constant fractional density error, with accuracy at low densities being about 0.5×10^{-6} g/cm³. Since composition-dependent systematic errors of a few percent are likely to be present with the α particle systems, the thick source system is thus preferred over the thin source system. Preliminary estimates of weight and power are 3/4 to 1 lb and 200 to 500 mw, depending on the design selected.

3) If the weight and power of the entire system is increased by about 100%, then the Ar component can be obtained by measuring the attenuation of the 3.3 keV Np M x-rays from an Am²⁴¹ source. This combined with the α particle system will give the CO₂ + N₂ density and the Ar density, with systematic errors being about 2%. These two instruments are both required to make the measurements, but no auxiliary data are required if the CO₂, N₂ and Ar composition limitation is valid.

4) The α particle system can also be used with gas composition data from another source. Under these conditions the greatest density accuracy is achieved, since the α particle system calibration curve can be converted to the measured composition thus eliminating this source of systematic error.

5) The worst performance is obtained when using the α particle system alone. Then systematic errors can be as large as $\pm 8\%$ for the most likely compositions of the Martian atmosphere (range for VM models).

As a result of the foregoing conclusions, the following recommendations are made:

1) A feasibility model of the thick source system should be constructed and tested. The selection of one of the two thick source systems would depend on whether greater accuracy is desired (maximum performance), or weight and power are to be reduced (minimum performance). The primary purpose of the feasibility model is to develop the electronics for a prototype and show that the experimental system response and accuracy are as predicted.

2) A prototype of a flight model thick source system should be constructed using the finalized electronics of the feasibility model. The prototype would have minimum weight and volume, and be packaged to withstand the shock and environment requirements of an actual flight model.

3) When the decontamination procedures for the Martian lander vehicle are finalized, the α sources and solid state detectors should be tested and, if necessary, modified so that they can withstand the procedure. The theoretical effects of the Martian atmosphere, including possible water vapor and frost, on the system should also be investigated. These studies would be carried out under the feasibility model testing program of (1).

4) If a system yielding the Ar fraction as well as total density is desired, a feasibility model and prototype of the Np M x-ray attenuation system should be constructed. The work on this system would proceed in the manner described for the α system in (1), (2) and (3).

APPENDIX A

CALCULATION OF GAS DENSITIES FROM PRESSURE AND TEMPERATURE MEASUREMENTS

The α particle systems measure gas density, while normal laboratory instruments usually provide pressure and temperature. Calibration of the α particle systems thus requires calculation of gas density from pressure and temperature measurements. This can be done for a known gas composition, since from the perfect gas law

$$\rho = \frac{nM}{V} = \frac{PM}{RT} \quad (\text{A. 1})$$

where ρ is the gas density, n the number of moles in the volume V , P is the pressure, T the absolute temperature, R the gas constant, and M the average molecular weight. For gas mixtures

$$M = \sum_i w_i M_i \quad (\text{A. 2})$$

where

$$w_i = \rho_i / \rho \quad (\text{A. 3})$$

Since the partial pressures, P_i , are generally measured, a more usable form of (A. 3) is

$$w_i = P_i M_i / \left(\sum_i P_i M_i \right) \quad (\text{A. 4})$$

Equation (A. 1) is true only for a perfect gas. For normal gases the Van der Waals equation of state is better, and is given by

$$(P + \rho^2 a / M^2) (M / \rho - b) = RT \quad (\text{A. 5})$$

Since a and b are small constants the first order density difference between (A. 1) and (A. 5) can be calculated to be

$$\frac{\Delta\rho}{\rho} \approx \frac{P}{RT} \left[\frac{a}{RT} - b \right] \quad (\text{A. 6})$$

Taking $T = 300^{\circ}\text{K}$, $R = 0.08206 \text{ l - atm/(mol - }^{\circ}\text{K)}$, and the constants a and b from Ref. 4.2, p D-104, the density errors in Table A.1 are found for CO_2 , N_2 and Ar. Since the maximum pressures used in the present investigation are significantly less than 1 atm (760 mm Hg), the densities obtained from the perfect gas law (Eq. (A.1)) are seen to be accurate to 0.1% or better.

Table A.1

Density Differences Between the Perfect Gas Law
and the Van der Waals Equation

<u>Gas</u>	$\Delta\rho/\rho$, in percent	
	<u>(P = 1 atm)</u>	<u>(P = 0.1 atm)</u>
CO_2	0.4	0.04
N_2	0.07	0.007
Ar	0.09	0.009

APPENDIX B

APPROXIMATE CALCULATION OF THE EFFECTS OF A TEMPERATURE DIFFERENCE BETWEEN THE DENSITY MEASURING SYSTEM AND THE ATMOSPHERIC GASES

The α particle system measures gas density independent of the gas temperature and pressure. If the α particle system and the Martian lander structure are at a temperature significantly different from the ambient atmospheric temperature, then the gas surrounding the lander may be at an intermediate temperature. The actual temperature change of the gas depends on lander geometry and on the presence of winds. However, any temperature changes in the gas will cause a corresponding density change given by

$$\Delta\rho = -\rho \frac{\Delta T}{T} \quad (\text{B. 1})$$

Equation (B. 1) is easily derived from Eq. (A. 1) by assuming $P = \text{constant}$. From (B. 1) it is seen that a 50°C temperature at 250°K introduces a 20% density error.

The result (B. 1) is only true when there is no wind present, such that the gas surrounding the lander can come to the lander temperature. As shown by Table 2.2, the lander descent velocity is on the order of 50 m/sec, and in Table I of Ref. 2.1 the surface wind speeds are estimated to be greater than 100 ft/sec \approx 20 m/sec. It is thus necessary to estimate the rate of diffusion of heat into the gas from the lander and compare this rate with the above wind speeds.

The heat diffusion equation for a one dimensional problem is

$$\frac{\partial T}{\partial t} = a^2 \frac{\partial^2 T}{\partial x^2} \quad (\text{B. 2})$$

where $T(x, t)$ is the temperature, x is the perpendicular distance from an infinite plane bounding the gas on one side, t is the time, and for a gas

$$a^2 = \kappa / \rho C \quad (\text{B. 3})$$

with ρ the gas density, κ its thermal conductivity, and C its heat capacity per

unit mass (Ref. B. 1, p 1584 ff). Here it is assumed that a^2 is constant, although it does have some temperature dependence for most gases. For CO_2 at 250°K the values are

$$\kappa \approx 3 \times 10^{-5} \frac{\text{cal}}{\text{sec-cm}^2 - ^\circ\text{K/cm}} \quad (\text{B. 4})$$

$$C \approx 0.16 \text{ cal/}^\circ\text{K-g}$$

$$\rho \approx 10^{-5} \text{ g/cm}^3$$

so

$$a^2 \approx 19 \text{ cm}^2/\text{sec} \quad (\text{B. 5})$$

In (B. 4) expansion at constant pressure is assumed in obtaining C.

The solution to (B. 2) is subject to the initial conditions

$$\begin{aligned} T(x, 0) &= T_g \\ T(\infty, t) &= T_g \\ T(0, t) &= T_o \end{aligned} \quad (\text{B. 6})$$

Here T_g is the initial ambient temperature of the gas, and T_o is the lander temperature, which is assumed not to change during the initial conduction process. The solution of (B. 2) can be obtained more easily by setting

$$T(x, t) = T_g + (T_o - T_g) F(x, t) \quad (\text{B. 7})$$

where the initial conditions (B. 6) now becomes

$$\begin{aligned} F(x, 0) &= 0 \\ F(\infty, t) &= 0 \\ F(0, t) &= 1 \end{aligned} \quad (\text{B. 8})$$

and (B. 2) becomes

$$\frac{\partial F}{\partial t} = a^2 \frac{\partial^2 F}{\partial x^2} \quad (\text{B. 9})$$

The solution of (B. 9) is obtained in two steps. From Ref. B. 1, p 692, the solution of (B. 9) for a heat pulse at $x = 0$, $t = 0$ is given by

$$f(x, t) = \frac{1}{\sqrt{t}} e^{-x^2/(4a^2 t)} \quad (\text{B. 10})$$

Note that (B. 10) does not satisfy the last of conditions (B. 8), since the temperature of the slab surface ($x = 0$) becomes infinite at $t = 0$ (the precise value depends on how x and t approach 0). To obtain $F(x, t)$, a source function $s(t)$ is introduced so that

$$F(x, t) = \int_0^t s(t_0) f(x, t-t_0) dt_0 \quad (\text{B. 11})$$

To satisfy the third of conditions (B. 8) it is required that

$$\int_0^t \frac{s(t_0)}{\sqrt{t-t_0}} dt_0 = 1 \quad (\text{B. 12})$$

A solution of (B. 12) is found to be

$$s(t_0) = \frac{1}{\pi \sqrt{t_0}} \quad (\text{B. 13})$$

so that

$$F(x, t) = \int_0^t \frac{1}{\pi \sqrt{(t-t_0)t_0}} e^{-x^2/[4a^2(t-t_0)]} dt_0 \quad (\text{B. 14})$$

The integral in (B. 14) is difficult, if not impossible, to evaluate analytically. However, since $x \geq 0$ and $t \geq t_0$, the exponential function in (B. 14) is always ≤ 1 , so an upper limit can be obtained by setting $t_0 = 0$ in the exponential and evaluating

$$\int_0^t \frac{1}{\pi \sqrt{(t-t_o)} t_o} dt_o = 1 \quad (\text{B. 15})$$

This gives

$$F(x, t) \leq e^{-x^2/(4 a^2 t)} \quad (\text{B. 16})$$

and thus

$$T(x, t) \approx T_g + (T_o - T_g) e^{-x^2/(4 a^2 t)} \quad (\text{B. 17})$$

The exponential in (B. 17) defines a time constant

$$\tau = x^2/4 a^2 \quad (\text{B. 18})$$

which depends on the distance x . An effective velocity to reach a distance x is thus given by

$$v_{\text{eff}} \approx \frac{x}{\tau} = \frac{4 a^2}{x} \quad (\text{B. 19})$$

For $x = 10$ cm this becomes (using (B. 5))

$$\begin{aligned} v_{\text{eff}} &\approx 7.6 \text{ cm/sec} \\ &= 0.076 \text{ m/sec} \end{aligned} \quad (\text{B. 20})$$

which is considerably smaller than the expected wind velocities.

An estimate of the error in the density measurement can be obtained as follows. In (B. 19) set $v_{\text{eff}} = v_w$ where v_w is the wind speed. This gives an effective thickness

$$x_w = 4 a^2 / v_w \quad (\text{B. 21})$$

over which it is assumed the temperature is T_o . By assuming that the remainder of the gas is at temperature T_g and that the source-detector distance is D ,

the density error can be calculated to be

$$\begin{aligned}\frac{\Delta\rho}{\rho} &= \frac{x_w}{D} \left(\frac{T_g}{T_o} - 1 \right) \\ &= \frac{4 a^2}{D v_w} \left(\frac{T_g}{T_o} - 1 \right)\end{aligned}\tag{B. 22}$$

By setting $D = 20 \text{ cm}$, $v_w = 40 \text{ m/sec} = 4 \times 10^3 \text{ cm/sec}$, $a^2 = 19 \text{ cm}^2/\text{sec}$, $T_g = 250^\circ\text{K}$, $T_o = 300^\circ\text{K}$, there results

$$\frac{\Delta\rho}{\rho} \approx - 1.6 \times 10^{-4} = 0.016\%\tag{B. 23}$$

Thus the measured density will be negligibly effected for the conditions, which might approximate entry into the Martian atmosphere.

When the lander is on the Martian surface, a worst case condition is likely to be a 10°C temperature difference and $v_w = 10 \text{ cm/sec}$, the latter being an order-of-magnitude estimate for convective flow produced by the temperature difference. For this case

$$\frac{\Delta\rho}{\rho} \approx \pm 0.4\%\tag{B. 24}$$

Temperature differences between the lander and the atmospheric gases are thus not expected to be a significant source of error.

APPENDIX C

DISCUSSION OF THE EFFECTS OF CO AND H₂O IN THE MEASURED ATMOSPHERE

Since there is current concern about H₂O and CO being present in the Martian atmosphere, the effects of these gases on the density measuring systems is considered here only briefly. From Ref. 3.1 the ratios of CO to CO₂ and of H₂O to CO₂ stopping powers can be obtained and these are plotted in Figure C. 1. From Figure C. 1 it appears that an effective density for CO and H₂O can be used for the α particle systems, so that Eq. (3. 4) can be modified to give

$$\begin{aligned} \rho_m = & \rho_{CO_2} + 1.035 \rho_{N_2} + 0.67 \rho_{Ar} \\ & + 1.014 \rho_{CO} + 1.19 \rho_{H_2O} \end{aligned} \quad (C. 1)$$

From (C. 1) it is seen that CO has the response of an approximately 50% CO₂ + 50% N₂ mixture, while H₂O has an effective density about 10% higher than CO₂.

The amount of water vapor present in the Martian atmosphere will be limited by the vapor pressure of H₂O at atmospheric temperatures. If the atmospheric temperature is 250°K, then the density of H₂O will be 0.7×10^{-6} g/cm³ or less; similarly at 0°C $\rho_{H_2O} \leq 4.8 \times 10^{-6}$ g/cm³ and at 20°C $\rho_{H_2O} \leq 17 \times 10^{-6}$ g/cm³. For surface densities of 40×10^{-6} g/cm³ the H₂O content will thus be less than 50% of the total density and (C. 1) shows that less than 10% systematic density error results. If a separate system measures the dew point of the Martian atmosphere, however, then (C. 1) can be used to correct the measured density since the dew point effectively gives ρ_{H_2O} .

The effect of CO and H₂O on the Np M x-ray attenuation system is to change Eq. (5. 4a) to

$$\begin{aligned} \rho'_m = & \rho_{Ar} + 0.105 \rho_{CO_2} + 0.083 \rho_{N_2} \\ & + 0.093 \rho_{CO} + 0.111 \rho_{H_2O} \end{aligned} \quad (C. 2)$$

Again, CO has a response intermediate to CO₂ and N₂, while H₂O is now about equal to CO₂ in response. The Np M x-ray system thus will not have its response affected other than to have $\rho_{CO_2} + \rho_{N_2}$ replaced by $\rho_{CO_2} + \rho_{N_2} + \rho_{CO} + \rho_{H_2O}$.

The preceding discussions show that overall density accuracy will not be affected if the H_2O component is separately measured. Otherwise, a systematic error of perhaps 10% could be introduced if a large amount of H_2O is present. CO has no effect on the systems, responding about the same as CO_2 and N_2 .

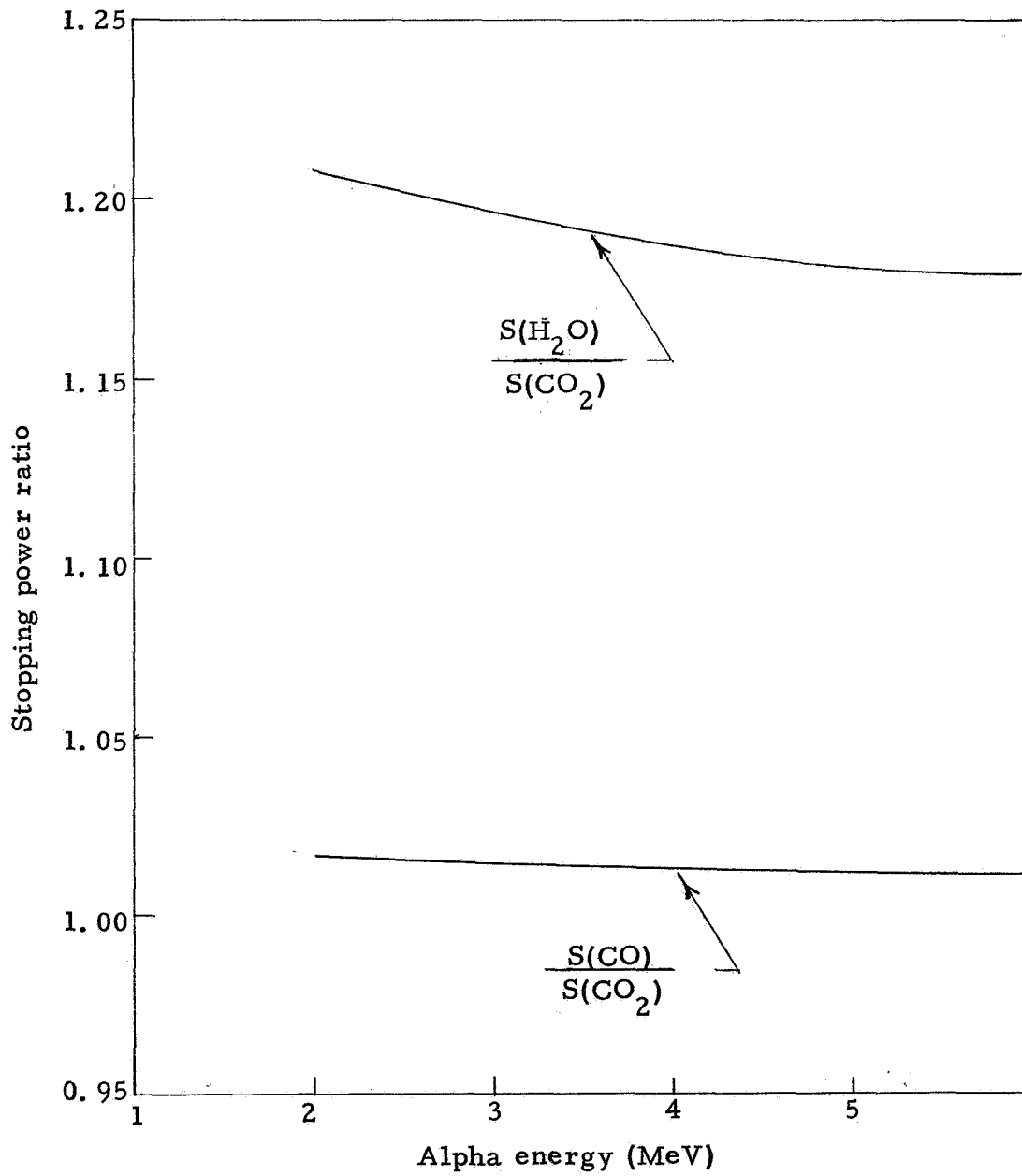


Figure C. 1 Plots of CO to CO₂ and of H₂O to CO₂ Stopping Power Ratios.

APPENDIX D

EFFECT OF A FROST LAYER ON THE SYSTEMS

The presence of H_2O in the Martian atmosphere raises the possibility of frost formation over the α sources and on the detector face. If the total frost thickness is t_f g/cm² and the source-detector separation is D_1 cm, then this appears as a spurious water density of

$$\rho_{f_1} = t_f/D_1 \quad (D. 1)$$

The total system response will then be

$$\begin{aligned} \rho_1 &= \rho_{\text{true}} + \rho_{f_1} \\ &= \rho_{\text{true}} + t_f/D_1 \end{aligned} \quad (D. 2)$$

where we neglect the slight difference in response for H_2O , CO_2 , etc. The frost layer can be measured by using a second source at a separation $D_2 \neq D_1$. This second source gives a response

$$\rho_2 = \rho_{\text{true}} + t_f/D_2 \quad (D. 3)$$

By solving (D. 2) and (D. 3) there results

$$t_f = D_2 D_1 (\rho_1 - \rho_2)/(D_2 - D_1) \quad (D. 4)$$

and

$$\rho_{\text{true}} = (D_1 \rho_1 - D_2 \rho_2)/(D_1 - D_2) \quad (D. 5)$$

The preceding analysis assumes that both α sources are covered with equal thicknesses of frost. In practice, a more involved analysis must be used, based on Eq. (C. 1). Use of two sources with the same detector also requires additional electronic circuitry to distinguish the two sources, as well as limiting the source energies and spectra that may be used. However, it should be possible to design a double-source system which can measure both air density and frost layer thickness.

REFERENCES

2. 1 Statement of Work, L 15-9084, Exhibit A, March 22, 1968. Part of Request for Proposal which preceded the award of the contract described in the present report.
3. 1 C. W. Hill, W. B. Ritchie, and K. M. Simpson, Data Compilation and Evaluation of Space Shielding Problems, Vol. I, Range and Stopping Power Data, Rep. ER 7777, Lockheed-Georgia Co., also NASA CR-69434.
3. 2 W. Whaling, The Energy Loss of Charged Particles in Matter, in Handbuch der Physik, S. Flügge, ed., pp 193-217, Springer, Berlin (1958).
3. 3 J. F. Janni, Calculations of Energy Loss, Range, Pathlength, Straggling, Multiple Scattering, and the Probability of Inelastic Nuclear Collisions for 0.1-to1000-MeV Protons, Technical Report AFWL-TR-65-150, Air Force Weapons Laboratory, Kirtland Air Force Base, New Mexico (1966).
3. 4 J. A. Coleman, D. P. Love, J. H. Trainor, and D. J. Williams, Low Energy Proton Damage Effects in Silicon Surface-Barrier Detectors, IEEE Trans. on Nucl. Sci., NS-15, #1, 482-90 (Feb. 1968).
3. 5 J. A. Coleman, D. P. Love, J. H. Trainor, and D. J. Williams, Effects of Damage by 0.8 MeV-5.0 MeV Protons in Silicon Surface-Barrier Detectors, IEEE Trans. on Nucl. Sci., NS-15, #3, 363-72 (June 1968).
3. 6 G. Dearnaley, and D. C. Northrop, Semiconductor Counters for Nuclear Radiations, Second Edition. Chap. 10, Wiley, New York (1966).
3. 7 R. E. Scott, Radiation Effects of Protons and Electrons in Silicon Diffused-Junction Detectors, IEEE Trans. on Nucl. Sci., NS-11, #3, 206-12 (June 1964).
3. 8 R. E. Scott, Low-Rate Proton Bombardment of Diffused Silicon Counters, Nucl. Instr. and Methods, 32, 171-2 (1965).
3. 9 G. Dearnaley, Radiation Damage by Charged Particles in Silicon Junction Detectors, IEEE Trans. Nucl. Sci., NS-10, #1, 106-10 (1963).
3. 10 H. M. Mann, and J. L. Yntema, Heavy Particle Radiation Damage Effects in Lithium Drifted Silicon Detectors, IEEE Trans. Nucl. Sci., NS-11, #3, 201-5 (June 1964).
3. 11 R. D. Evans, The Atomic Nucleus, McGraw-Hill, New York (1955).

REFERENCES (cont' d)

- 4.1 C. M. Lederer, J. M. Hollander, and I. Perlman, Table of Isotopes, Sixth Edition, Wiley, New York (1967).
- 4.2 R. C. Weast, and S. M. Selby, eds., Handbook of Chemistry and Physics, 47th edition, Chemical Rubber Co., Cleveland (1966).
- 4.3 L. B. Magnusson, Intensities of X-Rays and γ -Rays in Am²⁴¹ Alpha Decay, Phys. Rev., 107, 161-70 (1957).
- 4.4 K. H. Ansell, The Radiochemical Centre, Amersham, England. Personal communication (July 11, 1968).
- 4.5 E. G. Hall, The Radiochemical Centre, Amersham, England. Personal communication (March 10, 1969).
- 4.6 T. N. Lahr, 3M Company, St. Paul, Minnesota. Personal Communication (March 6, 1969).
- 5.1 G. Fjeldbo, and W. R. Eshleman, The Atmosphere of Mars Analyzed by Integral Inversion of the Mariner IV Occultation Data, Planet. Space Sci., 16, 1035-59 (1968).
- 5.2 A. H. Compton, and S. K. Allison, X-Rays in Theory and Experiment, Second Edition, Van Nostrand, New York (1960).
- 5.3 B. L. Henke, R. L. Elgin, R. E. Lent, and R. B. Ledingham, X-Ray Absorption in the 2- to 200-A Region, Report No. AFOSR 67-1254, June 1967. Also AD 654315.
- 5.4 W. Henneberg, Z. Physik 86, 592 (1933).
- 5.5 E. Merzbacher, and H. W. Lewis, X-Ray Production by Heavy Charged Particles, pp 166-92, in Handbuch der Physik, Vol. 34, S. Flügge, ed., Springer-Verlag, Berlin (1958).
- B.1 P. M. Morse, and H. Feshbach, Methods of Theoretical Physics, 2 Vols., McGraw-Hill, New York (1953).